

GLOBAL ESTIMATE OF LIGHTNING ENERGY INJECTED  
INTO THE EARTH'S PLASMASPHERE

A DISSERTATION  
SUBMITTED TO THE DEPARTMENT OF ELECTRICAL  
ENGINEERING  
AND THE COMMITTEE ON GRADUATE STUDIES  
OF STANFORD UNIVERSITY  
IN PARTIAL FULFILLMENT OF THE REQUIREMENTS  
FOR THE DEGREE OF  
DOCTOR OF PHILOSOPHY

Andrew Compston  
March 2016

© 2016 by Andrew James Compston. All Rights Reserved.  
Re-distributed by Stanford University under license with the author.



This work is licensed under a Creative Commons Attribution-Noncommercial 3.0 United States License.  
<http://creativecommons.org/licenses/by-nc/3.0/us/>

This dissertation is online at: <http://purl.stanford.edu/tn332zw8900>

I certify that I have read this dissertation and that, in my opinion, it is fully adequate in scope and quality as a dissertation for the degree of Doctor of Philosophy.

**Umran Inan, Primary Adviser**

I certify that I have read this dissertation and that, in my opinion, it is fully adequate in scope and quality as a dissertation for the degree of Doctor of Philosophy.

**Ada S Y Poon, Co-Adviser**

I certify that I have read this dissertation and that, in my opinion, it is fully adequate in scope and quality as a dissertation for the degree of Doctor of Philosophy.

**John Gill, III**

I certify that I have read this dissertation and that, in my opinion, it is fully adequate in scope and quality as a dissertation for the degree of Doctor of Philosophy.

**Ivan Linscott**

Approved for the Stanford University Committee on Graduate Studies.

**Patricia J. Gumport, Vice Provost for Graduate Education**

*This signature page was generated electronically upon submission of this dissertation in electronic format. An original signed hard copy of the signature page is on file in University Archives.*

# Abstract

Generated by lightning, ‘whistlers’ are electromagnetic waves that propagate through the plasma surrounding the Earth in near-Earth space known as the plasmasphere. Electromagnetic waves propagating in the plasmasphere can influence the Van Allen radiation belts, a collection of highly energetic, charged particles surrounding the Earth and trapped by the Earth’s magnetic field. In particular, energy from these waves can reduce the number of electrons in the radiation belts by causing them to precipitate into the lower atmosphere. Therefore, an estimate of the amount of energy input into the radiation belts from electromagnetic waves like lightning-generated whistlers is vitally important to our understanding of the nature and dynamics of this important part of our planetary environment. Previous estimates of lightning energy in the plasmasphere failed to take into account such considerations as the distribution of lightning across the globe and the effect of the ionosphere on whistler propagation, both of which we examine here.

We first present a method to automatically identify upgoing whistler waves using measurements taken from low Earth orbiting satellites. The algorithm computes cross-correlations of the frequency-time spectrogram of the wave data with the expected shape of an upgoing whistler to determine whether or not a given set of data corresponds to a whistler. The technique is validated using data from the DEMETER satellite, and an FPGA-based real time implementation of the algorithm has been built to fly on board the TARANIS satellite, scheduled to launch in 2018.

Next, we provide a calculation of the lightning energy injected into the plasmasphere using a frequency domain finite element electromagnetic full wave simulation known as the full wave method (FWM) to quantitatively model the propagation of



electromagnetic waves through any number of horizontally stratified layers of plasma such as the ionosphere. We first compare the FWM predicted amount of lightning energy propagating upward with extensive available measurements from the DEMETER satellite. Our comparisons indicate that the field intensities determined by the FWM tend to underestimate the measured energy from DEMETER by as much as 6 dB, although we also present evidence suggesting that the calibration of the DEMETER data may be inaccurate.

Finally, we use the FWM to map the upgoing amount of electromagnetic wave energy propagating from each point on Earth for an arbitrary source. By then scaling with data on lightning occurring at each point on Earth as given by the Vaisala Global Lightning Dataset (GLD360) lightning detection network, we arrive at a global estimate of the lightning energy injected into Earth's plasmasphere. Our estimate is comparable to though slightly lower than previous estimates yet provides a more detailed picture of the distribution of lightning in the plasmasphere.

# Acknowledgments

As anyone who has undertaken the endeavor will tell you, completing a doctoral dissertation is no easy task, and the only way it is made possible is through the support of countless people along the way. I would now like to take the opportunity to express my gratitude to some of those people, although it must be emphasized this is by no means an exclusive list.

For me, the first people who really stand out in the road leading to this point are Wayne Catell and the late Gregory Skufca, two of my math teachers at Melbourne High School. Their dedication to teaching instilled in me a love of math that ultimately served as the impetus to embark on this journey.

Later in my undergraduate years at Georgia Tech, I certainly owe a debt of gratitude to Dr. Hans Schantz. He served as an incredible mentor during my two internships at Q-Track and, possibly to his chagrin, as he likely desired I might stay and work full time at Q-Track, served as an inspiration for me to pursue a doctoral dissertation. I realized after working at Q-Track that I wanted to work on the cutting edge of physics and technology, which is fundamentally what a doctoral dissertation is all about. And so, in the fall of 2008, I made my way to Stanford University, where I eventually wrote this dissertation almost eight years later.

My dissertation advisor, Professor Umran Inan, is a true inspiration. I remember looking at his calendar during my first year at Stanford and, in the face of back-to-back meetings with student after student, wondered how he could ever get anything done. He got plenty done of course. That he made time to advise me despite all of those other demands on his time is truly gratifying. I was disappointed to see him leave Stanford after my first year in order to become President of Koç University, as I

undoubtedly missed out on benefiting first hand from his extensive experience in this field. Still, he thankfully did keep his word that he would continue to support me remotely, and the VLF group continued to survive for many years after his departure due no doubt to his extraordinary abilities.

Along with Dr. Ivan Linscott, I collaborated with Dr. Jean-Louis Pinçon, Pedro Zamora, Tedjani Hachemi, and many other people at LPC2E in Orléans, France for my first main project at Stanford: the  $0^+$  whistler detector FPGA for TARANIS as detailed in Chapter 2 and Appendix A. Everyone at LPC2E has been a joy to work with, and I will continue to have fond memories of the celebratory dinners in which we all partook together following a regularly successful week of testing both here and in Orléans. Dr. Ivan Linscott also deserves special thanks for serving as my co-advisor and reader of this dissertation, and I especially appreciate the many interesting and stimulating conversations we have had over the last few years.

This dissertation likely would not have been written were it not for Professor Morris Cohen, who stepped in and provided extensive mentorship for me (and many other VLF group members it should be noted) after Professor Inan's departure to Koç University. Through Professor Cohen's guidance, I eventually determined my thesis topic and ultimately proceeded to write this dissertation. Dr. Nikolai Lehtinen and Professor Robert Marshall also provided instrumental support and guidance along the way that in many ways cannot be understated.

I was able to travel extensively throughout my time at Stanford, both domestically and internationally (and to Antarctica!). Often I took side trips whose costs were not officially covered by the university. The patience exhibited by Helen Niu in processing my trip reimbursements and filtering what was and was not covered is unrivaled. She was so accomodating and understanding of my crazy and confusing travel schedules, and I doubt I will ever know how she managed to get me the reimbursements she did when faced against Stanford's unyielding bureaucracy.

Professors Roger Romani, Ada Poon, and Brad Osgood accompanied my advisors Professor Inan and Dr. Linscott on my oral defense committee. I specifically requested those three to be on my committee in addition to my advisors because they are the three best professors with whom I had classes at Stanford. Astrophysics

has a mystique of being extremely difficult, but Professor Romani made the subject approachable and (relatively) easy to grasp. Professor Poon's approach to teaching antennas was quite interesting, and I loved being able to both get my hands dirty and build actual antennas as well as learn the theory behind them in lecture. Last but not least, Professor Osgood knows how to strike the perfect balance between mathematical formality and practical understanding in the teaching of Fourier Transforms that allowed me to get an A in what would otherwise be a difficult class.

I must also thank Professors Ada Poon (again) and John Gill for serving as readers for this dissertation. In particular, my last minute request of Professor Gill to be the fourth reader of the dissertation is greatly appreciated.

Finally, the VLF group would not have been possible without the numerous students that were part of it at one time or another, so I would like to thank all of them for allowing me to be part of their family. I suppose I am the last one to carry that torch.

DREW COMPSTON

*Stanford, CA*

*March 11, 2016*

*The research in this dissertation was supported by the Air Force Research Laboratory under award FA9453-11-C-0011 to Stanford University and fellowships awarded to the author from the National Defense Science and Engineering Graduate Fellowship Program and the National Science Foundation Graduate Research Fellowship Program. The Bosack Kruger Foundation Gift Fund additionally provided support for travel.*

# Contents

<b>Abstract</b>	<b>iv</b>
<b>Acknowledgments</b>	<b>vi</b>
<b>1 Introduction</b>	<b>1</b>
1.1 Near-Earth Space Environment . . . . .	1
1.1.1 Ionosphere and Plasmasphere . . . . .	2
1.1.2 Van Allen Radiation Belts . . . . .	3
1.2 Electromagnetic Waves Radiated by Lightning . . . . .	6
1.2.1 Sferics . . . . .	7
1.2.2 Whistlers . . . . .	7
1.3 Interaction of Whistlers with Electrons . . . . .	12
1.4 Motivation and Organization of Thesis . . . . .	14
<b>2 0<sup>+</sup> Whistler Detector</b>	<b>16</b>
2.1 Motivation and Previous Work . . . . .	16
2.2 Description of Algorithm . . . . .	18
2.2.1 Spectrogram . . . . .	19
2.2.2 Forming 0 <sup>+</sup> Whistler Shapes . . . . .	21
2.2.3 Cross-Correlation with 0 <sup>+</sup> Whistler Shapes . . . . .	23
2.2.4 Summary of Algorithm Parameters . . . . .	26
2.3 Characterization of Algorithm . . . . .	26
2.3.1 0 <sup>+</sup> Whistler Catalog . . . . .	27
2.3.2 Comparison with Algorithm . . . . .	28

2.4	Suggestions for Improvement . . . . .	31
<b>3</b>	<b>Comparison between the FWM and DEMETER</b>	<b>33</b>
3.1	Description of Data Sources and Models . . . . .	33
3.1.1	DEMETER . . . . .	34
3.1.2	National Lightning Detection Network (NLDN) . . . . .	35
3.1.3	Full Wave Method . . . . .	36
3.2	Whistler Comparison Procedure . . . . .	38
3.2.1	Identification of $0^+$ Whistlers . . . . .	38
3.2.2	Pairing $0^+$ Whistlers with NLDN Stroke Data . . . . .	39
3.2.3	Isolating $0^+$ Whistlers in DEMETER Data . . . . .	41
3.3	Results . . . . .	44
3.3.1	Best Fit Estimated Signal to Noise Ratio . . . . .	44
3.3.2	Spectrum of $0^+$ Whistlers over Horizontal Distance . . . . .	46
3.3.3	Map of $0^+$ Whistler Energy . . . . .	47
3.4	Discussion . . . . .	50
3.5	Conclusions . . . . .	55
<b>4</b>	<b>Global Upgoing Lightning Power</b>	<b>57</b>
4.1	Methodology . . . . .	57
4.1.1	Global Lightning Dataset (GLD360) . . . . .	58
4.1.2	Simulation Size . . . . .	59
4.1.3	Frequency Bandwidth . . . . .	63
4.1.4	Orientation of Earth's Magnetic Field . . . . .	64
4.1.5	Ionospheric Profiles . . . . .	65
4.1.6	Procedure to Compute Power Flux . . . . .	67
4.2	Results . . . . .	69
4.2.1	Global Average Power Flux . . . . .	69
4.2.2	Power Through a Given $L$ -shell . . . . .	70
4.2.3	Nighttime and Daytime Dependence . . . . .	71
4.2.4	Seasonal Dependence . . . . .	72
4.3	Discussion . . . . .	72

4.4	Conclusions . . . . .	77
<b>5</b>	<b>Conclusions and Suggestions for Future Work</b>	<b>78</b>
5.1	Conclusions . . . . .	78
5.2	Suggestions For Future Work . . . . .	79
5.2.1	0 <sup>+</sup> Whistler Detection Algorithm . . . . .	79
5.2.2	Comparison of FWM and DEMETER Measurements . . . . .	81
5.2.3	Global Estimate of Lightning Energy . . . . .	81
<b>A</b>	<b>FPGA on TARANIS Satellite</b>	<b>82</b>
A.1	System Architecture . . . . .	82
A.1.1	Decimator . . . . .	83
A.1.2	Spectrogram . . . . .	85
A.1.3	Algorithm Computation . . . . .	88
A.2	Input and Output Description . . . . .	88
A.2.1	Input Command/Configuration Bytes . . . . .	89
A.2.2	Output Data Format . . . . .	91
	<b>Bibliography</b>	<b>94</b>

# List of Tables

2.1	Algorithm Parameters and Their Values . . . . .	27
2.2	Algorithm Parameters for Optimum Results . . . . .	31
2.3	Optimum Results for the Algorithm Parameters from Table 2.2 . . .	31
3.1	DEMETER Bust Mode Passes with Lightning/0 <sup>+</sup> Whistler Pairs . . .	45
A.1	Science Mode Options . . . . .	89
A.2	Test Mode Descriptions . . . . .	90
A.3	Dispersion Constants according to LSBs of Input Byte 3 . . . . .	92



# List of Figures

1.1	Near-Earth Space . . . . .	2
1.2	Radiation Belt Particle Trajectories . . . . .	5
1.3	Whistler Propagation . . . . .	9
1.4	Appleton-Hartree QL $\omega$ - $k$ Diagram . . . . .	11
1.5	Whistler Resonance with Electron . . . . .	13
2.1	Example $0^+$ Whistlers . . . . .	19
2.2	Whistler Coefficient Matrix . . . . .	23
2.3	Algorithm Computation over DEMETER Data . . . . .	25
2.4	Possible Probability of Whistler Given $T$ . . . . .	30
3.1	Example DEMETER and NLDN Data . . . . .	35
3.2	Procedure to Dechirp and Isolate $0^+$ Whistlers . . . . .	42
3.3	Histogram of Signal-to-Noise Ratios . . . . .	46
3.4	Median Whistler Amplitude over Horizontal Distance . . . . .	48
3.5	Histogram of Simulated to Measured $0^+$ Whistler Energy for Different Frequencies . . . . .	49
3.6	$0^+$ Whistler Energy over North/South and East/West Distance . . . . .	50
3.7	Histograms of the Simulated to Measured $0^+$ Whistler Energy for Hor- izontal Distance . . . . .	51
3.8	DEMETER and FWM Refractive Index . . . . .	54
4.1	GLD360 Lighting Return Stroke Peak Current Density . . . . .	58
4.2	FWM Upgoing Power Flux at Various Altitudes . . . . .	61

4.3	FWM Upgoing Power Flux over Lateral Extent . . . . .	62
4.4	Upgoing Power Flux over Frequency . . . . .	63
4.5	Earth's Magnetic Field Inclination . . . . .	65
4.6	Earth's Magnetic Field Declination . . . . .	66
4.7	Electron Density Profiles . . . . .	67
4.8	Total Average Upgoing Power Flux . . . . .	69
4.9	Average Power vs. $L$ -shell . . . . .	70
4.10	Total Average Power During the Day and Night . . . . .	71
4.11	Average Power in Four Seasons . . . . .	73
4.12	Global Estimate Compared with DEMETER and <i>Colman and Starks</i> [2013] . . . . .	76
A.1	Block Diagram of the $0^+$ Detector . . . . .	83
A.2	Decimator by $M$ . . . . .	84
A.3	Cascaded Integrator Comb (CIC) Filter . . . . .	84
A.4	ZPD Decimator Frequency Response . . . . .	86
A.5	STFT Windowing Function . . . . .	87

# Chapter 1

## Introduction

Across the globe, lightning flashes on average between 40 and 50 times every second [*Christian et al., 2003*]. Not only does lightning produce a loud thunder clap and a brilliant flash of light within or below the clouds, it also radiates electromagnetic radiation that can have far reaching effects across the globe and into near-Earth space. The objective of the research presented in this thesis is to thoroughly quantify the electromagnetic wave energy input into the Earth’s radiation belts by lightning discharges. Before describing our methodology of undertaking that effort, what follows in the present chapter is some important introductory information essential for understanding our goals and motivation. A particular emphasis is placed where possible on the history of discoveries in the particular topic.

### 1.1 Near-Earth Space Environment

The near-Earth space environment is generally accepted to start around 100 km above the Earth’s surface and consists of a number of different regions with different characteristics and properties. Three regions of near-Earth space are described in this section, the relative positions of which are illustrated in Figure [1.1](#).

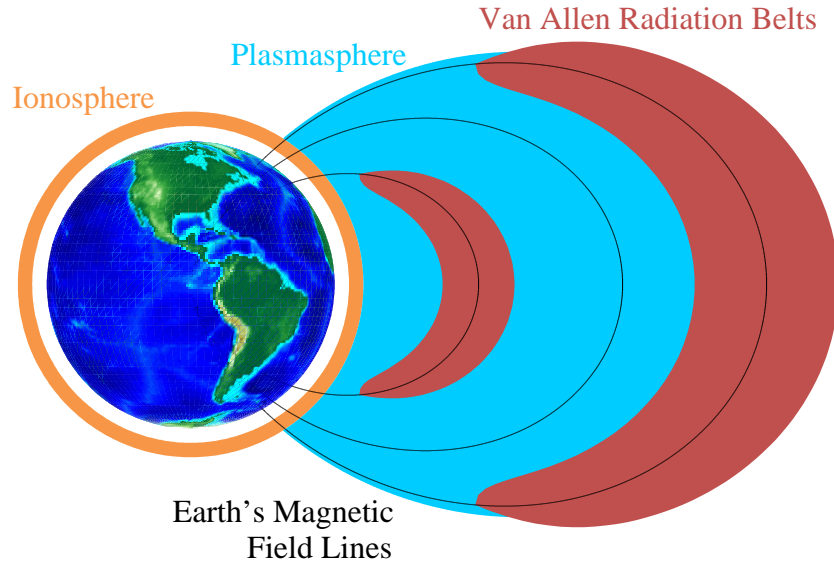


**Figure 1.1:** Regions of the near-Earth space environment (not to scale). The ionosphere is shown in orange, the plasmasphere is light blue, and the Van Allen radiation belts are in red.

### 1.1.1 Ionosphere and Plasmasphere

The Earth's atmosphere transitions from a neutral gas to a partially ionized, conducting plasma beginning at a few tens of kilometers above the surface. The presence of a conducting layer of the atmosphere was first postulated independently and almost simultaneously by *Kennelly* [1902] and *Heaviside* [1902] to explain Guglielmo Marconi's first trans-Atlantic radio transmission the previous year. Noting a difference between daytime and nighttime propagation of the radio signals, *Lodge* [1902] was the first to correctly propose that ultra-violet radiation from the sun might be responsible for the conducting layer, and *Taylor* [1903] later independently hypothesized the same process to explain the layer's existence. The ionosphere was eventually confirmed experimentally by *Appleton and Barnett* [1925] and *Breit and Tuve* [1925].

The ionosphere is generally said to consist of three separate regions, or layers: The *D* region, which is present only during the day time and starts at around 60 km, the *E* region, beginning at an altitude of about 80 km up to a little over 100 km, and finally the *F* region, which extends at least up to 1000 km beyond the *E* region.

The names of the regions come from Edward V. Appleton, who incidentally won the Nobel Prize in Physics in 1947 for his work on the ionosphere: He initially used the letter *E* to refer to the reflected electric field from the first layer that he discovered. He later found a layer above the first layer, which he denoted *F* as the next letter in the alphabet, and after that discovered still another layer below the *E* region which he termed *D* for the previous letter. Rather than begin the lettering at *A* for the lowest layer, he reserved the alphabet's first three letters for then as yet possibly undiscovered layers lower than the *D* region.

At high enough altitudes, the atmosphere becomes fully ionized, after which it is known as the plasmasphere. The upper edge of the plasmasphere, known as the plasmopause, extends to as many as three to seven Earth radii away from the planet. The existence of this region was possibly first postulated by *Storey* [1953] in his study of whistlers. The plasmopause was discovered after an analysis of VLF whistler data showed a marked decrease in the plasma density by several orders of magnitude beyond a certain altitude [*Carpenter*, 1963].

### 1.1.2 Van Allen Radiation Belts

In contrast to the relatively cold (i.e., low energy  $\sim 1$  eV) electrons and ions comprising the ionosphere and plasmasphere, there is also a region of space near Earth with relatively high energy ( $>100$  keV) charged particles known as the Van Allen radiation belts. While the possibility of charged particles being trapped by Earth's magnetic field had been previously considered, the existence of the radiation belts was not confirmed until 1958, when a Geiger counter placed on board the first American satellite, Explorer 1—built under the direction of James Van Allen, after whom the radiation belts are named—measured such high counting rates that it likely saturated. Later, measurements from a Geiger counter on the Pioneer 3 spacecraft indicated the presence of both an inner and outer radiation belt [*Van Allen and Frank*, 1959], and research on the nature and structure of the belts is still ongoing. In 2012, for example, two spacecraft originally known as the Radiation Belt Space Probes, later being renamed the Van Allen Probes, were launched by NASA to fly through and extensively

study this region of space. Having such large energies, particles in the radiation belts can be harmful to both spacecraft and astronauts passing through them [see, e.g., [Baker, 2002](#)], and thus a clear understanding of their effects is vital for the future of space flight and exploration.

From the Lorentz force equation,  $\vec{F} = q(\vec{E} + \vec{v} \times \vec{B})$ , where  $\vec{F}$  is the force on the particle,  $q$  is the particle charge,  $\vec{E}$  is the ambient electric field,  $\vec{v}$  is the particle velocity, and  $\vec{B}$  is the ambient magnetic field, one can show a charged particle in a uniform magnetic field in the absence of an electric field will gyrate with a gyroradius  $r_g$  given by

$$r_g = \frac{p_{\perp}}{qB}, \quad (1.1)$$

where  $p_{\perp}$  is the component of the particle momentum perpendicular to the magnetic field. In this framework, the trajectory of a particle is usually described in terms of the motion of the center of the gyroradius circle, known as the guiding center, with a gyration around that center implied. Another parameter used to describe motion of a charged particle in a magnetic field is the pitch angle  $\alpha$ , which is the angle between the particle velocity vector and the magnetic field vector. A particle with a pitch angle of  $\alpha = 90^\circ$  moves entirely perpendicular to the magnetic field and therefore moves in a circle with a radius given by (1.1). Conversely, a particle with a pitch angle of either  $\alpha = 0^\circ$  or  $\alpha = 180^\circ$  moves exactly parallel or antiparallel to the magnetic field and continues along that path without gyration.

Earth's magnetic field, of course, is not uniform but resembles that of a dipole, and as a result, the electrons and ions comprising the radiation belts undergo three types of periodic motion:

1. Gyration about the Earth's magnetic field lines,
2. A bouncing of the guiding center up and down the magnetic field lines, and
3. A slow longitudinal drift of the guiding center around the Earth, with electrons drifting eastward and positive ions drifting westward.

A diagram demonstrating these three types of motion is given in [Figure 1.2](#).

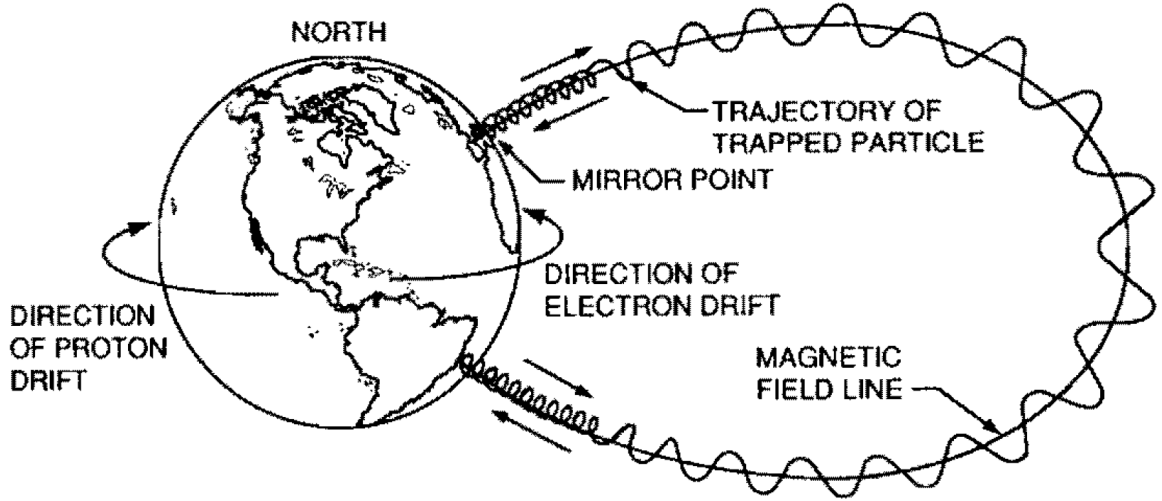


**Figure 1.2:** Different types of motion of electrons and protons trapped in the Van Allen Radiation Belts. Both electrons and protons bounce along a magnetic field line, while electrons drift east and protons drift west. [Walt, 1994, Figure 2.7].

For any particle undergoing periodic motion, the action integral given by  $\oint p dq$ , where  $p$  and  $q$  are the particle momentum and generalized coordinate along the period, is constant. By integrating over the particle gyration around the magnetic field lines (the first type of motion listed above) and scaling the result by some constant factors, one can show that a quantity known as the first adiabatic invariant  $\mu$ , which is given by

$$\mu = \frac{p_{\perp}^2}{2B}, \quad (1.2)$$

must be conserved; therefore, because the magnitude of the magnetic field increases along a field line, the particle perpendicular momentum and hence velocity must also increase. Because the particle kinetic energy must be conserved, its parallel velocity must decrease in order to maintain a constant speed along its path of motion. Eventually, the particle parallel velocity goes to zero, and so the particle velocity will be entirely perpendicular to the magnetic field ( $\alpha = 90^\circ$ ), after which the particle reverses course due to the spatial magnetic field gradient [Inan and Golkowski, 2010, p. 37] and begins moving back along the field line from whence it came. If the point at which the particle reverses course, known as the mirror point, is sufficiently high

in altitude above the Earth, the particle remains trapped by the Earth's magnetic field and continues in that path. However, if the mirror point occurs at low enough altitudes where the atmospheric density is high, the particle will be absorbed by the atmosphere and lost from the radiation belts. It should be clear that the further the particle pitch angle at the equator is from  $\alpha = 90^\circ$ , the further along a field line that particle travels. Hence, a parameter known as the loss cone angle  $\alpha_{LC}$ , given by

$$\alpha_{LC} = \arcsin \left( \sqrt{\frac{B_{eq}}{B_a}} \right), \quad (1.3)$$

where  $B_{eq}$  is the equatorial magnetic field strength and  $B_a$  is the magnetic field strength at the altitude where the atmosphere is dense enough that the particle would be lost (typically taken as the upper edge of the atmosphere at around 100 km), can be used to define which particles remain trapped and which are lost. Specifically, particles with pitch angles in radians between  $\frac{\pi}{2} \pm \alpha_{LC}$  remain trapped, and the rest are lost.

## 1.2 Electromagnetic Waves Radiated by Lightning

The process by which thunderclouds build up large amounts of charge is still somewhat poorly understood but fortunately is not important for the purposes of the present work. Suffice it to say, after enough charge builds up in a thundercloud, the charge is neutralized in an electrostatic discharge that is referred to as a lightning discharge. Accelerating charges, like those in an electrostatic discharge such as lightning, radiate electromagnetic energy, and therefore lightning emits radio waves. Because the stroke carrying the bulk of the lightning current occurs on a time scale on the order of tens of microseconds, the radiated electromagnetic wave from lightning is primarily concentrated in the Very Low Frequency (VLF) band, generally defined as lying between 3 kHz and 30 kHz (wavelengths between 100 km and 10 km) [*Uman, 1987*, p. 118]. Most of the energy radiated by lightning propagates near the Earth's surface, but some of the energy propagates away from Earth and into near-Earth space. It is the latter energy that is the main concern of this thesis, although we



briefly introduce both types of waves in the following sections.

### 1.2.1 Sferics

Both being relatively good electrical conductors at VLF, the surface of the Earth and the ionosphere form a waveguide known as the Earth-ionosphere waveguide through which electromagnetic waves can propagate. Radio waves emitted by lightning in particular propagate efficiently through this waveguide with less than 3 dB of attenuation per 1000 km [*Davies, 1990*, p. 387]. The radio waves from lightning that propagate within the Earth-ionosphere waveguide are called radio atmospherics, or “sferics” for short.

### 1.2.2 Whistlers

Soldiers in World War I made some of the earliest, although likely not the first, reported observations of the electromagnetic waves which came to be known as whistlers [*Barkhausen, 1919, 1930*]. The telephone wires used to communicate with the front lines were poorly insulated and thus induced significant ground currents which could be measured some distance away by inserting metallic probes into the ground a few hundred meters apart and connecting the leads to a high-gain amplifier. Thus, the technique was utilized frequently to listen in on the enemy’s communications. Occasionally, the eavesdroppers heard “the grenades fly” in their listening equipment, sometimes so loudly that any enemy conversations were completely drowned out. The sounds could best be described using letters as a “pēou,” descending in tone over time almost like a whistle, hence their eventual naming as whistlers. While a meteorological correlation was noted in the sounds, their source remained a mystery for more than thirty years afterwards. Research on the phenomenon did continue, with for example *Eckersley* [1935] showing that the characteristic frequency vs. time dependence of a whistler could result from an impulsive wave propagating through and getting dispersed by the ionosphere, but the onset of World War II hindered further work on the topic.

Finally, *Storey* [1953] was able to propose a satisfying mechanism for the generation of whistlers by collecting an extensive catalog of whistlers and from that deriving a number of important patterns. First, he determined that loud (i.e., strong) whistlers could either be preceded by a loud “click” (atmospheric) or none at all, while weak whistlers never were preceded by a click. He also noted that whistlers preceded by clicks were dispersed about twice as much as those not preceded by clicks. Additionally, utilizing the simple whistler dispersion relation  $t \propto f^{-\frac{1}{2}}$  found previously by *Eckersley* [1935], he extrapolated graphs of the time vs. frequency measured for the whistlers up to an infinite frequency and found that the corresponding time was the same as that of the whistler’s preceding click, if there was one. Finally, he was able to split the whistler “echoes” (i.e., one whistler followed some time later by a more dispersed whistler) he measured into two groups: one with dispersions increasing in ratios of 1 : 2 : 3 : 4 when preceded by a click but in ratios of 1 : 3 : 5 : 7 when not preceded by a click.

From all of those observations, Storey concluded that whistlers must be the result of sferics from lightning propagating out into space approximately along the Earth’s magnetic field lines to the opposite hemisphere, at which point some of the energy would propagate to the ground and the rest would reflect back to the original hemisphere, as demonstrated in Figure 16 from his paper (reproduced as Figure 1.3 here). We now denote whistlers by the number of times they have crossed the equator and whether they are upgoing or downgoing: The initial upgoing whistler is called a  $0^+$ , followed by the downgoing  $1^-$ , and then the reflected upgoing  $1^+$ , and so on. Interestingly, Storey noted that the plasma densities required to produce the whistlers with dispersions as large as he observed were significantly larger than the ionosphere was previously thought to contain, and so ultimately his work helped contribute to our understanding of the plasmasphere as a region of significant plasma density extending high in altitude from the ground. Finally, owing to the efficient propagation of sferics through the Earth-ionosphere waveguide, it should be noted that  $0^+$  whistlers have been observed up to 1500 km from their parent lightning stroke [*Chum et al.*, 2006].

Readers interested in a more detailed exposition on the history of whistler studies are directed to *Helliwell* [1965, ch. 2].

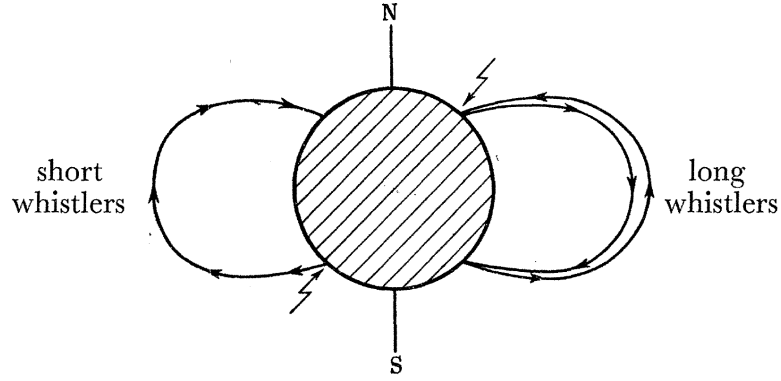


**Figure 1.3:** Whistler propagation according to *Storey* [1953, Figure 16]. For a northern observer, short whistlers originate in the southern hemisphere and propagate approximately along the Earth’s magnetic field line up to the northern hemisphere. Longer whistlers, which are sometimes preceded by clicks, originate in the northern hemisphere and reflect at the southern hemisphere back to the north.

Because whistlers propagate through the plasma of the ionosphere and the plasmasphere, an understanding of how electromagnetic waves propagate through a plasma is necessary for a complete description of whistlers. In general, the complex refractive index  $n$  of an electromagnetic wave propagating through a homogenous plasma with a wave normal at an angle  $\theta$  from the ambient magnetic field is given by the so-called Appleton-Hartree equation:

$$n^2 = \frac{c^2 k^2}{\omega^2} = 1 - \frac{X}{1 - jZ - \frac{Y^2 \sin^2 \theta}{2(1 - X - jZ)} \pm \sqrt{\left(\frac{Y^2 \sin^2 \theta}{2(1 - X - jZ)}\right)^2 + (Y \cos \theta)^2}} \quad (1.4)$$

where  $c$  is the speed of light in vacuum,  $k$  is the wave number,  $\omega$  is the radian frequency of the propagating wave,  $j = \sqrt{-1}$  is the imaginary unit, and

$$X = \frac{\omega_{pe}^2}{\omega^2} = \frac{q_e^2 N_e}{\epsilon_0 m_e \omega^2}, \quad (1.5a)$$

$$Y = \frac{\omega_{ce}}{\omega} = \frac{q_e B_0}{m_e \omega}, \quad (1.5b)$$

$$Z = \frac{\nu}{\omega}, \quad (1.5c)$$

$\omega_{pe}$  is the plasma frequency,  $q_e$  is the electric charge of an electron,  $N_e$  is the number density of electrons in the plasma,  $\epsilon_0$  is the permittivity of free space,  $m_e$  is the mass of an electron,  $\omega_{ce}$  is the gyrofrequency of an electron in an ambient magnetic field with strength  $B_0$ , and  $\nu$  is the collision frequency between electrons and other particles.

Because (1.4) is quite complicated, a simplification to it known as the quasi-longitudinal (QL) approximation is sometimes invoked to make it more tractable. The QL approximation generally holds for small angles  $\theta$ , or more specifically when

$$\frac{Y^2 \sin^4 \theta}{4 \cos^2 \theta} \ll |1 - X - jZ|^2. \quad (1.6)$$

In that case, (1.4) reduces to

$$n^2 \simeq 1 - \frac{X}{1 - jZ \pm |Y \cos \theta|}. \quad (1.7)$$

The + sign in (1.7) describes a left hand circularly polarized (LHCP) wave, while the – sign corresponds to a right hand circularly polarized (RHCP) wave. It is relatively straightforward to show that (1.7) has two cut-off frequencies (when the real part of the refractive index goes to zero), which we denote as  $\omega_L$  and  $\omega_R$  for the two different wave polarizations, at

$$\omega_{L,R} = \sqrt{\omega_{pe}^2 + \frac{\omega_{ce}^2}{4}} \mp \frac{\omega_{ce}}{2}. \quad (1.8)$$

A graph of  $\omega$  vs.  $k$  for (1.7) is given in Figure 1.4. The blue curve is the RHCP wave, the green curve is the LHCP wave, and the red line corresponds to the case for which the refractive index is unity (i.e., free space propagation). At high frequencies, the dispersion relation for RHCP and LHCP waves approach that of free space propagation. RHCP waves experience a cut-off at  $\omega_R$ , immediately below which they cannot propagate, and LHCP waves have a cut-off at a lower frequency of  $\omega_L$ . There is one more branch for frequencies below the electron cyclotron frequency  $\omega_{ce}$  where RHCP waves can propagate, and this branch is called the whistler mode because it is the branch occupied by whistlers. So whistlers are essentially RHCP electromagnetic waves that propagate approximately along the magnetic field lines within a plasma.

To calculate the group velocity of a whistler-mode wave, it is helpful to neglect

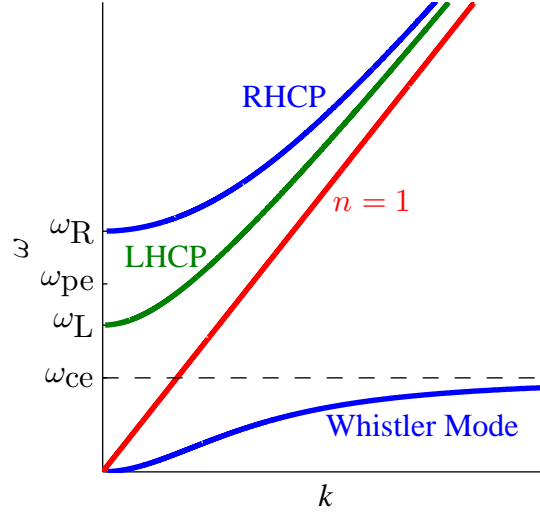


**Figure 1.4:**  $\omega$ - $k$  diagram of the Appleton-Hartree equation under the QL approximation. The blue curve is the RHCP branch, and the green curve is the LHCP branch, while the red line represents a unity refractive index. The whistler mode occurs for  $\omega < \omega_{ce}$ .

collisions and approximate the refractive index as

$$n^2 \simeq \frac{X}{|Y \cos \theta| - 1}. \quad (1.9)$$

Essentially, we have assumed that the second term in (1.7) (i.e., the fraction after the minus sign) dominates such that the 1 can be dropped. This is equivalent to assuming  $\omega_{pe}^2 \gg \omega_{ce}^2$ , which is generally believed to be true in the ionosphere. Then, one can show that the group velocity is

$$v_g \stackrel{\text{def}}{=} \frac{\partial k}{\partial \omega} = 2c \frac{\sqrt{\omega}(\omega_{ce} \cos \theta - \omega)^{3/2}}{\omega_{pe} \omega_{ce} \cos \theta}. \quad (1.10)$$

For low frequencies (specifically, when  $\omega \ll \omega_{ce} \cos \theta$ ), (1.10) can be further reduced to

$$v_g \simeq 2c \frac{\sqrt{\omega_{ce} \cos \theta}}{\omega_{pe}} \sqrt{\omega}, \quad (1.11)$$

and hence the group velocity is proportional to  $\sqrt{\omega}$ . That means the plasma is dispersive, and higher frequency components will travel through the medium faster than lower frequencies. Recall that the lightning emits a broadband spectrum of electromagnetic waves in a relatively short duration of time. After propagating through the plasma of the ionosphere, that initial impulse spreads out in time, with the higher frequencies arriving at their destination sooner than lower frequencies.

### 1.3 Interaction of Whistlers with Radiation Belt Electrons

It turns out that an electron trapped in the Earth's magnetic field gyrates along the field lines in the same sense (right handed) that whistler-mode waves are polarized, as illustrated in Figure 1.5 for the case of a whistler propagating exactly along the magnetic field line (i.e., for  $\theta = 0$ ). In general, the wave electric field  $\vec{E}_w$  and magnetic field  $\vec{B}_w$  rotate in the same sense as the electron perpendicular velocity  $\vec{v}_\perp$ . The electron rotates with a frequency of  $\omega_{ce}$  and observes, in the non-relativistic case, the whistler rotating at a Doppler shifted frequency of  $\omega \pm kv_\parallel$  for an electron moving towards or away from the oncoming whistler-mode wave, respectively. At any point in time  $t$ , then, the so-called Larmor phase angle between the wave magnetic field and the electron perpendicular velocity is given by

$$\phi(t) = \left[ \omega_{ce} - (\omega \pm kv_\parallel) \right] t + \phi_0, \quad (1.12)$$

where  $\phi_0$  is the initial angle at  $t = 0$ . The wave fields exert a Lorentz force on the electron of

$$\vec{F} = -q_e \left( \vec{E}_w + \vec{v} \times \vec{B}_w \right), \quad (1.13)$$

which causes both a change in the kinetic energy via the  $q_e \vec{E}_w$  acceleration and also the direction of the momentum from the  $q_e (\vec{v} \times \vec{B}_w)$  term. For a whistler-mode wave, the magnetic field effect is substantially more important due to the relatively high value of the wave refractive index. As a result, the dominant effect of the

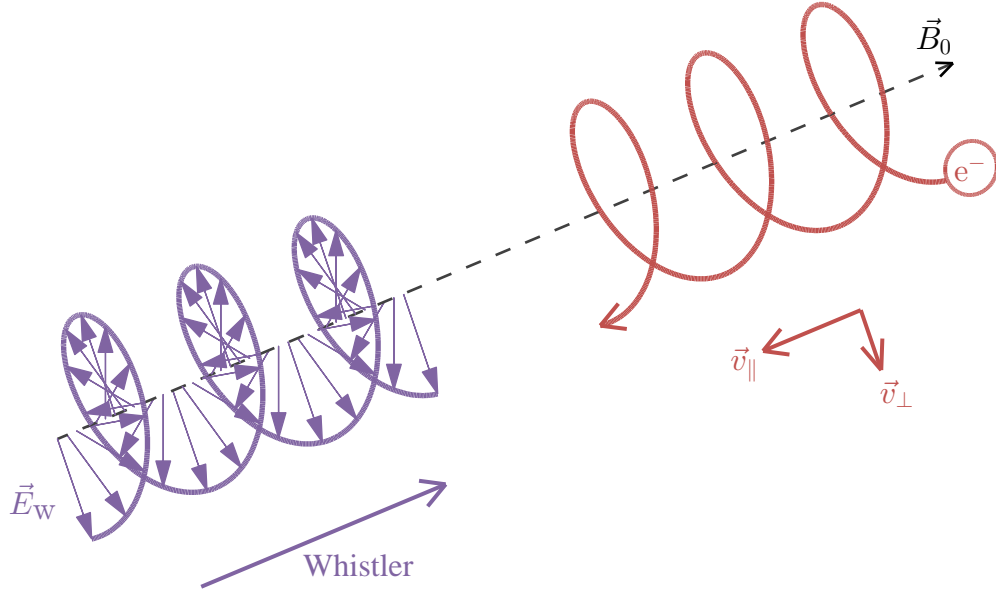


**Figure 1.5:** Whistler resonance with electron. An incoming whistler rotates with the same polarization that an electron gyrates around the magnetic field.

wave on the electron is a modification of the direction of its momentum, or in other words, the pitch angle.

Most of the time, the cumulative deflections in pitch angle are not large because the phase angle given by (1.12) is a rapidly changing function of time. But when  $\omega_{ce} = \omega + kv_{\parallel}$ , the time dependence goes away, and the wave, now said to be in resonance with the electron, can cause significant cumulative scattering of the electron pitch angles. In other words, for the case of the electron moving towards the whistler, which is given by the  $+$  sign in the Doppler shifted frequency, the electron can acquire significant amounts of pitch angle change. While it may not be obvious, it is nevertheless the case that the electron will subsequently travel further down the magnetic field line before bouncing back. In fact, whistlers can cause such a change in electron pitch angles that a once stably trapped electron falls within the loss cone and therefore is removed from the radiation belts, a process called lightning-induced electron precipitation.

This mechanism, i.e. the removal of electrons from the radiation belts via pitch angle scattering by waves, was proposed soon after the radiation belts were first discovered to explain the observed drop in electron populations in the radiation belts at

around  $L \sim 2.5$  [*Dungey, 1963; Cornwall, 1964*]. Since then, there has been extensive debate on the importance of lightning-generated whistlers in controlling radiation belt populations. Utilizing an estimated whistler wave amplitude of 10 pT occurring 3% of the time and uniformly distributed between  $1.2 \leq L \leq 4$  derived from *Burgess and Inan [1993]*, *Abel and Thorne [1998a,b]* modeled the effect of lightning-generated whistlers and showed a significant drop in electron lifetimes due to those waves. Other studies have borne out that same conclusion [*Bortnik et al., 2003; Gemelos et al., 2009*], but *Meredith et al. [2007]* has instead suggested that plasmaspheric hiss, another whistler-mode wave present in the radiation belts, contributes much more significantly to electron loss rates than lightning-generated whistlers.

## 1.4 Motivation and Organization of Thesis

Previous estimates of the amount of VLF wave energy that escapes the Earth-ionosphere waveguide and propagates into the plasmasphere and radiation belts have typically relied on a set of sub-ionospheric absorption curves derived by *Helliwell [1965, Figure 3-35]*. However, use of those curves were called into question after *Starks et al. [2008]* showed that a number of ionospheric propagation models coupled with the Helliwell absorption curves when applied to VLF transmitter signals from the ground tended to overestimate the field strengths measured on five different satellites in the plasmasphere by at least 20 dB at night and 10 dB during the day. Various reasons for the discrepancy have been investigated, including loss of VLF electromagnetic wave energy due to conversion to quasi-electrostatic mode waves after scattering off of irregularities in the background electron plasma density [*Bell et al., 2008; Foust et al., 2010*] and nonlinear interactions due to parametric plasma instabilities driven by the (high power) VLF transmitters [*Mishin et al., 2010; Galinsky et al., 2011*], but no one could account for the discrepancy, especially one as large as 20 dB.

Subsequently, the trans-ionospheric VLF propagation model of *Lehtinen and Inan [2008, 2009]*, a frequency domain finite element electromagnetic full wave simulation (hereafter referred to as the full wave method (FWM)), was used to simulate the propagation of VLF transmitter waves into the plasmasphere. *Lehtinen and Inan*



[2009] compared the model to satellite measurements by DE-1 and DEMETER over two VLF transmitters and showed an overestimate of the field strengths by about 10 dB; however, an expanded study encompassing additional passes of DEMETER over 9 different transmitters demonstrated the FWM simulated field strengths fell within 5 dB of the measured fields both at night and during the day even though the FWM simulation does not account for plasma density irregularities [*Cohen and Inan, 2012; Cohen et al., 2012*]. It was then determined using the FWM that parameters such as incidence angle, wave polarization, and the ionospheric profile, which cannot be varied when using the Helliwell absorption curves, have a strong impact on the transmission of VLF waves from the ground into the ionosphere and hence could explain the discrepancy that *Starks et al. [2008]* found using the Helliwell absorption curves [*Graf et al., 2013*].

It should be emphasized that the aforementioned studies all focused on anthropogenic VLF transmitter signals. Lightning-generated whistlers, the other strong terrestrial source of VLF waves propagating into the plasmasphere, have yet to be checked despite the discrepancies *Starks et al. [2008]* reported. The research presented in this thesis thus attempts to apply a similarly thorough treatment for the determination of the energy input into the plasmasphere by lightning-generated whistlers that has recently been given for the case of VLF transmitters. After the introduction just provided in this chapter, the next chapter presents an algorithm to detect  $0^+$  whistlers in electric or magnetic field data from a low orbiting spacecraft, although in principal the algorithm could be applied to the detection of any kind of whistler. In the chapter that follows, results of a comparison made between FWM simulations of lightning-generated whistlers and measurements from the DEMETER satellite of  $0^+$  whistlers identified using the algorithm previously described in Chapter 2 are given. The subsequent chapter then explains how calculations of the global lightning energy injected into the plasmasphere are made along with their results. Finally, the last chapter offers some conclusions and suggestions for future work to expand on what has been presented here.

# Chapter 2

## $0^+$ Whistler Detector

In an effort to quantify the amount of lightning energy propagating from the Earth into the plasmasphere from satellite data, we developed an algorithm to automatically detect  $0^+$  whistlers on low-Earth orbiting satellites. The TARANIS satellite, expected to be launched in 2018 and whose mission broadly speaking is to study transient luminous events and other lightning related phenomena, is slated to carry an instrument to automatically detect  $0^+$  whistlers and report information about them to the ground. The instrument, known as the  $0^+$  detector or ZPD, is deployed as an Actel AX 2000 field programmable gate array (FPGA). What follows in this chapter is a detailed description of the detection algorithm.

### 2.1 Motivation and Previous Work

Ideally, the full electromagnetic wave data from the TARANIS satellite could be transmitted to the ground for complete analysis, but unfortunately telemetry limitations make such a proposition impossible. Yet information on the amount and strength on the  $0^+$  whistlers in particular seen by a satellite could provide a means to answering fundamental questions related to the amount of lightning energy that is present in the plasmasphere. A system to collect such information does not currently exist, although some work has been done on solving this problem, most notably using the DEMETER satellite.

In June 2004, the DEMETER (Detection of Electro-Magnetic Emissions Transmitted from Earthquake Regions) satellite was launched into Earth orbit at an altitude of 710 km (which was subsequently lowered to 660 km in December 2005) and remained in operation until the end of 2010. Among DEMETER's many objectives was to measure the electromagnetic spectrum at the satellite altitude using two different instruments: the Instrument Champ Electrique (ICE) to measure the electric field [Berthelier *et al.*, 2006] and Instrument Magnetometer Search-Coil (IMSC) for the magnetic field [Parrot *et al.*, 2006]. Therefore, the satellite offers a rich source of data for the study of  $0^+$  whistlers. Additionally, because it was placed into a circular, sun-synchronous orbit allowing it to pass over a given part of the Earth close to 10:15 Local Solar Time (LST) in the morning and 22:15 LST at night, DEMETER had the opportunity to measure  $0^+$  whistlers propagating through both daytime and nighttime ionospheric profiles.

The electromagnetic sensors on DEMETER had two primary modes of operation within the VLF band: a survey mode that continuously provided spectra every 2 seconds of a single field component up to 20 kHz with 20 Hz resolution and a burst mode that, while active only part of the time, provided full waveform data sampled at 40 kHz of a single field component. A study by Fiser *et al.* [2010] applied a similar technique to ours of computing cross-correlations of known  $0^+$  whistler shapes with the spectrogram to identify  $0^+$  whistlers in burst mode data from DEMETER to measure the  $0^+$  whistler intensity above active thunderstorms over Europe and thus was limited in geographical scope. Colman and Starks [2013], on the other hand, utilized survey mode data to develop a global map of  $0^+$  whistler intensity, but survey mode data lacks the resolution to distinguish  $0^+$  whistlers from other types of waves, such as chorus and hiss. Finally, it should be noted that there was a configurable neural network onboard that could be configured to identify certain kinds of waves, and the instrument was initially used to identify whistlers of all kinds, both fractional hop  $0^+$  whistlers and those with larger dispersions [Elie *et al.*, 1999], although we are not aware of any studies analyzing data from that instrument to deduce an estimate of the global upgoing lightning energy.

Limitations both in the available downlink data throughput from the TARANIS

satellite and the aforementioned studies led us to develop an algorithm that automatically detects  $0^+$  whistlers. The algorithm is computationally simple enough to fit onto a standard Actel AX 2000 FPGA, a goal of the project, and the FPGA with the algorithm we supplied for the TARANIS mission has been allotted a downlink bandwidth of 6 kb/s. Data from the instrument is expected to contribute to our understanding of how much lightning energy is input into the plasmasphere and thereby interacts with the Van Allen radiation belts. Additionally, data will likely be useful in providing context to TARANIS's primary mission of studying lightning related phenomena and should also find application in comparisons with global lightning detection networks. The French space agency CNES has set a mission lifetime for the satellite of at least two to three years with the possibility of additional extensions.

## 2.2 Description of Algorithm

From (1.11), the low frequency approximation of the group velocity of a whistler-mode wave, one can show that the instantaneous frequency of a whistler is inversely proportional to the square of the time after the whistler is first recorded [*Helliwell, 1965*, p. 4]. That is, when plotted as a spectrogram, the frequency-time curvature of a whistler should follow a shape given by

$$t = \frac{D}{\sqrt{f}} \quad (2.1)$$

where  $D$ , known as the dispersion constant of the whistler, represents the degree to which the whistler is dispersed. Two example  $0^+$  whistlers from the electric field instrument of the DEMETER satellite [*Berthelier et al., 2006*] can be seen in Figure 2.1. The magenta curve overlaid on top of the first  $0^+$  whistler in the plot traces a line given by (2.1) with  $D = 4 \text{ s}^{1/2}$  and follows the shape of the whistler. Therefore, this whistler can be said to have a dispersion constant of  $D = 4 \text{ s}^{1/2}$ .

Broadly speaking, our algorithm identifies  $0^+$  whistlers by making spectrograms of either the electric or magnetic fields as measured by the satellite and looking for shapes in those spectrograms given by (2.1). Let the input to the algorithm

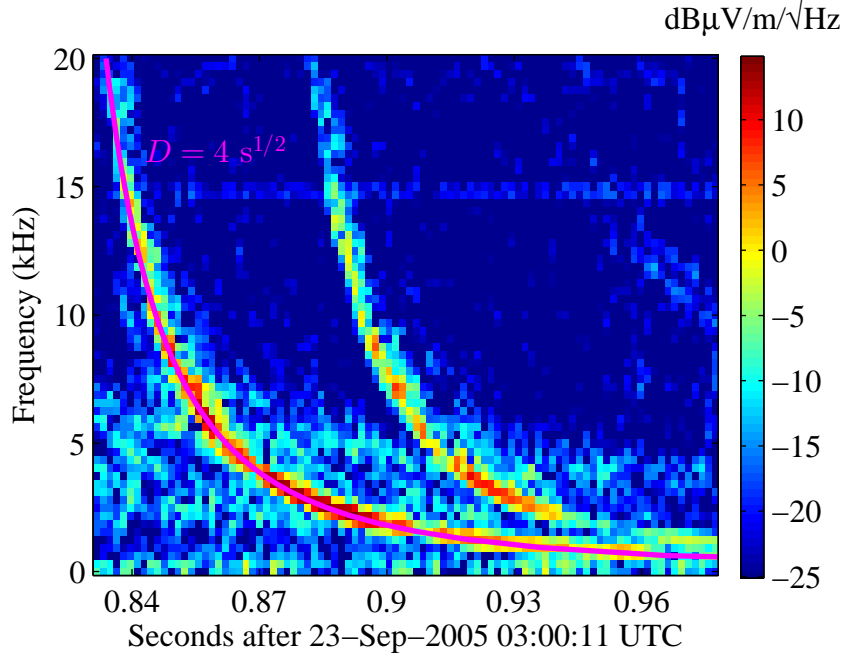


**Figure 2.1:** Example  $0^+$  whistlers measured by DEMETER’s electric field instrument. In this case, a curve shown in magenta with  $D = 4 \text{ s}^{1/2}$  in (2.1) fits the whistlers.

be a time-domain waveform given by  $x(t)$  which is then sampled at a frequency of  $f_s$  so that  $x[k] = x(k/f_s)$  is input into the algorithm for  $k = 0, 1, \dots$ . We first compute spectrograms of the input waveform and then take the cross-correlation of the spectrogram with an expected  $0^+$  whistler shape. A large value in the cross-correlation generally indicates the presence of a  $0^+$  whistler.

### 2.2.1 Spectrogram

A spectrogram is the magnitude of the short-time Fourier transform (STFT), which is defined for a time domain signal  $x[k]$ ,  $k = 0, 1, \dots$  as

$$\text{STFT}\{x[k]\} = s[m, n] = \sum_{k=0}^{N-1} \left( x[k - (N - O)n] w[k] e^{-j2\pi \frac{km}{N}} \right), \quad (2.2)$$

where the parameters of the STFT are:

- $N$  is the discrete Fourier transform (DFT) length.
- $O$  is the number of points to overlap between successive times.
- $w[k]$  is the windowing function. Also, let  $W$  be the largest  $k$  that satisfies  $w[k-1] \neq 0$  (i.e., the length of the windowing function).

Note that  $N > O$  and  $N \geq W$ . If  $x[k]$  represents a continuous time signal  $x(t)$  sampled at a frequency  $f_s$ , the value of  $s[m, n]$  estimates the spectral content of  $x(t)$  at the frequency

$$f_m = \frac{f_s}{N}m \quad (2.3)$$

(so that the spacing between frequency indices is  $\Delta f = f_s/N$ ) and at the time

$$t_n = \frac{W}{2f_s} + \frac{W-O}{f_s}n \quad (2.4)$$

for  $m = 0, 1, \dots, N/2-1$  and  $n = 0, 1, \dots$ . Therefore, the  $m$  values index in frequency and the  $n$  values index over time.

A  $0^+$  whistler is visually distinguished in a spectrogram by having some number of pixels following the shape given by (2.1) stand out, or more specifically, exceed the background noise by some margin. Therefore, we next compute a normalized spectrogram having  $C$  distinct time indices by finding all the points in the spectrogram that exceed the mean of the previous  $A$  values of the spectrogram at each frequency by some number  $N_\sigma$  standard deviations of the same previous  $A$  values. Mathematically, this process can be represented as follows: Let the magnitude of the STFT given by (2.2) (i.e., the spectrogram) be  $p[m, n]$  for  $m = 0, 1, \dots, N/2-1$  and  $n = 0, 1, \dots$ . We then compute the mean and standard deviation vectors, respectively, as

$$\mu_n[m] = \frac{1}{A} \sum_{i=1}^A p[m, n-i] \quad (2.5a)$$

$$\sigma_n[m] = \sqrt{\frac{1}{A} \sum_{i=1}^A (p[m, n-i] - \mu_n[m])^2} \quad (2.5b)$$

for all  $n \geq A$  (i.e., for all spectrogram time frames after the first  $A$  frames). Next, a normalized spectrogram with  $C$  time frames is created by computing

$$q_n[m, k] = \begin{cases} 1, & p[m, n + k] - \mu_n[m] \geq N_\sigma \sigma_n[m] \\ 0, & \text{otherwise} \end{cases} \quad (2.6)$$

for  $k = 0, 1, \dots, C - 1$  again for all  $n \geq A$ . The term  $N_\sigma$  (also denoted as  $N_{\text{std}}$ ) is a parameter of the algorithm that determines the sought for margin over which a pixel must stand out over the background noise. It is in these normalized spectrograms where  $0^+$  whistlers are sought by the algorithm.

### 2.2.2 Forming $0^+$ Whistler Shapes

The next step in the algorithm involves computing the two-dimensional cross-correlation of the normalized spectrograms by expected whistler shapes. The expected whistler shapes are matrices having  $N/2$  rows and  $C$  columns, identical to the normalized spectrograms. We denote those shapes by  $c_l[m, k]$  for  $l = 0, 1, \dots, S - 1$ , where  $S$  is the number of expected whistler shapes to check against. Thus, each  $c_l[m, k]$  represents a whistler with a dispersion constant  $D_l$ .

There are a number of different ways the expected whistler shapes  $c_l[m, k]$  could be formed. We create them by finding the pixels in a spectrogram that trace a line given by (2.1) for each dispersion constant  $D_l$  of interest. That computation is made by first converting  $t$  and  $f$  from (2.1) to unitless indices using the spacings given by (2.3) and (2.4), which results in the following unitless dispersion constant in terms of the time index  $n$  and frequency index  $m$ :

$$\frac{D_l}{\Delta t^2 \Delta f} = \left( \frac{t}{\Delta t} \right)^2 \left( \frac{f}{\Delta f} \right) = n^2 m. \quad (2.7)$$

Next, for each frequency index  $m = 0, 1, \dots, N/2 - 1$ , a vector  $u_l[m]$  is calculated by finding the time indices  $n$  that most closely match the particular dispersion

constant as computed in (2.7). Formally, this can be written as

$$u_l[m] = \arg \min_{n \in \mathbb{Z}_{\geq 0}} \left( \frac{D_l}{\Delta t^2 \Delta f} - n^2 m \right). \quad (2.8)$$

Let the vector  $v_l[m]$  be defined as

$$v_l[m] = \begin{cases} u_l[0] - u_l \left[ \frac{N}{2} - 1 \right] + 1, & m < 0 \\ u_l[m] - u_l \left[ \frac{N}{2} - 1 \right] + 1, & 0 \leq m < \frac{N}{2} \\ 1, & m \geq \frac{N}{2} \end{cases}. \quad (2.9)$$

Essentially, this is the  $u_l[m]$  vector normalized to end with a minimum value of 1 and defined over all  $m$  by fixing values outside the range of frequency indices to the value at the closest frequency index. The vector  $v_l[m]$  gives the coordinates in  $c_l[m, k]$  that trace the line of a  $0^+$  whistler is expected to make in a spectrogram.

Finally, the whistler shapes are computed from  $v_l[m]$  by making the surrounding pixels either +1 or -1 according to:

$$c_l[m, k] = \begin{cases} +1, & v_l[m] < C \text{ and } v_l[m] \leq k \leq v_l[m-1] + 1 \\ -1, & v_l[m] < C \text{ and} \\ & v_l[m+1] \leq k+1 \leq v_l[m] \text{ or } v_l[m-1] \leq k-2 \leq v_l[m-2] \\ 0, & \text{otherwise} \end{cases}. \quad (2.10)$$

An example whistler shape coefficient matrix for  $D = 4 \text{ s}^{1/2}$  (the same dispersion constant from Figure 2.1),  $N = 128$ , and  $C = 48$  (incidentally, the same values used by the ZPD FPGA) is given in Figure 2.2. Also, the coordinates  $(v_l[m], m)$ , which represent the exact trace of the whistler with the particular dispersion constant of  $D = 4 \text{ s}^{1/2}$ , are denoted with red circles.



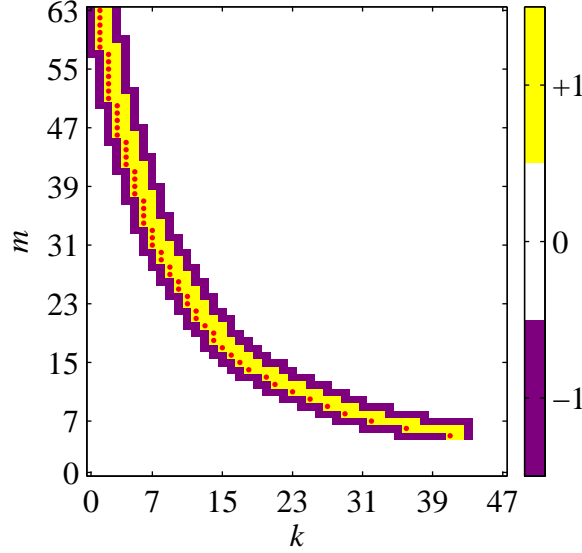


**Figure 2.2:** Whistler coefficient matrix for  $D = 4 \text{ s}^{1/2}$ . Yellow pixels are where the matrix is +1, and purple pixels show the negative values. Additionally, the red circles give the coordinates  $(v_l[m], m)$ , which are helpful for understanding (2.10).

### 2.2.3 Cross-Correlation with $0^+$ Whistler Shapes

For each normalized spectrogram  $q_n[m, k]$ ,  $n \geq A$  computed according to (2.6), we next measure how closely that spectrogram resembles a  $0^+$  whistler by taking the two-dimensional cross-correlation of it with a number of expected whistler shapes. The cross-correlation of each coefficient matrix  $c_l[m, k]$  is calculated for each normalized spectrogram  $q_n[m, k]$  as

$$r_l[n] = \sum_{m=0}^{\frac{N}{2}-1} \sum_{k=0}^{C-1} c_l[m, k] q_n[m, k] \quad (2.11)$$

Note that (2.11) represents  $S$  different vectors,  $r_0[n]$ ,  $r_1[n]$ ,  $\dots$ ,  $r_{S-1}[n]$ , again for  $n \geq A$ . Large values in  $r_l[n]$  mean that the spectrogram starting at the time given by (2.4) for the particular  $n$  index is highly correlated with the coefficient matrix  $c_l[m, k]$ , and so the larger  $r_l[n]$  is, the more likely the spectrogram contains a  $0^+$  whistler. As  $n$  is increased and the coefficient matrix moves over a  $0^+$  whistler with dispersion constant  $D$ , the values in at least one of the  $r_l[n]$  vectors will gradually increase to

a peak and then decrease to a nominal value around zero. The corresponding  $l$  from the dispersion constants  $D_l$  used to calculate the coefficient matrices that is closest to the actual dispersion constant  $D$  of the  $0^+$  whistler in the spectrogram denotes which of the  $r_l[n]$  vectors registers the largest peak.

As a demonstration of how the  $r_l[n]$  vectors can be used to detect a  $0^+$  whistler, Figure 2.3 shows the algorithm with  $N_\sigma$  set to 3 and the other parameters as specified in Table 2.1 (in Section 2.2.4) applied over some electric field data from the DEMETER satellite. The upper panel shows the spectrogram of the DEMETER data. In the middle panel, a representation of the normalized spectrogram where a pixel is colored if it ever exceeds the background for any of the normalized spectrograms of which it is a part is given. Finally, the bottom panel shows the  $r_l[n]$  vectors for five different dispersion constants  $D_l$ . Note that just as each  $0^+$  whistler occurs in the spectrogram, the green curve corresponding to a dispersion constant of  $D_l = 4 \text{ s}^{1/2}$ —the same as shown in Figure 2.1 for the prominent whistler in Figure 2.3—has a large peak, indicating the spectrogram immediately following is highly correlated with and the coefficient matrix calculated for  $D_l = 4 \text{ s}^{1/2}$  and therefore is likely a  $0^+$  whistler with that amount of dispersion.

The actual decision on whether or not a spectrogram is a  $0^+$  whistler is made after finding the maximum across the  $S$  vectors  $r_l[n]$  at each point  $n$ . That is, by finding

$$b[n] = \max_l(r_l[n]) \quad (2.12)$$

Then, a  $0^+$  whistler is identified at  $t_n$  given by (2.4) if  $b[n]$  is a local maximum and equals or exceeds some threshold  $T$ , a parameter of the algorithm. In the example of Figure 2.3, the  $r_l[n]$  vector for  $D_l = 4 \text{ s}^{1/2}$  has local maxima exceeding 30 preceding the strongest  $0^+$  whistlers, suggesting a threshold of  $T = 30$  is suitable for detecting  $0^+$  whistlers given the other parameters and ambient environment.

In order to minimize the possibility of false positives, another parameter that can be measured is the number of rows and columns that a given normalized spectrogram has values within the positive area of the coefficient matrix. Specifically, the

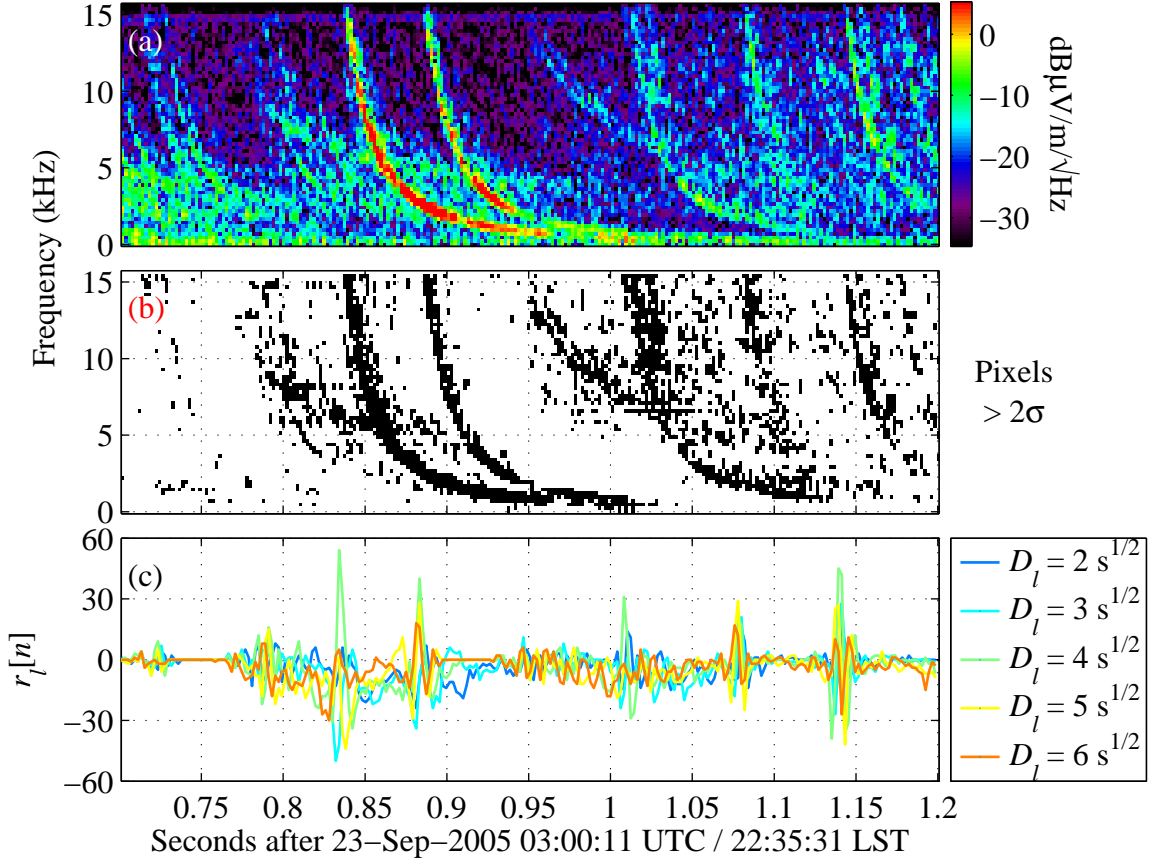


**Figure 2.3:** Result of applying algorithm over example DEMETER data. (a) Raw spectrogram magnitude. (b) Normalized spectrogram for  $N_\sigma = 2$ . (c) Algorithm result for various dispersion constants. Note that  $r_l[n]$  corresponding to  $D_l = 4 \text{ s}^{1/2}$  in panel (c) exceeds 30 for all the  $0^+$  whistlers visible the spectrogram in panel (a).

parameters to calculate can be written as

$$\rho_l[n] = \sum_{m=0}^{\frac{N}{2}-1} \Gamma \left( \sum_{k=0}^{C-1} c_l[m, k] q_n[m, k] \right) \quad (2.13a)$$

$$\gamma_l[n] = \sum_{k=0}^{C-1} \Gamma \left( \sum_{m=0}^{\frac{N}{2}-1} c_l[m, k] q_n[m, k] \right) \quad (2.13b)$$

where  $\Gamma(x)$  is a step function; that is,

$$\Gamma(x) = \begin{cases} 0, & x \leq 0 \\ 1, & x > 0 \end{cases}. \quad (2.14)$$

Essentially, the counts  $\rho_l[n]$  and  $\gamma_l[n]$  given by (2.13a) and (2.13b) respectively are not affected by how many rows or columns of the normalized spectrogram fall within the positive area of the coefficient matrix; just having at least one row or column is all that is required. These parameters are less sensitive to (and therefore will reject when thresholded) vertical and horizontal lines in the spectrograms.

### 2.2.4 Summary of Algorithm Parameters

Find in Table 2.1 a list of all of the algorithm parameters as well as the values that the ZPD FPGA onboard TARANIS uses for them. Specific details on the implementation of the algorithm on the ZPD FPGA presented in this chapter are provided in Appendix A, including for example how exactly the parameters  $N_\sigma$ ,  $D_l$ , and  $T$  can vary and how they are set using with a command to the satellite from the ground. In principle, the algorithm described here can be used to detect any type of whistler, not just  $0^+$  whistlers, or even any shape that follows (2.1), by adjusting the parameters in Table 2.1 appropriately.

## 2.3 Characterization of Algorithm

In general it is not obvious what the various parameters in Table 2.1 should be to result in an optimum algorithm. This problem is complicated by the fact that the parameters are not independent of each other: for example, a larger standard deviation threshold  $N_\sigma$  will result in fewer values of 1 in the normalized spectrogram of (2.6), which in turn will generally require a lower algorithm threshold  $T$  to detect a given  $0^+$  whistler. In order to determine what those parameters should be in the general case for the ZPD and the resulting algorithm efficacy, we applied the algorithm to data from the DEMETER satellite, which should be similar to that seen

**Table 2.1:** Algorithm Parameters and Their Values

Parameter	Description	ZPD Value
$W$	STFT Window Length	128
$O$	Overlap Length	64
$N$	Fourier Transform Length	128
$A$	Background Averaging Length	16
$N_\sigma$	Standard Deviation Threshold	varies
$C$	Normalized Spectrogram Window Length	48
$S$	Number of Whistler Shapes	8
$D_l$	Dispersion Constant for Whistler Shape $l$	varies
$T$	Threshold on Algorithm for Spectrogram to be Called a $0^+$ Whistler	varies
$R$	Threshold on Number of Rows for Spectrogram to be Called a $0^+$ Whistler	10
$Q$	Threshold on Number of Columns for Spectrogram to be Called a $0^+$ Whistler	7

on TARANIS, and compared the results with a hand labeling of  $0^+$  whistlers from the same data set.

### 2.3.1 $0^+$ Whistler Catalog

When the TARANIS satellite launches in 2018, it will be placed in a circular, sun-synchronous orbit of approximately 700 km altitude and passing over the Earth at around 01:30 and 13:30 local solar time (LST). It therefore will have a similar orbit to that of DEMETER. Recall that DEMETER had an electric field instrument that collected data at a rate of 40 kHz; during burst mode operations of the satellite, those sample values were transmitted to the ground in full [*Berthelier et al.*, 2006]. Therefore, burst mode data from DEMETER can be used to simulate what the ZPD on TARANIS can expect to encounter once the satellite is operational, and so we characterize the ZPD algorithm using data from DEMETER.

Characterization of the algorithm requires comparing it with a tried and true method of detecting  $0^+$  whistlers. As no other algorithm has currently been developed to identify  $0^+$  whistlers, we opt to hand label them in the DEMETER data. In

total, we analyze 40 daytime and 72 nighttime burst mode passes from DEMETER comprising 42m15s and 56m31s, respectively. In sum, we identified 8032  $0^+$  whistlers during the day and 58793  $0^+$  whistlers in the nighttime data.

### 2.3.2 Comparison with Algorithm

To find the algorithm-determined  $0^+$  whistlers, first we resample the 40 kHz DEMETER data to the sample frequency used in the TARANIS ZPD, which is done by first up-sampling the data to 2 MHz and then downsampling to 31.25 kHz using the CIC filter described in Section A.1.1. The result is a data stream close to what the ZPD will see. Ideally, the result would first be converted from  $\mu\text{V}/\text{m}$  to an applied voltage on the analog to digital converter (ADC) by inverting the transfer function that leads from the electric field antenna to the ADC, but we do not do this for two reasons: The transfer function is a complicated function of frequency, and computation of the normalized spectrogram makes the absolute value of the measurements irrelevant—only the relative measurement at successive times within the same frequency band matters.

Excluding variation in the algorithm threshold  $T$ , the number of possible configurations in which the ZPD can be operated total 2048: There are up to 16 different choices for the standard deviation threshold  $N_\sigma$ , 16 different sets of dispersion coefficients  $D_l$ , and 8 different science modes. To find the optimum choice generally, we compute the algorithm output  $b[n]$  as given by (2.12) for each 112 burst mode data sets and 1024 algorithm configurations. We test just 1024 configurations rather than 2048 because we opt not to toggle between thresholding on the rows and columns, reducing the number of science modes from 8 to 4.

Then we attempt to pair peaks (i.e., relative maxima) in the algorithm outputs  $b[n]$  with the hand selected  $0^+$  whistlers in that pass. Because the start time of a  $0^+$  whistler is not clearly defined, and  $b[n]$  might have a relatively small peak closer to a hand selected time than a relatively large one that is more likely attributable to that particular  $0^+$  whistler, this task is not as simple as assigning the closest peak in  $b[n]$  to the closest peak in the hand selected  $0^+$  whistlers. Instead, we do the pairing

by sorting the peaks in  $b[n]$  in descending order and then, starting with the largest one, seek a hand selected  $0^+$  whistler within  $\pm 20$  ms (approximately  $\pm 10$  spectrogram time indices). If there is one, that peak value gets paired with that hand selected  $0^+$  whistler, and that  $0^+$  whistler is removed from the remaining hand selected ones to be paired. If there isn't a hand selected  $0^+$  whistler within  $\pm 20$  ms, that peak value is considered "unpaired." Pairing the peaks in  $b[n]$  with the hand selected  $0^+$  whistlers in this way biases the paired peaks towards larger peak values because the pairings are done in descending order of  $b[n]$ , which is justified because our algorithm is designed with the idea that  $0^+$  whistlers will cause large values in  $b[n]$ . After the last hand selected  $0^+$  whistler is paired with a peak, the remaining peaks in  $b[n]$  are also classified unpaired. In our data, it never happens that the hand selected  $0^+$  whistlers do not get assigned a  $b[n]$  peak, as it is rare for  $b[n]$  to not have any peaks whatsoever, no matter how small, for long stretches.

Next, we histogram the peak values according to whether or not they are paired or unpaired with a hand selected  $0^+$  whistler by counting the number of peaks within each possible threshold value  $T$ . That is, we count the number of paired peaks between 0 and 4 and the number of unpaired peaks between 0 and 4, the number of paired peaks between 4 and 8 and the number of unpaired peaks between 4 and 8, and so on. Let  $N_p^s(T)$  and  $N_u^s(T)$  be the number of paired and unpaired peaks, respectively, for a given threshold  $T$  and given burst mode data set  $s$ . At this point, one could analyze each pass individually and come up with an optimum configuration for each data set, but our objective is to find a general optimum over a number of varied types of passes. Therefore, we sum these across the data sets  $s$  while still keeping night and day separate, resulting in four different vectors  $N_{p,u}^{n,d}(T)$ , where the superscript denotes either night (n) or day (d) and the subscript denotes either paired (p) or unpaired (u). Note, though, that each of these vectors is repeated over the 1024 different algorithm parameters that we varied.

Now we would like to determine the optimum threshold  $T$  to use for a given set of algorithm parameters. Setting the threshold too low will allow for many false positives, and setting the threshold too high will miss many actual whistlers. We set the threshold to the point where we can be at least 50% sure that the given

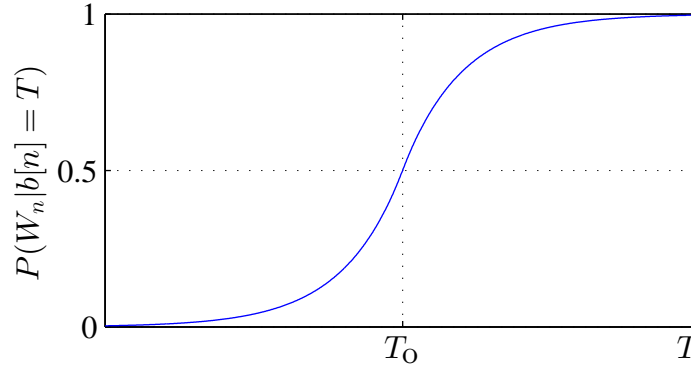


**Figure 2.4:** Possible form of the probability that a  $0^+$  whistler is at spectrogram  $n$  given that  $b[n] = T$  as a function of  $T$ .

algorithm output is due to the presence of a  $0^+$  whistler. If we let the event  $W_n$  mean that a  $0^+$  whistler is present at spectrogram  $n$ , then we seek the value  $T$  such that  $P(W_n | b[n] = T) \geq 0.5$ . That is, we seek the value  $T$  such that the probability of a  $0^+$  whistler being at spectrogram  $n$  given that the algorithm output  $b[n]$  is greater than or equal to the value  $T$  is greater than or equal to 0.5. Note in general we can estimate  $P(W_n | b[n] = T)$  as

$$P(W_n | b[n] = T) = \frac{N_p(T)}{N_p(T) + N_u(T)} \quad (2.15)$$

since  $N_p(T)$  gives the number of times  $b[n] = T$  corresponds to a  $0^+$  whistler and  $N_p(T) + N_u(T)$  gives the total number of times that  $b[n] = T$ . In general, if we plot (2.15) over  $T$ , we might expect a graph like Figure 2.4. The point  $T_o$ , which is the point where the probability crosses 0.5, is our optimum threshold. As  $T$  increases, the probability also increases, and for very large  $T$ , our confidence that the given algorithm output is the result of a  $0^+$  whistler approaches certainty.

Once an optimum threshold is found for each 1024 possible sets of algorithm parameters, what remains is finding the best set amongst those parameters. We simply select the one that maximizes the number of true detections (i.e., the true positives, or the number of  $0^+$  whistlers detected by the algorithm that were paired with a hand selected  $0^+$  whistler). The set of parameters that satisfy that condition



**Table 2.2:** Algorithm Parameters for Optimum Results

			Dispersion	Spectrogram	Negative
Time	$T$	$N_\sigma$	Constant Index	Magnitude	Coefficient
Night	32	1	1	Logarithmic	-1
Day	20	1.5	13	Logarithmic	-0.7578125

**Table 2.3:** Optimum Results for the Algorithm Parameters from Table 2.2

Time	Total Number of Hand Selected $0^+$ Whistlers	Number of True Detections	Detection Rate	Number of False Positives
Night	58793	27420	0.466	11549
Day	8032	5365	0.668	1472

for both night and day are shown in Table 2.2, and the results of that selection are given in Table 2.3. The detection rate, which might also be considered the detection efficiency, is simply the number of true detections divided by the total number of  $0^+$  whistlers identified by hand.

Using the parameters in Table 2.2, the algorithm successfully identifies almost half the  $0^+$  whistlers at night, while about 42% of the whistlers the algorithm identifies as  $0^+$  whistlers were not identified as such in the hand selections. For the daytime cases, the algorithm works even better: About 2/3 of the  $0^+$  whistlers are identified, and only about a quarter of the  $0^+$  whistlers the algorithm identified are false positives.

Other methods of selecting a set of algorithm parameters are possible of course. Ultimately the method chosen depends on the desired objectives. One might, for example, want to minimize the number of false positives and thus be almost absolutely certain that what the algorithm says is a  $0^+$  whistler is actually a  $0^+$  whistler.

## 2.4 Suggestions for Improvement

Unfortunately, limitations in the hardware force us to make certain design choices that often are not optimum. Ideally, all the parameters in Table 2.1 would be infinitely configurable from the ground. This would allow complete freedom to select any particular set of parameters depending on the expected conditions the satellite would

face. As it is, the ZPD is only allotted 3 command and control input bytes, and some of those bits are reserved for purpose besides selecting different configurations, which limited the number of choices.

We would suggest that the thresholding of the number of unique rows and columns with  $R$  and  $Q$  be configurable. That is, both  $R$  and  $Q$  should be allowed to vary rather than being fixed at 0 or 10 and 7, respectively. Those are arbitrary values that were never optimized against the hand-selected  $0^+$  whistler catalog we collected.

Additionally, the possible range of the algorithm output threshold  $T$  and standard deviation threshold  $N_\sigma$  are larger than is practically necessary. The algorithm in fact rarely computes a value greater than 80 even for very strong  $0^+$  whistlers, yet the input command allows for thresholds up to  $T = 252$ , which is in all likelihood impossible to reach. Similarly, the maximum possible  $N_\sigma$  parameter would reject the vast majority of pixels from the normalized pixels and thus render any  $0^+$  whistlers undetectable. Instead, we suggest allowing those parameters to float and then optimizing them against the hand selected  $0^+$  whistler catalog. If necessary, a reasonable range around the optimum could be set after the optimum is found (or the possibilities could be selected from different optimization objectives) rather than selecting arbitrary possible values and finding the optimum within that set.

## Chapter 3

# Comparison between the FWM and DEMETER

After *Starks et al.* [2008] found as much as a 20 dB overestimate by VLF propagation models coupled with the *Helliwell* [1965, Figure 3-35] sub-ionospheric absorption curves when compared to satellite measurements, all means of estimating trans-ionospheric VLF propagation were called into question. While the trans-ionospheric VLF propagation model of *Lehtinen and Inan* [2008, 2009], a frequency domain finite element electromagnetic full wave simulation (hereafter referred to as the full wave method (FWM)), was later validated to within 5 dB after comparison with measurements from the DEMETER satellite [*Cohen and Inan*, 2012; *Cohen et al.*, 2012], the quantification of the energy input by lightning-generated whistlers remained undetermined. In this chapter, we present a systematic comparison of model results was made with DEMETER satellite measurements.

### 3.1 Description of Data Sources and Models

The study utilizes data from the DEMETER satellite and National Lightning Detection Network. The simulation results come from the FWM developed in the Stanford VLF group.

### 3.1.1 DEMETER

The DEMETER (Detection of Electro-Magnetic Emissions Transmitted from Earthquake Regions) satellite was launched in June 2004 into Earth orbit at an altitude of 710 km (which was subsequently lowered to 660 km in December 2005) and remained in operation until the end of 2010. Having a circular, sun-synchronous orbit, DEMETER passed over a given part of the Earth close to 09:30 Local Solar Time (LST) in the morning and 21:30 LST at night, providing the opportunity to measure  $0^+$  whistler propagation through both daytime and nighttime ionospheric profiles. Among DEMETER’s many objectives was to measure the electromagnetic spectrum at the satellite altitude using two instruments carried for this purpose, both of which we utilize in this study: the Instrument Champ Electrique (ICE) to measure the electric field [Berthelier *et al.*, 2006] and Instrument Magnetometer Search-Coil (IMSC) for the magnetic field [Parrot *et al.*, 2006]. Both of these instruments had two primary modes of operation in the VLF band: a survey mode that continuously provided spectra every 2 seconds of a single field component up to 20 kHz with 20 Hz resolution and a burst mode that, while active only part of the time, provided full waveform data sampled at 40 kHz of a single field component. For this study, we exclusively use the burst mode data products with the field component in the plane of the orbit (specifically, DEMETER’s “E12” electric field sensor and “B2” magnetic field sensor), which are suitable for measuring the largely transverse components of upward propagating whistler waves.

Over the course of the DEMETER mission lifetime, burst mode data were primarily taken over regions with high seismic activity, which do not in general correlate with high thunderstorm activity. However, DEMETER did collect a large amount of burst mode data over the Great Plains in the United States during the summer of 2009, a time and region characterized by frequent thunderstorm activity. An example DEMETER burst mode pass over the United States during an active thunderstorm is shown in Figure 3.1.

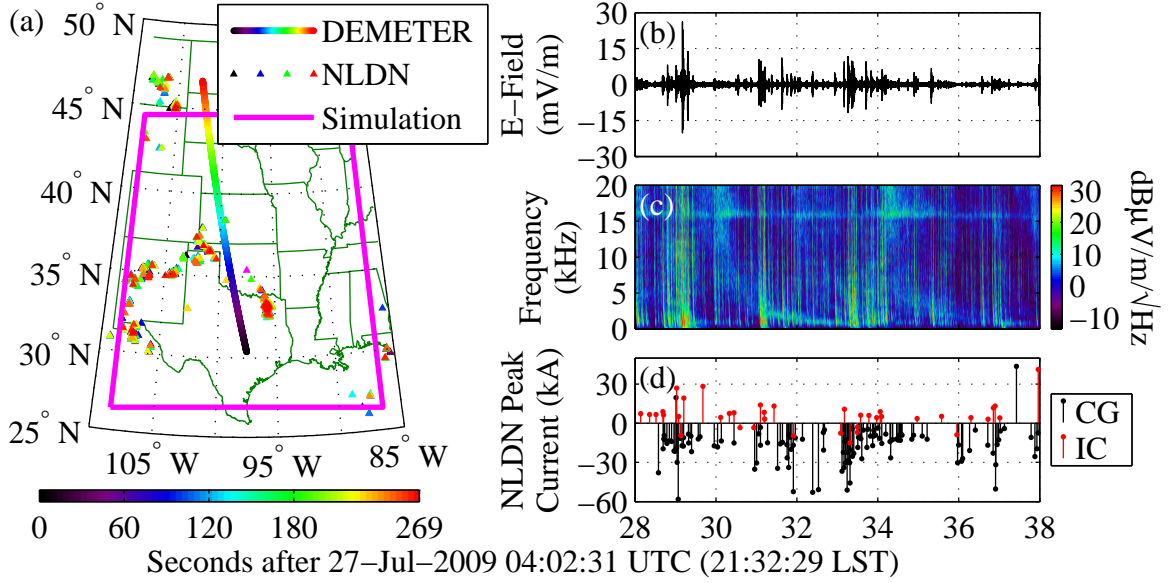


**Figure 3.1:** An example DEMETER burst mode pass with NLDN stroke data on 27-Jul-2009. (a) Trajectory of DEMETER for a single burst-mode pass along with lightning stroke locations reported by the NLDN. Additionally, the magenta box shows the extent of the FWM simulation space, and the magenta triangle in the middle of the box ( $35.4^\circ$  N,  $97.5^\circ$  W) shows the FWM source location and is also the point where the IRI and IGRF were acquired for input into the FWM. (b) Electric field burst mode waveform of a 10 second snapshot from this pass; (c) spectrogram of the same waveform; (d) peak current data as measured by the NLDN over the same 10 second snapshot.

### 3.1.2 National Lightning Detection Network (NLDN)

The whistlers observed on DEMETER are associated with lightning stroke measurements from the National Lightning Detection Network (NLDN), which uses remote measurements of sferics to geo-locate individual lightning return strokes [Cummins and Murphy, 2009]. Utilizing a combination of time of arrival and magnetic direction-finding techniques, the NLDN locates ground strokes with a median resolution of around 250 m. The NLDN also measures the peak current of each return stroke and classifies each detected event as either an in-cloud (IC) or cloud-to-ground (CG) stroke. While most lightning flashes are IC, the NLDN’s detection efficiency for IC flashes is less than 30%, but it detects up to 95% of CG flashes with peak

currents greater than 5 kA [Cummins and Murphy, 2009]. Figure 3.1 shows NLDN data coinciding with a DEMETER pass over an active thunderstorm during which the satellite collected burst mode data.

### 3.1.3 Full Wave Method

The FWM simulation model we use calculates the full electromagnetic fields from an arbitrary source configuration at a fixed frequency in a non-magnetic ( $\mu = \mu_0$ ) stratified medium with each layer in the vertical ( $z$ ) direction having an arbitrary complex permittivity tensor that is uniform along any horizontal ( $x, y$ ) plane. The full-wave field is split into two upward- and two downward-propagating modes that are transformed into adjacent layers in a recursive manner so as to avoid the numerical “swamping” that plagues many similar methods [Lehtinen and Inan, 2008, 2009]. The complex permittivity tensor in each layer is a function of the ambient magnetic field, electron density, and electron-neutral collision frequency, which serve as inputs to the FWM simulation. While the general complex permittivity tensor is also a function of electron-ion collisions, those were determined not to contribute significantly for the ion profiles used. Both the finite conductivity of the ground and the obliquely-directed magnetic field of the Earth are included in the model.

The 11<sup>th</sup> generation International Geomagnetic Reference Field (IGRF-11), a spherical harmonic expansion of the Earth’s magnetic field with coefficients calculated by a least squares estimate of various satellite measurements and magnetic surveys, is used as the ambient magnetic field input [Finlay et al., 2010]. When compared with satellite magnetometer measurements at altitudes between 200 km and 1000 km, the IGRF has been found to be accurate to within 1% almost 93% of the time and therefore is highly accurate even during geomagnetically active conditions [Matteo and Morton, 2011].

The electron density input comes from the International Reference Ionosphere (IRI) 2012, which utilizes a combination of ionosondes, incoherent scatter radars, rocket measurements, and satellites, to provide monthly averages of many ionospheric parameters [Bilitza et al., 2014]. The IRI has been validated by many independent

studies and is most accurate in the northern mid-latitudes due to the high ionosonde density in that region. Because the IRI only provides an electron density down to about 80 km at night, we extend the given electron density down to 60 km using an exponential decay as

$$N_e(h < 80 \text{ km}) = N_{e, 80 \text{ km}} e^{0.5(h-80 \text{ km})}. \quad (3.1)$$

Finally, we use the electron-neutral collision frequency given by equation (11) of *Swamy* [1992].

The FWM simulations were conducted in a  $2000 \text{ km} \times 2000 \text{ km} \times 665 \text{ km}$  space with 5 km spacing between horizontal grid points. Two separate FWM simulations were run using the IGRF and IRI at the location ( $35.4^\circ \text{ N}$ ,  $97.5^\circ \text{ W}$ ), denoted with a magenta triangle in Figure 3.1, for 13-Aug-2009 16:00:00 UTC and 13-Aug-2009 04:00:00 UTC, which broadly represent the average daytime and nighttime conditions over the region. A total of 212 (132) layers were used to represent the nighttime (daytime) ionosphere, and the ground was assumed to be flat with a conductivity of 10 mS/m. The lightning source is modeled as a unity amplitude electric current moment oriented vertically at the center of the simulation space on the ground (0, 0, 0). To capture the broadband nature of a lightning return stroke, we conducted FWM simulations for all frequencies up to  $f_{\text{max}} = 20 \text{ kHz}$  with a spacing of  $\Delta f = 40 \text{ Hz}$  (500 points) and then scaled the result by the *Bruce and Golde* [1941] model for the lightning return stroke current moment, which in this case is the product of the current and channel length. The return stroke current is

$$I(t) = I_0 \left( e^{-\alpha t} - e^{-\beta t} \right), \quad (3.2)$$

where  $I_0$  is the peak current amplitude and  $\alpha$  and  $\beta$  are parameters that Bruce and Golde found by observation to be about  $4.4 \times 10^4 \text{ s}^{-1}$  and  $4.6 \times 10^5 \text{ s}^{-1}$  respectively, and the return stroke channel length, which is the integral of the stroke velocity, is

$$\ell(t) = \frac{v_0}{\gamma} \left( 1 - e^{-\gamma t} \right), \quad (3.3)$$

where  $v_0 = 8 \times 10^7$  m/s and  $\gamma = 3 \times 10^4$  s<sup>-1</sup>, again determined empirically. We take the Fourier transform of the product of (3.2) and (3.3) to get the current moment as a function of frequency and then multiply the result by the propagation factor computed by the FWM simulation output to get the simulated field quantity to compare with the DEMETER data.

## 3.2 Whistler Comparison Procedure

For any individual pass of DEMETER over an active thunderstorm, the satellite will observe thousands of 0<sup>+</sup> whistlers, and so our first step in comparing the DEMETER data with the FWM simulations is to identify the occurrence times of each 0<sup>+</sup> whistler in the data. We employ an automated approach similar to the technique *Fiser et al.* [2010] used in identifying 0<sup>+</sup> whistlers on DEMETER over active thunderstorms in Europe. Once the 0<sup>+</sup> whistlers in a given pass of DEMETER have been identified, we then identify the parent lightning stroke of each 0<sup>+</sup> whistler using data from the NLDN in order to be able to compare the observed 0<sup>+</sup> whistlers with the predictions of the FWM simulation. Finally, the last step in making the comparison involves isolating the 0<sup>+</sup> whistlers from other 0<sup>+</sup> whistlers and the background noise and then computing their Fourier transforms.

### 3.2.1 Identification of 0<sup>+</sup> Whistlers

We find 0<sup>+</sup> whistlers in DEMETER data by utilizing the algorithm described in Chapter 2, although DEMETER's sampling frequency of 40 kHz is preserved rather than 31.25 kHz for the case of the ZPD. For a 128-point FFT and a 50% overlap, the resulting spectrograms have a frequency bin spacing of 312.5 Hz, and the bins are spaced 1.6 ms apart. We otherwise utilize the same parameters that the ZPD uses as given in Table 2.1. For the dispersion constants  $D_l$ , we use 16 different shapes with the  $D_l$  linearly spaced between 1 s<sup>1/2</sup> and 6 s<sup>1/2</sup>. Additionally, the standard deviation parameter is set to  $N_\sigma = 2$ , and the threshold for detection is  $T = 15$ . Since we only keep those whistlers that we can pair with NLDN lightning return



strokes (see Section 3.2.2), minimizing the number of false positives is not important, as they should be excluded anyway. Because the signal-to-noise ratio (and thus sensitivity) of DEMETER electric field instrument is higher than that of its magnetic field instrument, we generally detect more whistlers in the electric field than the magnetic field data.

### 3.2.2 Pairing $0^+$ Whistlers with NLDN Stroke Data

We require two pieces of information on the causative lightning return stroke for each of the  $0^+$  whistlers observed on DEMETER that we wish to compare with the FWM simulation results. The two pieces are the location of the source lightning and the lightning peak current amplitude. The former is necessary in order to know which coordinate in the FWM simulation should be used for comparison with DEMETER, and the latter sets the Bruce-Golde current magnitude  $I_0$ .

However, determining the parent strokes for each  $0^+$  whistler is complicated both by the unknown propagation time for the lightning stroke radiation to reach DEMETER and the offset between the NLDN and DEMETER clocks. To mitigate these issues, we utilize a method similar to that of *Chum et al. [2006]*: Let  $t_{Lj}$  be the time of the  $j$ th lightning stroke (measured by the NLDN),  $t_{Gj}$  be the propagation time of the sferic caused by the  $j$ th lightning stroke through the Earth-ionosphere waveguide (unknown),  $t_{Ij}$  be the propagation time of the whistler caused by the  $j$ th lightning stroke through the ionosphere (unknown), and  $t_{\Delta j}$  be the offset between the NLDN and DEMETER clocks at the time of the  $j$ th lightning stroke (unknown). One might then expect to measure a  $0^+$  whistler on DEMETER at a time of

$$t_{\text{exp}j} = t_{Lj} + t_{Gj} + t_{Ij}. \quad (3.4)$$

However, because the clocks on DEMETER and the NLDN are not synchronized, the actual time at which the  $0^+$  whistler will be observed is

$$t_{\text{act}j} = t_{Lj} + t_{Gj} + t_{Ij} + t_{\Delta j}. \quad (3.5)$$

Also, some lightning strokes may not produce a detectable  $0^+$  whistler observed on DEMETER, and some  $0^+$  whistlers observed on DEMETER may not have a parent lightning stroke measured by the NLDN since the network's detection efficiency is not perfect. Therefore, the number of lightning strokes may not necessarily be the same as the number of  $0^+$  whistlers. To reduce the number of time delay parameters, we assume all of the following:

1. The sferic propagates close to the magnetic footprint of DEMETER through the Earth-ionosphere waveguide before propagating through the ionosphere itself; hence  $t_{Gj}$  can be approximated as  $t_{Gj} \simeq d_j/v_G$ , where  $d_j$  is the distance between the lightning stroke and DEMETER's magnetic footprint at the time of the lightning stroke and  $v_G \approx c$  is the propagation velocity of a sferic through the Earth-ionosphere waveguide.
2.  $t_{Ij} \simeq t_I$  and  $t_{\Delta j} \simeq t_\Delta$  are approximately constant over a given pass.
3. Either most of the lightning strokes detected by the NLDN produce an observed  $0^+$  whistler or most of the observed  $0^+$  whistlers have a parent lightning stroke detected by the NLDN.

Given these assumptions, the most likely  $t_I + t_\Delta$  can be estimated by first calculating

$$t_{WL}|_{jk} = t_{Wk} - (t_{Lj} + t_{Gj}), \quad (3.6)$$

where  $t_{Wk}$  is the time of the  $k$ th  $0^+$  whistler observed on DEMETER, for all  $j$  lightning strokes and  $k$   $0^+$  whistlers. By assumption 3 above, the most common value for the difference in (3.6) corresponds to the most likely  $t_I + t_\Delta$ , and all lightning strokes and  $0^+$  whistlers that are separated by that time can be paired together.

We exclude any  $0^+$  whistler observed on DEMETER that we cannot pair with a parent lightning stroke, which can happen in two ways: Either the  $0^+$  whistler does not have a lightning stroke occurring in the vicinity of  $t_I + t_\Delta$  before it, or there is more than one  $0^+$  whistler following a single lightning stroke by  $t_I + t_\Delta$ , in which case the  $0^+$  whistler closest to the predicted occurrence time is chosen. For those  $0^+$  whistlers remaining, we determine how far east or west and north or south the

satellite was located relative to the lightning stroke paired with it and find the closest grid point in the FWM simulation to compare it with.

### 3.2.3 Isolating $0^+$ Whistlers in DEMETER Data

Because of the dispersion that a whistler undergoes, the signals of interest on DEMETER will extend over many milliseconds in time. This can be observed in Figure 3.2, which shows  $0^+$  whistlers measured by DEMETER. As panel (b) of the figure shows, it is even possible for another  $0^+$  whistler to appear on top of a  $0^+$  whistler occurring previously. Therefore, it is necessary to isolate the  $0^+$  whistlers from each other, which we do by reducing their extent in time using a technique known as “dechirping” [Jacobson *et al.*, 2011]. For each  $0^+$  whistler that we can pair with a source lightning return stroke, we take the 4096 time domain samples (about 102.4 ms) immediately after the beginning of the  $0^+$  whistler, prepend that signal with 4096 zeros, and send the resulting 8192 sample point signal through our dechirping procedure. The dispersion relation given by (2.1) equivalently means the phase delay of a whistler varies as  $-D\sqrt{f}$ . In other words, the ionosphere disperses (or chirps) the impulsive lightning signal by adjusting the phases of each frequency component by  $-D\sqrt{f}$ . To dechirp the whistler, we compute the Fourier transform of the 8192 point signal and multiply the Fourier components by the following scaling factor with the opposite phase delay:

$$\phi = e^{-i2\pi(-D\sqrt{f})} = e^{i2\pi D\sqrt{f}}. \quad (3.7)$$

Because the dispersion constant  $D$  is not precisely known, we apply this correction for a range of different dispersion constants. The dispersion constants range from  $2.5\text{ s}^{1/2}$  to  $4.5\text{ s}^{1/2}$  for nighttime whistlers and  $4\text{ s}^{1/2}$  to  $6\text{ s}^{1/2}$  for daytime whistlers, both in steps of  $0.001\text{ s}^{1/2}$ . Since ideally the signal condenses to a single impulse after being dechirped, we then select the one particular dispersion constant that results in the largest peak in the subsequent inverse Fourier transform. Panels (c) and (d) in Figure 3.2 demonstrate the result of dechirping the first whistler shown in panels (a) and (b) of the same figure. In this case, the dispersion constant  $D$  that resulted in

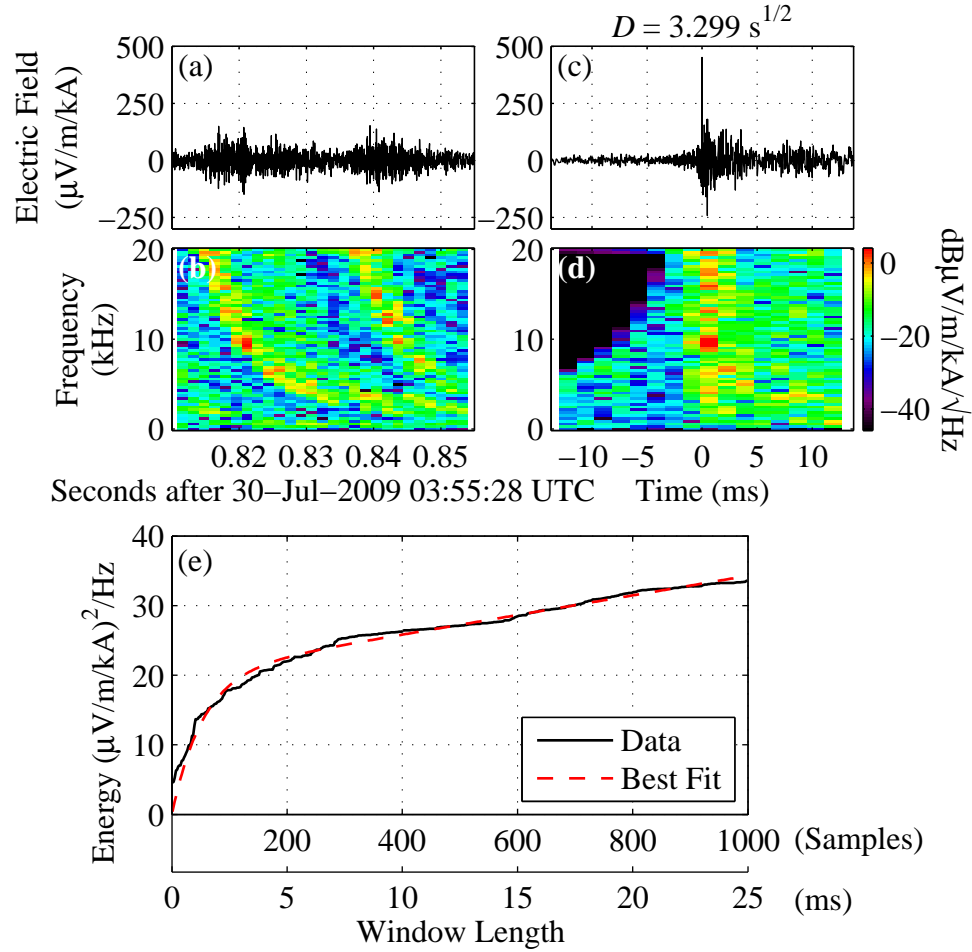


**Figure 3.2:** (a) Time domain waveform of two  $0^+$  whistlers observed on DEMETER normalized by the parent lightning peak current of the first  $0^+$  whistler. (b) Spectrogram of the time domain waveform in panel (a). (c) Result of dechirping the first  $0^+$  whistler observed in panel (a) using the best dispersion constant of  $D = 3.299 \text{ s}^{1/2}$ . (d) Spectrogram of the dechirped signal in panel (c). (e) Energy in the band between 2 kHz and 20 kHz in a window centered around the maximum of the dechirped signal in panel (c) as a function of the length of the window as well as a best fit line of the form given in (3.9) with  $\mathcal{E}_w = 20.2 (\mu\text{V/m/kA})^2/\text{Hz}$ ,  $\tau = 1.33 \text{ ms}$ , and  $\sigma^2 = 0.014 (\mu\text{V/m/kA})^2$ .

the largest peak in panel (c) happened to be  $D = 3.299 \text{ s}^{1/2}$ .

Note from the spectrogram of the dechirped signal shown in 3.2(d) that only one whistler is now present over a span of 10 ms. However, the dechirping procedure does

not typically succeed in condensing all of the whistler energy to one single point. Instead, the dechirped whistler can still have some nonzero extent in time, and so one must utilize a sufficiently large window that fully captures the entire whistler. At the same time, one cannot use an arbitrarily large window because a larger window brings in more background noise and may even run the risk of including another whistler, defeating the purpose of dechirping in the first place. Since the dechirp procedure should serve to condense most of the whistler energy at a single point (say  $t = 0$ ), we make the assumption that the instantaneous power of the dechirped signal comprises a sum of two terms: an exponentially decaying term representing the whistler and the background noise power, which we model as a zero-mean Gaussian random process with variance  $\sigma^2$ . Mathematically, this assumption can be written as

$$|x(t)|^2 = Ae^{-|t|/\tau} + P(t), \quad (3.8)$$

where  $A$  and  $\tau$  are constants representing the whistler strength and the characteristic extent of the dechirped whistler in time, respectively, and  $P(t)$  is the background noise power. The signal energy in a window of length  $T$  centered around  $t = 0$  is just the integral of (3.8), which is

$$\mathcal{E}(T) = \int_{-\frac{T}{2}}^{\frac{T}{2}} |x(t)|^2 dt = \mathcal{E}_w(1 - e^{-T/\tau}) + \sigma^2 T, \quad (3.9)$$

where we changed the whistler strength constant  $A$  into a new constant  $\mathcal{E}_w$  representing the total whistler energy and assumed that  $T$  is sufficiently large that the integral of  $P(t)$  reduces to the average power of the process:  $\sigma^2$ .

For each lightning/ $0^+$  whistler pair, we then compute the energy in progressively larger windows centered on the dechirp peak and expect that the resulting curve when plotted against the window length constitutes a reasonable fit to (3.9). From Parseval's theorem, we can compute the energy in a window either in the time domain or frequency domain. Doing the computation in the frequency domain, however, has the advantage of allowing us to calculate the energy within specific frequency bands by adjusting the limits of integration. In particular, because frequencies below about

2 kHz are below the Earth-ionosphere waveguide cutoff frequency and are thus heavily attenuated by propagation through the waveguide, we compute the signal energy between 2 kHz and 20 kHz. The energy computation for the whistler in Figure 3.2 is shown as the black line in panel (e). We use a non-linear least squares solver in MATLAB to determine the best fit of the data to an equation of the form of (3.9) for the three known parameters after normalizing it to a unitless form centered close to 1. In this example, the parameters were found to be  $\mathcal{E}_w = 20.2 (\mu\text{V}/\text{m}/\text{kA})^2/\text{Hz}$ ,  $\tau = 1.33 \text{ ms}$ , and  $\sigma^2 = 0.014 (\mu\text{V}/\text{m}/\text{kA})^2$ , and the curve which those parameters trace is shown as a dashed red line in panel (e).

### 3.3 Results

We applied the comparison procedure outlined in the previous section to a total of 21 different DEMETER burst mode passes over the center of the United States in the summer of 2009; seven of these occurred during the day while 14 occurred at night. The passes were selected due to their proximity to the center of the FWM simulation space coupled with the presence of a large number of lightning strokes nearby so that many lightning/ $0^+$  whistler pairings could be made. Table 3.1 shows the start times of each pass as well as the total number of pairings made for each field component. For any given pass, each field component typically has a different number of lightning/ $0^+$  whistler pairs because the number of whistlers detected by each field probe is generally different. Over the 21 DEMETER passes we selected, we collected over 20,000 lightning/ $0^+$  whistler pairs, each of which we further analyzed and compared with the results of the FWM simulation.

#### 3.3.1 Best Fit Estimated Signal to Noise Ratio

For each lightning/ $0^+$  whistler pair, we dechirped the whistlers, computed their energy for varying window lengths, and fit the curves to (3.9) as explained in Section 3.2.3. The signal-to-noise ratio (SNR) for each of the lightning/ $0^+$  whistler pairs can

**Table 3.1:** List of all DEMETER burst mode passes analyzed with the number of the NLDN lightning strokes, detected  $0^+$  whistlers, and lightning/ $0^+$  whistler pairs (both total and within the FWM simulation space) made for each pass.

Pass Start Time (UTC)	Duration (MM:SS)	NLDN Lightning Strokes	$0^+$ Whistlers Detected		Lightning/ $0^+$ Whistler Pairs		Pairs within FWM	
			E Field	B Field	E Field	B Field	E Field	B Field
Day	10-Aug-2009 16:26:01	1313	7363	1812	992	449	909	433
	17-Aug-2009 16:40:31	1210	8375	2320	980	588	942	572
	20-Aug-2009 16:32:31	2398	4634	1792	1534	640	1189	592
	26-Aug-2009 16:17:31	1661	7812	2239	1181	530	947	481
	21-Sep-2009 16:16:01	1158	5714	1298	909	448	865	437
	01-Oct-2009 16:22:01	1131	5473	1000	871	275	343	228
	08-Oct-2009 16:37:01	622	4297	1026	476	249	468	249
Night	21-Jul-2009 04:18:01	3213	10732	4426	2294	1515	1982	1372
	27-Jul-2009 04:02:31	4219	9186	4331	2458	1683	1388	1117
	30-Jul-2009 03:55:01	4590	10101	4529	2721	1740	1900	1542
	31-Jul-2009 04:25:01	2484	8055	1979	1702	751	927	552
	05-Aug-2009 03:39:31	4374	11108	5109	2911	1874	2202	1557
	06-Aug-2009 04:09:31	4144	10500	3631	2348	1321	774	610
	15-Aug-2009 03:46:01	2989	9891	4620	2080	1505	1432	1144
	16-Aug-2009 04:16:01	873	10519	3455	616	531	481	429
	18-Aug-2009 03:38:31	3089	10690	4060	2078	1328	1771	1206
	19-Aug-2009 04:08:31	2099	11684	5598	1591	1217	1158	983
	21-Aug-2009 03:30:31	3401	8817	3493	2046	1258	1288	926
	25-Aug-2009 03:53:01	875	9006	2726	674	426	415	339
	04-Sep-2009 04:00:01	1876	9265	2711	1348	881	632	542
	09-Oct-2009 03:35:01	1213	10220	3465	866	661	678	595

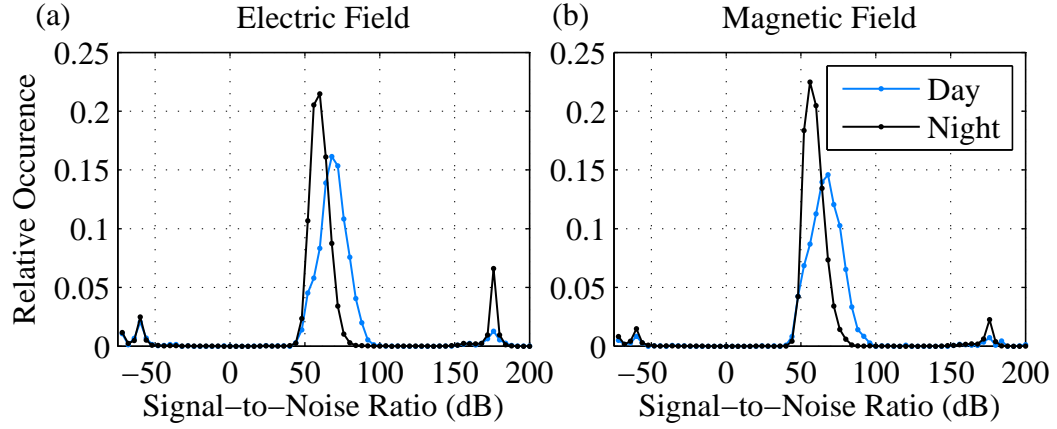


**Figure 3.3:** Histogram of the signal-to-noise ratios for all the lightning/ $0^+$  whistler pairs for both (a) the electric field and (b) the magnetic field.

be computed as

$$\text{SNR} = \frac{\mathcal{E}_w}{\sigma^2 \tau}. \quad (3.10)$$

A histogram of the SNR for all the lightning/ $0^+$  whistler pairs we identified is shown in Figure 3.3. The vast majority of the SNRs lie within a range between 30 dB and 130 dB, and SNRs outside that range are likely spurious cases where the signal and noise estimation via the best fit process failed. Therefore, any lightning/ $0^+$  whistler pair with an SNR less than 30 dB or greater than 130 dB was excluded in our subsequent analyses.

### 3.3.2 Spectrum of $0^+$ Whistlers over Horizontal Distance

In our first comparison of the DEMETER data with the results of the FWM simulation, we sort all the lightning/ $0^+$  whistler pairs by the horizontal distance from the source lightning return stroke to Earth’s magnetic field footprint from the DEMETER satellite to 110 km above the Earth (which is provided in the ephemeris data for the satellite) and then grouped all the pairs into 10 km bins. That is, all the pairs between 0 km and 10 km are grouped together into one bin, the pairs between 10 km and 20 km are grouped into another bin, and so on. We then compute the Fourier transform of the dechirped signals (panel (c) of Figure 3.2) using a fixed



window length of 200 samples (5 ms) for the nighttime pairs and 40 samples (1 ms) for the daytime pairs and found the median Fourier transform magnitude as a function of frequency over all the pairs in each bin. Recall that each lightning/ $0^+$  whistler pair has a FWM simulation output attached to it, so we compute the median amplitude of all those FWM outputs at the same time. In Figure 3.4, the top row shows the number of lightning/ $0^+$  whistler pairs composing each bin, the next two rows give the median electric field amplitude as measured by DEMETER and predicted in the FWM simulation, respectively, and the last two rows give the median magnetic field amplitude from DEMETER and the FWM simulation.

The most striking feature of Figure 3.4 are the lines emanating up in frequency as the horizontal distance increases, which are discussed in Section 3.4. Note that they are present both in the DEMETER measurements and FWM simulations for both the electric and magnetic fields. Overall, the DEMETER field amplitudes tend to be larger than the FWM, with two exceptions: the electric fields are larger in the FWM at high frequencies, and the nighttime magnetic field predicted by the FWM is larger than DEMETER for distances less than about 150 km. While there are not many lightning/ $0^+$  whistler pairs comprising the latter relationship, we show the former trend more explicitly in Figure 3.5. Each line represents a histogram for all the lightning/ $0^+$  whistler pairs (i.e., over all horizontal distances) of the ratio of the simulated  $0^+$  whistler energy to the measured  $0^+$  whistler energy for a particular range of frequencies. Notice for the electric field that the ratio increases as the frequency increases, but for the magnetic field, the ratio is roughly constant for all frequencies (except 0 kHz to 2 kHz).

### 3.3.3 Map of $0^+$ Whistler Energy

In Figure 3.6, we show the variation of the total  $0^+$  whistler energy over the two horizontal dimensions relative to the source lightning stroke at the origin. To construct the graph of the  $0^+$  whistler energy as measured by DEMETER (the top row of Figure 3.6), we first interpolate the DEMETER locations relative to the parent lightning stroke for all of the lightning/ $0^+$  whistler pairs to a uniform grid with

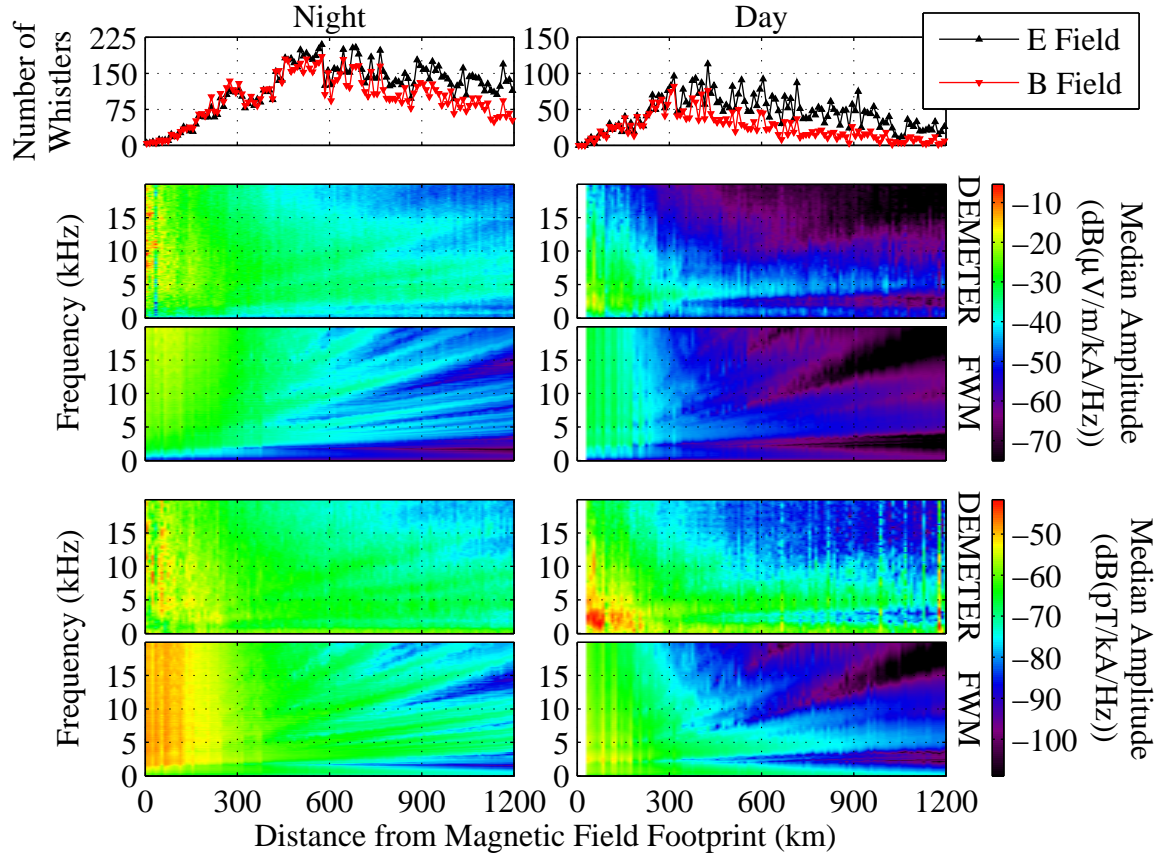


**Figure 3.4:** (top) Number of lightning/ $0^+$  whistler pairs made both at night (left) and during the day (right) as a function of horizontal distance partitioned into 10 km bins from the parent lightning stroke to the Earth’s magnetic field footprint of the DEMETER satellite. (middle) Median electric field  $0^+$  whistler amplitude over frequency and horizontal distance for each 10 km bin both at night (left) and during the day (right) as measured by DEMETER and predicted by the FWM simulation. (bottom) Same as (middle) for the magnetic field rather than the electric field.

spacing of 25 km in each direction. We then take the mean of the non-linear least squares fit parameter  $\mathcal{E}_w$  of all the whistlers at each grid point. Grid points having no lightning/ $0^+$  whistler pairs are shown in white. For the FWM simulation (middle row), we simply integrate the results between 2 kHz to 20 kHz (since the  $\mathcal{E}_w$  parameter is computed similarly) at every point. Finally, on the bottom row we show the ratio of the FWM simulation to the DEMETER measurement.

Both the DEMETER measurements and FWM simulations show a peak in  $0^+$

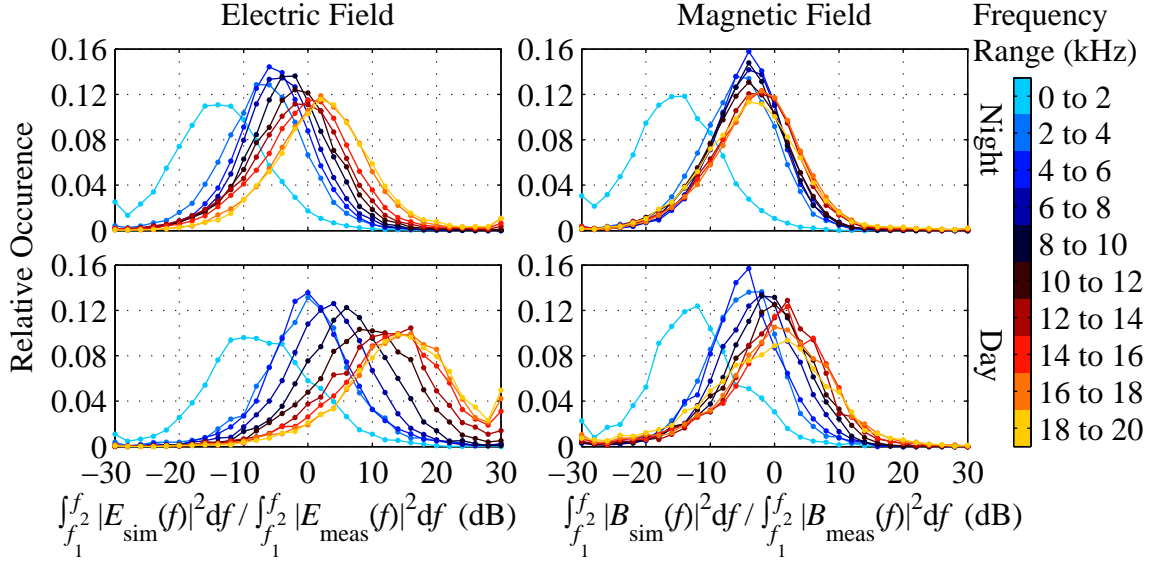


**Figure 3.5:** Histogram of the simulated to measured  $0^+$  whistler energy ratio in increasing frequency bands. The top panels show the histograms of the ratio for all the lightning/ $0^+$  whistler pairs seen at night, and the bottom panels have the ratios for the lightning/ $0^+$  whistler pairs seen in the daytime passes. Also, the left panels give the electric field energy ratio, while the right panels contain the magnetic field energy ratio.

whistler energy injection slightly south of the source lightning stroke, which is the location of the magnetic field footprint from the DEMETER satellite. Also, especially at night, the ratio of the simulated to measured data has the closest match near the peak in energy injection. As the distance from the peak increases, the ratio decreases, meaning that the DEMETER measurements become larger than the FWM simulation. This relationship is demonstrated more clearly in Figure 3.7, which gives histograms of the ratio of the energy in the simulated  $0^+$  whistlers to the energy measured by DEMETER for various distances from the source lightning stroke to the satellite magnetic footprint at 110 km. For both the electric and magnetic fields, the ratios are largest for the  $0^+$  whistlers with the smallest horizontal distance to their sources, and the ratios get progressively smaller with increasing distance. This trend is more continuous and pronounced across the nighttime ionosphere compared to the daytime, a result that could be due to the larger number of nighttime cases.

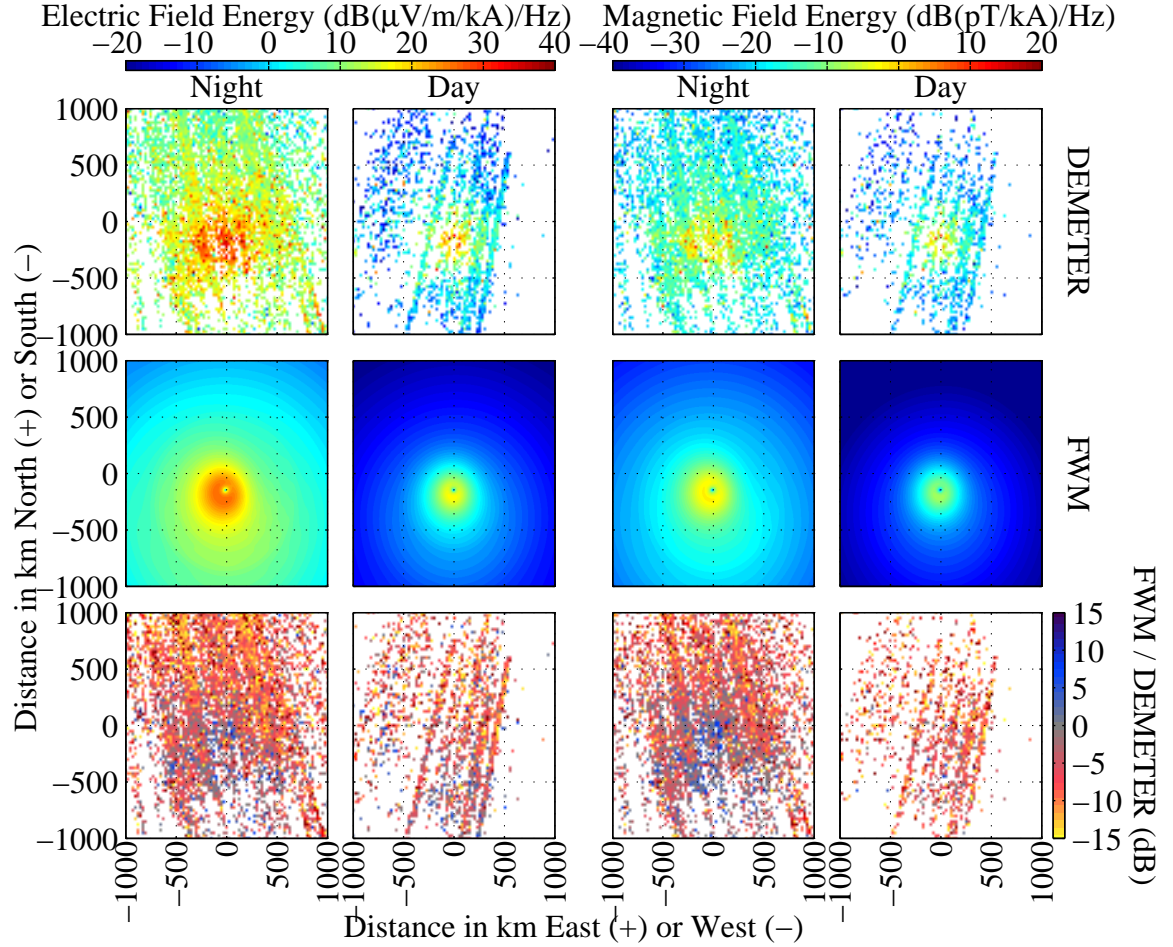


**Figure 3.6:**  $0^+$  whistler energy integrated from 2 kHz to 20 kHz (top) measured by the DEMETER satellite, (middle) computed by the FWM simulation, and (bottom) the ratio of the simulation to the measurement both for night and day and the electric and magnetic fields.

### 3.4 Discussion

When plotted over horizontal distance, the  $0^+$  whistlers observed on DEMETER show the same “V-shaped streaks” that *Parrot et al.* [2008] first reported in survey mode data from DEMETER when passing over thunderstorms. Those streaks were determined to be caused by a mapping to the satellite altitude of the modal interference pattern of sferic propagation through the Earth-ionosphere waveguide.

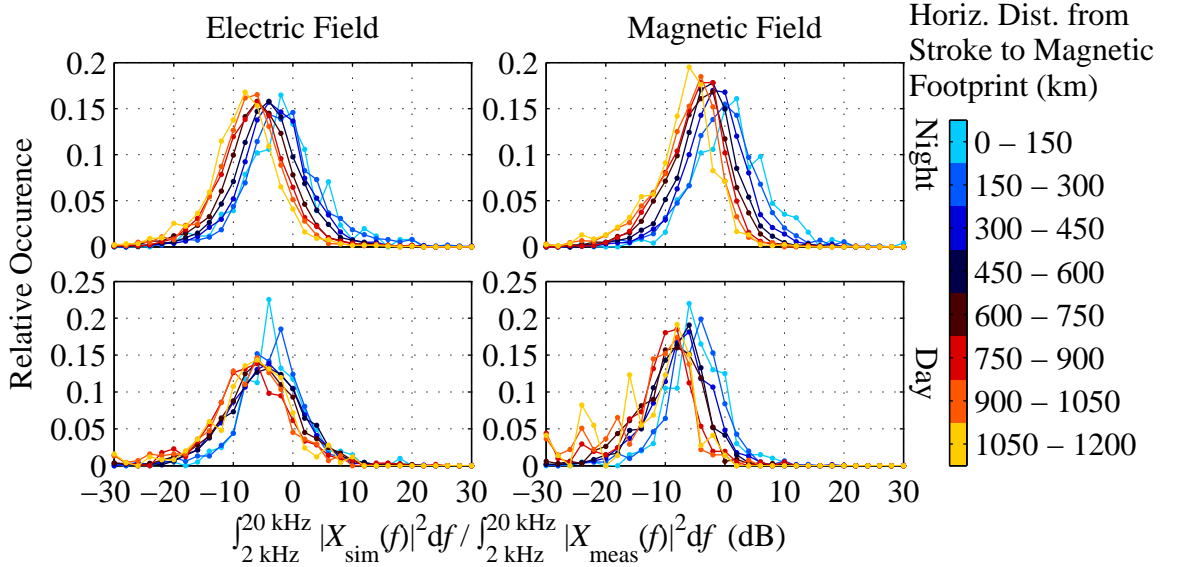


**Figure 3.7:** Histograms of the ratio of the simulated to measured  $0^+$  whistler energy separated into bins of increasing horizontal distance from the satellite magnetic footprint to the source lightning return stroke. The left panels show the electric field, and the right panels display the magnetic field. Additionally, the nighttime cases are given in the top panels, and the daytime cases appear below them.

The difference here is that the graphs displayed in the top panels of Figure 3.4 are composed of  $0^+$  whistlers from many varied DEMETER passes over a few months span, and interestingly, V-shaped streaks are nevertheless present. This indicates that the modal interference pattern is roughly constant across the entire late summer of 2009 which we analyzed. In addition, the structure of the V-shaped streaks in the DEMETER data match up well with the V-shaped streaks also present in the FWM simulation. The fact that the modal interference pattern is roughly constant from day-to-day indicates that the Earth-ionosphere waveguide is not too sensitively dependent on day-to-day variations of, for example,  $D$ -region electron density profiles.

However, the FWM simulation consistently underestimates the amount of  $0^+$  whistler energy measured by DEMETER both at night and in the daytime. Recall that *Starks et al.* [2008] found their simulations to overestimate the energy measured by satellites, which is the opposite of our finding. There are a few possible explanations for why the FWM might predict smaller field strengths than seen on DEMETER.

First of all, because the FWM is only simulating a single lightning stroke, any other noise present in the DEMETER data would cause an underestimate by the FWM, a problem we attempted to minimize by measuring the whistler energy as a parameter in fitting a curve to (3.9) as described in Section 3.2.3. Another possibility is that the FWM is underestimating the amount of energy that escapes the Earth-ionosphere waveguide, but such a case is unlikely in part because the V-shaped streak pattern seen in the FWM simulation so closely matches what is seen on DEMETER. To be sure this is not the case, though, we compared the FWM simulation results on the ground to a sferic waveform bank and found agreement to within about 2 dB, which is within the measurement uncertainty of the sferic waveform bank.

What remains, then, is that the FWM predicts more loss in the transmission through the ionosphere than the NLDN and DEMETER measurements suggest. Also, the FWM shows a larger underestimate of the field strengths (i.e., predicts more loss than measured) as the distance from the satellite’s magnetic footprint is increased. A distance dependent discrepancy could be caused by the FWM not accounting for a curved Earth: Sferics propagating through a curved Earth-ionosphere waveguide are in reality incident on the ionosphere with a less grazing angle, and hence more energy would escape the waveguide. However, not accounting for the Earth’s curvature cannot fully explain the discrepancy because our simulations only show up to 2 dB more energy in the waveguide than measured. It is well known that lightning strokes occurring in the lower atmosphere can cause perturbations in the lower ionosphere up to 100 km, evidenced both by “early/fast” events in Earth-ionosphere propagating VLF transmitter signals [e.g., *Armstrong, 1983; Inan et al., 1988, 1991*] and transient luminous events observed at high altitudes [e.g., *Lyons, 1994; Sentman et al., 1995; Fukunishi et al., 1996*]. Because those perturbations are localized to within at most a few hundred kilometers from the lightning stroke, the ionosphere could be significantly different in lateral extent from the IRI baseline than that assumed by the FWM over the entire simulation space, and therefore the predicted signal would be different relative to the DEMETER measurement over horizontal distance. The simulated field strengths are particularly sensitive to changes in the daytime electron density.

Finally, the FWM predicts relatively larger electric field strengths for increasing



frequency, but the same trend is not present in the magnetic field. That difference suggests that the FWM predicts a different ratio between the electric and magnetic field strengths as a function of frequency than what is measured by DEMETER. If we assume that the horizontal electric and magnetic fields measured by DEMETER comprise the entire wave fields (i.e., that the waves have minimal vertical components), and that the wave electric field is entirely transverse to the wave vector, we can approximate the refractive index  $n$  as

$$n = \frac{cB}{E}. \quad (3.11)$$

Therefore, DEMETER measurements of a different field ratio than predicted by the FWM suggests that DEMETER measures a different refractive index. Recall that the refractive index of a wave propagating in a plasma can be computed from the Appleton-Hartree equation (1.4). Invoking the QL approximation and ignoring collisions (so that  $Z = 0$ ), the refractive index of the RHCP whistler mode can be found from (1.7) as

$$n^2 = 1 - \frac{\frac{\omega_{pe}^2}{\omega^2}}{1 - \frac{\omega_{ce}}{\omega}}, \quad (3.12)$$

where  $\omega$  is the wave radian frequency,  $\omega_{pe}$  is the electron plasma frequency, and  $\omega_{ce}$  is the electron cyclotron frequency. We compare the refractive index as predicted from (3.12) using the electron density and magnetic field as given by the IRI and IGRF with the mean and median of the refractive indices of the all the whistlers observed on DEMETER using (3.11) in Figure 3.8. Only those  $0^+$  whistlers that were detected in both the electric and magnetic fields are included here. Additionally, the mean refractive index of the paired FWM simulation results computed using (3.11) is also plotted; the median is not significantly different for the FWM.

The whistler mode refractive index follows the FWM curve well both at night and during the day. However, the curves for DEMETER show a significant divergence from the whistler mode prediction, especially for higher frequencies where the  $1/f$  trend that (3.12) would suggest is not evident. Much of that discrepancy during the

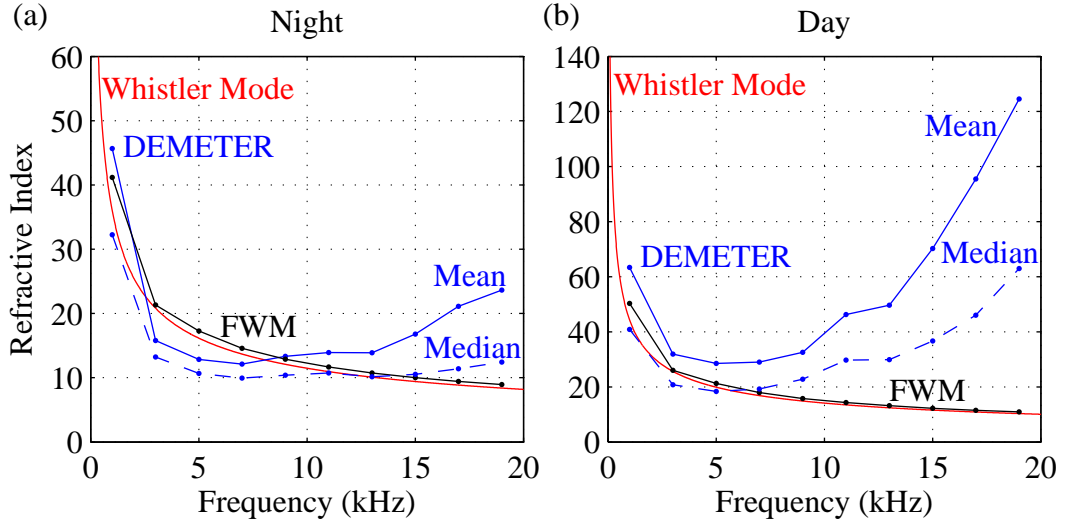


**Figure 3.8:** Refractive index for both the (a) nighttime and (b) daytime ionospheres predicted by the Appleton-Hartree equation whistler mode (red) compared with the mean and median refractive index measured by DEMETER (solid blue and dashed blue, respectively) and the mean refractive index computed from the FWM simulation results (black).

day is likely due to the fact that the daytime ionosphere blocks frequencies above about 10 kHz from propagating up to the satellite’s altitude from the ground, and hence the signal to noise ratio for those frequencies is likely too small. This behavior is especially evident after viewing  $0^+$  whistlers in DEMETER data during the day. However, the trend, albeit somewhat weaker, is also present at night where the signal to noise ratio is generally quite good.

Two possibilities remain to explain this discrepancy: the DEMETER data could be miscalibrated, or DEMETER measures something more than whistler-mode waves, although it is not clear what that might be. Conversion to quasi-electrostatic-mode waves is likely not responsible for this trend for two reasons:

1. When a whistler is converted into quasi-electrostatic-mode waves, the whistler-mode energy is reduced, but we see more energy on DEMETER than in the FWM, where the horizontal stratification does not allow for conversion to quasi-electrostatic mode waves.



2. Quasi-electrostatic-mode waves are so named because they have large electric field components relative to their magnetic field components and can only propagate for frequencies larger than the lower hybrid resonance frequency. Therefore, we would expect the DEMETER-measured electric field to be larger than the whistler mode for high enough frequencies, but in fact the electric field on DEMETER at those frequencies is on average smaller.

### 3.5 Conclusions

We compared results from two FWM simulations representing a nighttime and daytime ionosphere with field measurements from the DEMETER satellite for 21 different passes over the central United States in the summer of 2009. Our FWM simulations predict smaller field amplitudes in the ionosphere than measured by the DEMETER satellite, the opposite of what *Starks et al. [2008]* found when comparing their models of anthropogenic VLF transmitters to satellite measurements, including DEMETER. The discrepancy between the FWM and DEMETER is smallest for the magnetic field at night—approximately just 3 dB—while during the day the underestimate by the FWM is closer to 6 dB. The electric field, on the other hand, on average shows an underestimate by the FWM of about 5 dB at night and over 6 dB during the day. Two trends are noteworthy: The FWM predicts relatively smaller field amplitudes at larger distances between the source lightning stroke and the satellite’s magnetic footprint. Also, the electric field predicted by the FWM is relatively larger for increasing frequencies, while the magnetic field predicted is approximately equal to that measured for all frequencies.

After ruling out the possibility that the FWM predicts that less energy escapes the Earth-ionosphere waveguide than DEMETER indicates and that a significant amount of background noise is inflating the DEMETER measurements, we have concluded that the FWM overestimates the amount of loss in the trans-ionospheric propagation of  $0^+$  whistlers. Our analysis here thus implies the FWM simulations predict less VLF wave energy from lightning entering the magnetosphere than indicated by measurements from DEMETER and the NLDN. The decrease in the simulated field

strengths relative to DEMETER with increasing horizontal distance from the lightning stroke could be due to our model not accounting for the curved Earth and the lightning strokes causing localized perturbations in the ionosphere. Finally, we also noted that the refractive index as indicated by the DEMETER measurements shows a significant divergence from that predicted both by the FWM and the whistler mode of the Appleton-Hartree equation, which could either be due to a miscalibration of the DEMETER data or an indication that something other than whistler-mode waves are being measured.

## Chapter 4

# Calculation of the Global Upgoing Lightning Power

Since we previously showed the efficacy of the FWM in estimating the wave power in the ionosphere due to lightning, we now apply the technique to lightning all over the world to derive an estimate of the total wave power propagating up and out of the ionosphere and into the plasmasphere from tropospheric lightning. Such an estimate involves taking data from a number of different FWM simulations representing different conditions on Earth to derive a global map of wave power injection from anywhere on the ground. The result is then scaled by the amount of lightning that actually occurs at each of those points. After a detailed description of our method of estimation, results are followed by a discussion.

### 4.1 Methodology

First and foremost, the amount of lightning energy in space is highly dependent on the amount of lightning that happens near the ground. Therefore, information on where on the ground the lightning occurs and the peak current of the lightning, which we determine using the Global Lightning Dataset, is needed to determine the lightning energy in space. We then calculate for a given peak current density at each point on Earth the upgoing power flux (in  $\text{W/m}^2$ ) using a FWM simulation for the

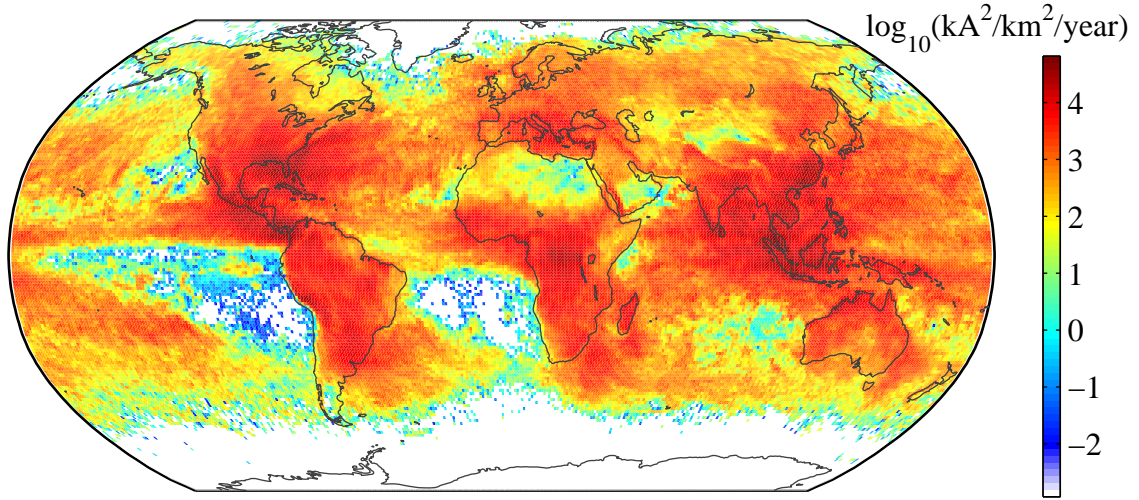


**Figure 4.1:** Lightning return stroke peak current density as provided by GLD360 over the entire year of 2014 across the globe.

magnetic field and ionospheric conditions at that point. By combining the power flux at all points on the globe, a global lightning energy estimate injected into the plasmasphere can then be calculated.

#### 4.1.1 Global Lightning Dataset (GLD360)

We obtain data on global lightning return strokes from the Vaisala Global Lightning Dataset (GLD360) system. Composed of a series of VLF receivers across the globe, the GLD360 triangulates lightning return strokes by analyzing the sferic waveforms from many different receivers [Said *et al.*, 2010]. Like the NLDN, the GLD360 utilizes both direction finding and time of arrival techniques to determine the return stroke location. As opposed to satellite systems such as the optical transient detector, which only provide a sampling of lightning occurrence information [Christian *et al.*, 2003], a particular advantage of the GLD360 network is truly continuous global coverage and recording of both the location and lightning return stroke peak current. The operators of the network claim that the system currently has a detection efficiency of at least 70% in the northern hemisphere and a median location accuracy of 2 km to 5 km.

The GLD360 data provides a source input for our simulation results. Specifically, we generate a map that provides the lightning return stroke peak current density across the world by summing the squared peak current of each GLD360-provided return stroke occurring within half a degree in latitude and longitude at every coordinate on Earth (thereby providing the return stroke peak current density on a  $1^\circ \times 1^\circ$  grid) and then dividing by the area of that region and one year in time. The result is shown in Figure 4.1. While Figure 4.1 shows the results for the entire year, it should be noted that lightning in general is highly seasonal, and so we actually generate maps for each month, which are not shown here. Also, because the propagation through the ionosphere depends on the time of day, we also find the return stroke peak current density for each hour of the day.

As expected, regions of high lightning activity, such as the southeast United States and southeast Asia, are strongly represented in the stroke peak current density map. Interestingly, Sub-Saharan Africa, which in the past has been shown to have the most frequent lightning occurrence rate [*Christian et al., 2003*], does not have the largest return stroke current density in the world (a distinction instead belonging to the southeast United States), which, if not caused by a network bias, could indicate that peak current magnitudes in Africa are lower than in other parts of the world. Also, the oceans are more highly represented in this graph than in lightning occurrence rate data. The GLD360 tends to report larger peak currents over the ocean than over land [*Said et al., 2013*], and investigations into why that is the case, specifically whether the larger peak currents over the oceans are due to a network effect or the fact that lightning over the ocean actually has larger peak currents generally, are ongoing [see, e.g., *Zoghzoghy et al., 2015*].

### 4.1.2 Simulation Size

Ideally, of course, we would run a single simulation representing the entire Earth and be done. In practice, the FWM cannot be used over an entirely global simulation space because it cannot account for a laterally varying ionosphere or even a dipolar magnetic field. So instead, we conduct a number of simulations at a much smaller

scale and then essentially stitch the results from each of the smaller simulations together. However, on the face of it, it is not immediately clear how large or small those simulations need to be to fully capture the global distribution. We therefore must make some assumptions and determine how they will affect our final results.

The first thing to determine is the layer heights to use. More layers would result in a more accurate simulation at the expense of taking longer to complete. We opted to use 0.5 km layer heights up to an altitude of 110 km and 2.5 km heights above that altitude as a reasonable trade-off between accuracy and computation time.

Next, we calculate the total upgoing power at various altitudes to determine the maximum simulation height needed. Specifically, we conduct simulations of a single lightning return stroke out to a lateral distance of  $\pm 2000$  km using a generic daytime ionosphere and a magnetic field inclined  $60^\circ$  from the horizontal ground for frequencies 200 Hz, 2 kHz, and 20 kHz and saved the total fields at various altitudes between 65 km to 300 km. The total upgoing power flux can then be computed as the Poynting flux ( $\vec{S} = \vec{E} \times \vec{H}$ ), which is shown in Figure 4.2 for the three frequencies at the various altitudes. Note that above an altitude of 150 km, the upgoing power flux is relatively unchanged, which indicates that both most of the coupling of wave energy from the Earth-ionosphere waveguide up through the ionosphere and most of the losses due to collisions with neutral constituents occur below that altitude. Hence, running simulations up to just 150 km satisfies our goal of computing most of the total upgoing power flux due to a single lightning return stroke.

The other important consideration after the simulation height is the lateral extent the simulations should cover to fully account for the upgoing power. In principle,  $0^+$  whistler energy could emerge out upward through the ionosphere at lateral distances of thousands of kilometers away from the parent lightning source owing to the efficiency with which sferics propagate through the Earth-ionosphere waveguide. In practice, however,  $0^+$  whistlers have only been observed on satellites out to around 1500 km away from their parent lightning strokes (see, e.g., Chapter 3 and [Chum *et al.*, 2006]). Beyond that, any whistlers that may be present are swamped by the noise and therefore do not contribute appreciably to the total injected power. Because simulation runs take exponentially longer to finish as the lateral distance increases,

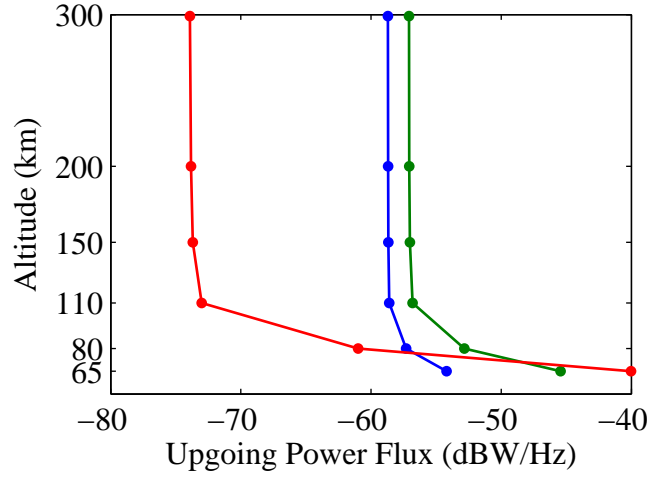


**Figure 4.2:** Upgoing power flux at various altitudes according to FWM simulations of a single lightning return stroke at three different frequencies.

we seek to reduce the lateral extent of the whistlers as much as possible without sacrificing the integrity of our results. Therefore, in addition to the simulations already conducted above, we run simulations at 5 kHz, 10 kHz, and 15 kHz and computed the total upgoing power flux at an altitude of 150 km for each of the simulations. The result for 5 kHz is shown in Figure 4.3(a).

Note that most of the upgoing power is concentrated near the origin where the lightning return stroke source is located. So we then compute the upgoing power through smaller subsets of the entire simulation, with those subsets being larger and larger squares centered at the origin and representing simulations with smaller lateral extents than the full  $\pm 2000$  km simulation. A plot of the power going through those smaller squares normalized by the total power passing through the entire  $\pm 2000$  km simulation is shown in Figure 4.3(b). Note that more than 80% of the power goes through a square within  $\pm 500$  km of the origin. Accordingly, we conducted our simulations out to that distance. Practically, longer distances not only take longer to run but also become unrepresentative of the actual real world conditions since the curvature of the Earth and lateral changes in the ionosphere and Earth's magnetic field, none of which the FWM model accounts for, begin to have an effect. Because a degree of latitude is about 110 km (and a degree of longitude is about the same at

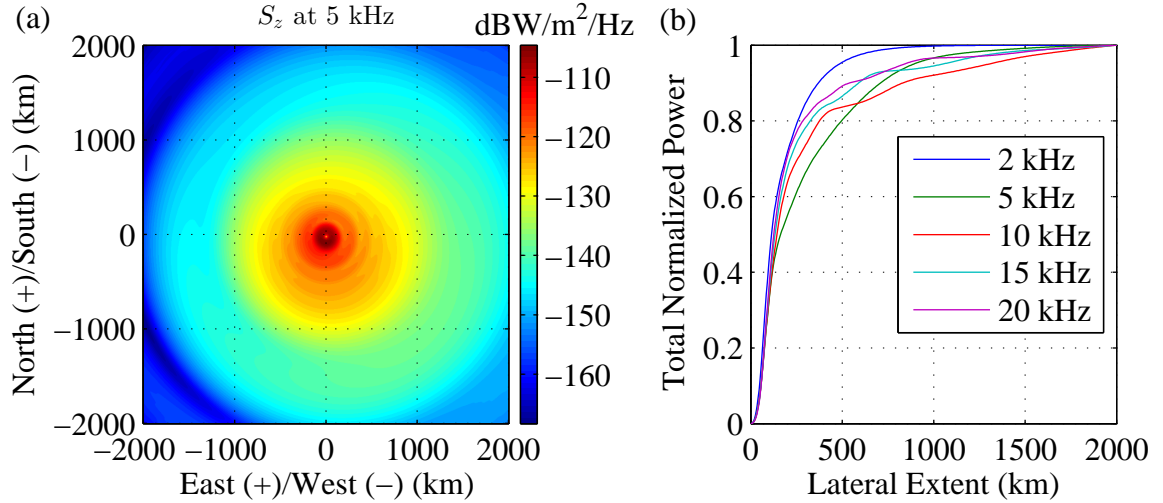


**Figure 4.3:** (a) Upgoing power flux at an altitude of 150 km for the FWM run at 5 kHz. (b) Total upgoing power flux passing through the given lateral extent normalized by the total upgoing power flux through the entire simulation at the given frequencies.

the equator, getting progressively smaller with increasing latitude), each simulation thus accounts for the power due to a lightning stroke out to about  $\pm 4.5^\circ$  in latitude and longitude.

Up to a certain point, the nature of the way that the FWM calculations are carried out means that the horizontal grid spacing does not appreciably affect the total simulation run time. That is, there is little difference in computation time between using a 1 km grid versus a 10 km grid, unlike the case for finite-difference time-domain methods. This result essentially stems from the fact that the FWM makes its calculations in the wave-vector space and recovers the fields as a function of position using a (spatial) inverse Fourier transform. Compared to the computation of the fields in the wave-vector space, that inverse Fourier transform is relatively quickly and efficiently computed in MATLAB using matrix multiplication. Ultimately, the limiting factor in this case is the memory required to store the desired grid in a matrix (so eventually the grid spacing can be so small that limits on the available memory would bog down the calculation). We opt to save a 5 km grid, which is much smaller than a degree of latitude, our ultimate goal for spatial resolution.



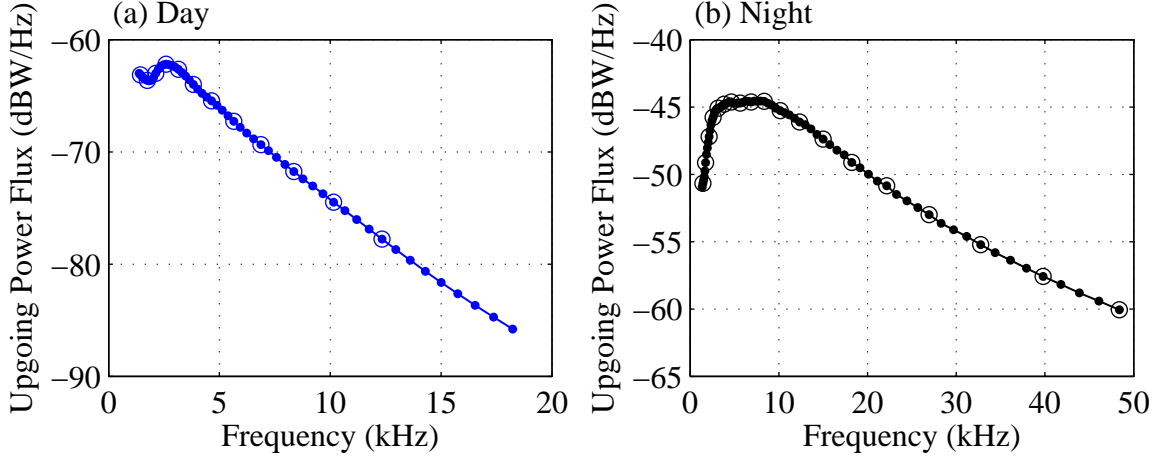


**Figure 4.4:** The total integrated upgoing power flux at an altitude of 150 km out to  $\pm 500$  km for a FWM simulation having a  $45^\circ$ -tilted magnetic field and a typical (a) daytime and (b) nighttime ionosphere as a function of frequency. The solid circles are the discrete frequencies run, and the open circles denote the frequencies that are run in the final global simulations.

### 4.1.3 Frequency Bandwidth

The next choice to be determined was the frequencies necessary to reasonably compute the total lightning power. Ideally we would conduct simulations from DC to infinite frequency, but of course that is not practical. To determine which frequencies contribute most to the lightning power flux, we conduct simulations for a typical daytime and nighttime ionosphere and over the same numerical space as decided in the previous section (out to  $\pm 500$  km and up to 150 km altitude) and a magnetic field inclined  $45^\circ$  from the ground. The frequencies at which the simulations are run ranged from

$$f = (15 \text{ kHz}) \times 1.05^n, \quad (4.1)$$

where  $n = -49, -48, \dots, 4$  for the daytime ionosphere and  $n = -49, -48, \dots, 24$  for the nighttime ionosphere. The total integrated upgoing power flux is graphed in Figure 4.4 for both simulations, and the discrete frequencies run as given by (4.1) are denoted with solid circles.

The upgoing power flux in the daytime simulations begins rolling off as early as

about 2 kHz while the power flux in the nighttime simulation does not start its roll off until about 10 kHz. Also, the upgoing power flux in the daytime simulations rolls off more quickly than the power flux in the nighttime simulation. Therefore, we conclude that more and higher frequencies would be required for simulations with a nighttime ionosphere than those with daytime ionospheres. In particular, we opt to conduct daytime simulations for frequencies given by (4.1) with  $n = -48, -44, \dots, -4$ , while  $n = -48, -44, \dots, 24$  for the nighttime simulations. Those frequencies are labeled with open circles in Figure 4.4.

#### 4.1.4 Orientation of Earth's Magnetic Field

The orientation of Earth's magnetic field on the ground can be described with two angles: The first, known as the inclination  $I$ , is the angle between the ground and the magnetic field vector. This angle is illustrated in Figure 4.5 along with the variation of the inclination across the world as given by the IGRF. An inclination of  $0^\circ$  represents a horizontal magnetic field, and positive inclinations indicate a magnetic field pointing out of the ground while negative inclinations indicate a magnetic field pointing into the ground. An inclination of exactly  $\pm 90^\circ$  is an entirely vertical magnetic field. Because the Earth's magnetic field is approximately a dipole, the inclination on Earth roughly varies with latitude: That is, latitudes near the equator have approximately a horizontal inclination, and latitudes near the poles have an almost vertically directed magnetic field, with intermediate values in between. The line where the inclination is exactly  $0^\circ$  is known as the magnetic equator. Note that while the inclination in general can be positive or negative, the amount of electromagnetic wave energy propagating through a plasma is independent of the sense of direction of the magnetic field line, and hence only positive inclination simulations are necessary. The negative inclinations can be represented by flipping the simulation results along the east/west axis (i.e., so north becomes south and south becomes north). We conduct simulations for inclinations between  $0^\circ$  and  $88^\circ$  in  $4^\circ$  increments.

The other angle that describes the Earth's magnetic field on the ground is known as the declination. It is the angle between true geographic north and where the

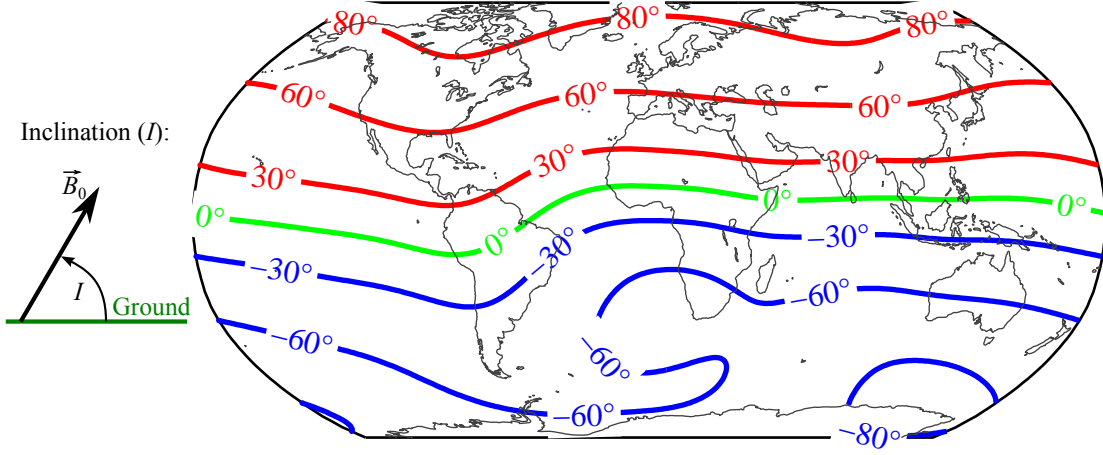


**Figure 4.5:** Earth’s magnetic field inclination given by the IGRF.

magnetic field is directed. A declination of  $0^\circ$  means that the Earth’s magnetic field points exactly towards the Earth’s north pole at that point (ideal for navigation incidentally). In practice, variation in the declination angle can be captured by conducting simulations for just one declination (say  $0^\circ$  for convenience) and then a coordinate rotation of the results by the corresponding declination at that point. A diagram of what is meant by the declination and its variation across the world is shown in Figure 4.6. If the Earth’s magnetic field were truly a magnetic dipole with its north and south poles at the Earth’s geographic south and north poles, respectively, the declination everywhere on the Earth would be exactly  $0^\circ$ .

#### 4.1.5 Ionospheric Profiles

The ionosphere exhibits tremendous variability, and the leakage of VLF energy into the plasmasphere is generally highly dependent on the ionospheric composition at the time. In particular, we have found that the simulated upgoing power flux can change by as much as  $\pm 10$  dB depending on what daytime ionosphere is used. Varying the nighttime ionosphere between extremes typically encountered, however, only changes the simulation result by approximately 0.2 dB. Therefore, we conducted 10 different daytime simulations having varying electron densities and just a single nighttime simulation, which, it should be noted is fortuitous since the nighttime

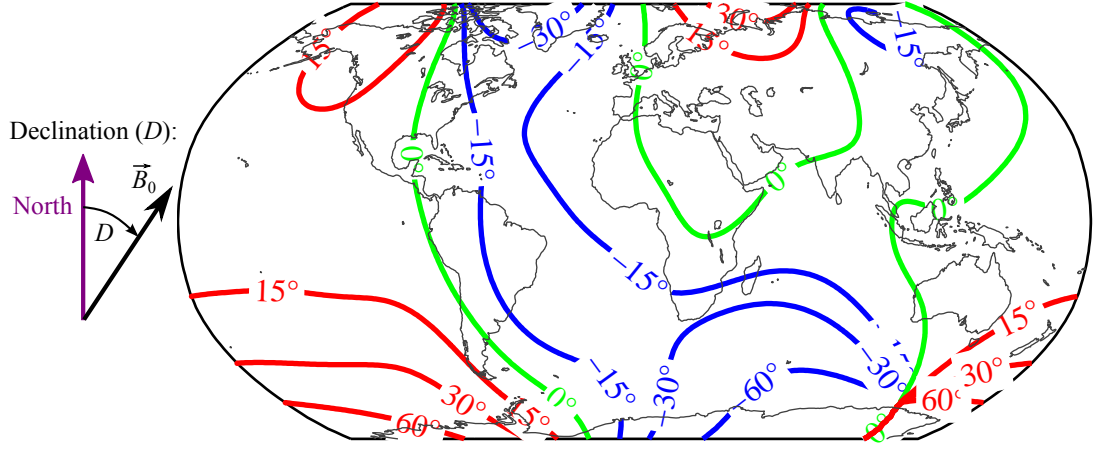


**Figure 4.6:** Earth's magnetic field declination given by the IGRF.

simulations take much longer to complete than the daytime ones. The various profiles used are given in Figure 4.7.

To determine which daytime simulation to use at a particular point in time and space, we find which of the 10 electron density profiles most closely matches the electron density given by the IRI at the point. However, because the electron density at lower altitudes has a larger impact on the simulation result than the density at higher altitudes, a weighting function given by

$$w(h) = \begin{cases} 2 - e^{0.2(h-110)}, & h < 110 \\ e^{-0.2(h-110)}, & h \geq 110 \end{cases} \quad (4.2)$$

for  $h$  in km is applied to preferentially favor the lower altitudes. Specifically, if  $N_{e, \text{IRI}}$  is the IRI electron density at the point of interest and  $N_{e,i}$  is the  $i$ th electron density profile from Figure 4.7, then we seek

$$\arg \min_i \left( \sum_h \left( w(h) |N_{e, \text{IRI}}(h) - N_{e,i}(h)|^2 \right) \right). \quad (4.3)$$

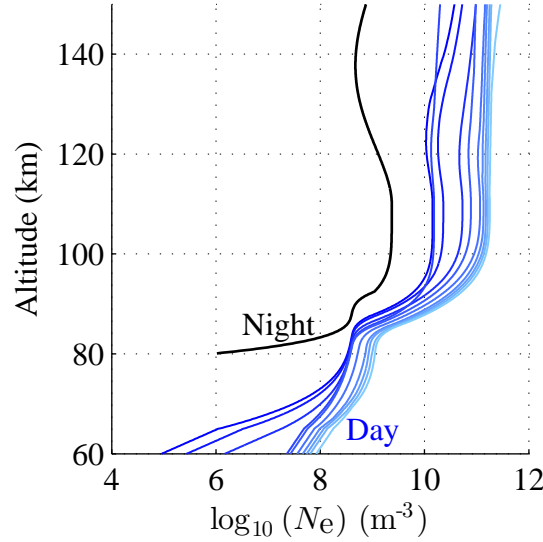


**Figure 4.7:** Electron density profiles used in the global FWM simulations. The various blue shades are the daytime profiles, and the black line is the nighttime profile.

#### 4.1.6 Procedure to Compute Power Flux

To summarize and synthesize what has been described thus far in this section, we first compute the lightning return stroke peak current density on a  $1^\circ \times 1^\circ$  latitude/longitude grid on the Earth from the GLD360. FWM simulations are conducted for 1 nighttime ionosphere and 10 daytime ionospheres with inclinations varying between  $0^\circ$  and  $88^\circ$  in  $4^\circ$  increments. For each of those return stroke peak current densities we get from the GLD360, we find the simulation run that most closely matches the conditions given by the IRI and the IGRF (specifically, the electron density and magnetic field inclination). Finally, we rotate the simulation result by the declination value (also provided by the IGRF) at the point of interest.

What remains, then, is to compute the upgoing power flux. The FWM fundamentally calculates the frequency-domain electric- and magnetic-field vector components due to (in our case) a single vertically-directed current source. The units of those vector components, after the proper normalization by the Bruce-Golde return stroke model, are, respectively,  $\text{V/m/kA/Hz}$  and  $\text{A/m/kA/Hz}$ . The upgoing power flux in general is given by the  $z$ -component of the Poynting vector  $\vec{S}$ , which in complex form

is given by:

$$\vec{S} = \frac{1}{2} \text{Re} \{ \vec{E} \times \vec{H}^* \}. \quad (4.4)$$

The units of  $\vec{S}$  in (4.4) are thus  $\text{W}/\text{m}^2/\text{kA}^2/\text{Hz}^2$ . We are actually interested in the total outgoing power flow (in  $\text{W}/\text{kA}^2/\text{Hz}^2$ ) rather than the surface power density, which we can determine for each nearby surrounding latitude and longitude by integrating the surface power flux density given by  $S_z$  over the horizontal grid points saved in the simulation. Recall that the simulations extend to about  $\pm 4.5^\circ$  in latitude, meaning that the FWM simulation calculation for a single latitude/longitude coordinate provides a power flow to coordinates as much as  $4.5^\circ$  away in latitude and at least that much in longitude as well. The result is many overlapping squares of varying outgoing power flows.

It is important to note here that the upgoing power flux squares just computed above are actually for the case of a single, vertically-directed lightning return stroke current source located at the center of each of the squares. In actuality, the lightning is the result of many various return strokes located throughout the area, which we represent as a return stroke peak current density in  $\text{kA}^2/\text{km}^2/\text{year}$ . Therefore, the next step is to scale each square by the return stroke peak current density at that coordinate, resulting in a power flux surface density in  $\text{W}/\text{km}^2/\text{Hz}$ . At this point, the contributions from all the overlapping squares are summed to yield a single power flux at every grid point.

The FWM operates in the frequency domain, and so the resulting power fluxes as computed thus far are functions of frequency. Specifically, the daytime simulations are computed for frequencies  $f = 15 \text{ kHz} \times 1.05^n$  with  $n = -48, -44, \dots, -4$ , and the nighttime simulations have the same frequencies as well as those with  $n = 0, 4, \dots, 24$ . For frequency dependent processes, it can be instructive to preserve the power flux as a function of frequency, and so in the results that follow, power fluxes with units  $\text{W}/\text{km}^2/\text{Hz}$  are given for a specific frequency in the bandwidth. The total power flux over the entire bandwidth in units of  $\text{W}/\text{km}^2$  is then given by integrating the power flux over frequency.

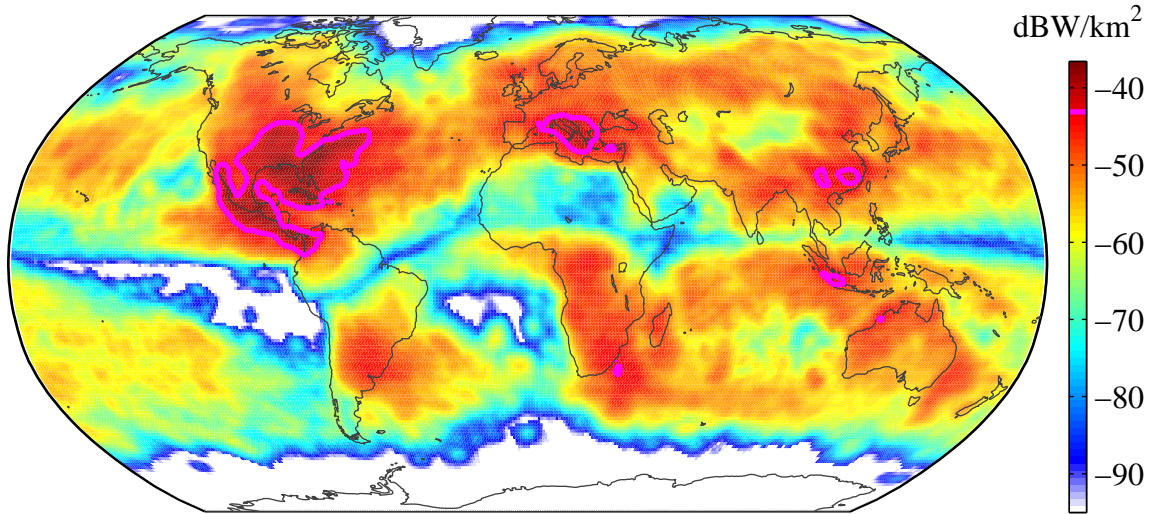


**Figure 4.8:** Total average upgoing power flux at 150 km altitude due to all of the lightning in the year 2014 across the entire globe. The magenta line denotes the approximate equivalent surface power density that results in a 10 pT wave at the equator 3% of the time, which is the value *Abel and Thorne [1998a]* used in their calculations.

## 4.2 Results

### 4.2.1 Global Average Power Flux

Perhaps the most natural result to show first is the total average upgoing power flux at 150 km across the globe over the entire year of 2014 without segmenting by, for example, season or day/night. That result is provided in Figure 4.8. Note that the map generally compares with the lightning return stroke peak current density map given in Figure 4.1 over for example North America. However, the regions of strong lightning activity where the magnetic inclination is close to  $0^\circ$ , such as over South America and Southeast Asia, do not show a corresponding large amount of upgoing power flux. The fact that the magnetic field is mostly horizontal there is not conducive to transmission of whistler-mode waves into the ionosphere, and hence most of the wave energy stays within the Earth-ionosphere waveguide in such regions.



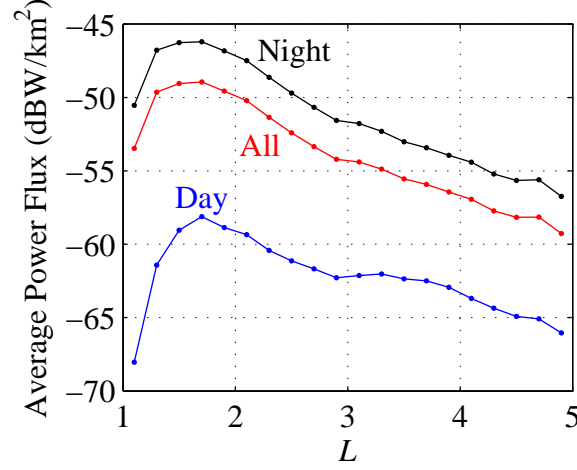


**Figure 4.9:** Total average power input into a given  $L$ -shell at night (black), during the day (blue), and finally the average power across both day and night (red).

#### 4.2.2 Power Through a Given $L$ -shell

A convenient parameter used in studies of the radiation belts is the McIlwain  $L$ -shell. A particle on a given  $L$ -shell remains on that  $L$ -shell as it longitudinally drifts around the Earth [McIlwain, 1961]. In the case of a dipole magnetic field, a particular  $L$ -shell describes a magnetic field line that crosses the dipole's equatorial plane  $L$  radii away from the center of the dipole. Because Earth's magnetic field is approximately dipolar, the  $L$ -shell is often thought of as that magnetic field line that crosses the Earth's equator  $L$  Earth radii away from the Earth. We can compute the average power flux into different  $L$ -shells, as shown in Figure 4.9, by averaging the surface power density from Figure 4.8 across the  $L$ -shell for each point. Specifically, we find the  $L$ -shell at each grid point and then histogram the average surface power density at all the grid points with  $L$ -shells between  $1 < L \leq 1.2$ ,  $1.2 < L \leq 1.4$ , etc. up to  $L = 5$ .

After a sharp drop-off for low  $L$ -shells corresponding to low inclination-angle propagation, the lightning power reaches a maximum at around  $L = 1.7$  for the night, day, and overall average case. The power injection then drops off approximately linearly on a dB scale over the entire range all the way to  $L = 5$ , although the daytime case shows a slight plateau at around  $L = 3.3$ . There is more than 10 dB less power



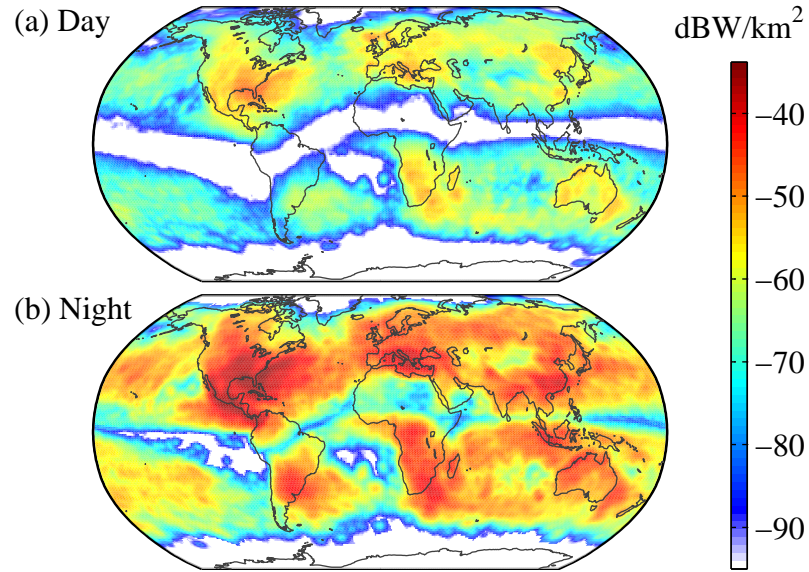


**Figure 4.10:** Total average power flux at 150 km altitude due to lightning both (a) during the day and (b) at night.

injected near  $L = 5$  than there is near the peak at  $L = 1.7$ .

### 4.2.3 Nighttime and Daytime Dependence

In Figure 4.10, we provide separate maps for lightning occurrence in both the daytime hours and the nighttime hours. The first thing to note here is that despite the fact that more lightning occurs during the day than at night, much less power emerges out of the ionosphere during the day. In fact, compared with Figure 4.8, the total average power injected into the plasmasphere is predominantly set by the power injected at night. The daytime injection provides a relatively negligible contribution to the total average.

Another thing to note is that the magnetic equator is much more pronounced in the daytime map than at night. In fact, almost no power propagates out of the ionosphere when the inclination is near  $0^\circ$  as evidenced by the white band crossing the middle of Figure 4.10(a). Yet in Figure 4.10(b), while there is certainly attenuation of the total power at the magnetic equator, the power is not negligible. Thus, the magnetic field inclination has a much stronger effect on the propagation through the

ionosphere during the day than at night. This result can be further seen in Figure 4.9, where the average power injected is plotted as a function of  $L$ -shell for both the day (blue) and night (black) cases. The average power during the day shows a steeper drop-off for  $L < 1.7$  than the nighttime result.

#### 4.2.4 Seasonal Dependence

Lightning on average is seasonal: more lightning occurs during the summer than in winter. Therefore, one would expect there to be more lightning power input into the plasmasphere in the southern hemisphere in January/February/March than in July/August/September, and vice versa for the northern hemisphere. We can see that such is indeed the case by viewing Figure 4.11, which shows the total average power flux in the four quarters of the year 2014 for both day and night. In the northern hemisphere, there is much more power in the months of July, August, and September (the third row of Figure 4.11) than in the first three months of the year (the top row of the same figure), while the opposite is true for the southern hemisphere.

### 4.3 Discussion

Thus far, the results we have presented have been the upgoing power flux of the electromagnetic waves radiated by lightning at an altitude of 150 km. In analyses of the effect of lightning on the radiation belts, what is typically desired is the magnetic field wave amplitude in the radiation belts themselves. To find the wave amplitude in the radiation belts from VLF transmitters from upgoing power flux calculations in the ionosphere, *Inan et al.* [1984] assumed that the VLF wave propagation was entirely “ducted” along Earth’s magnetic field lines due to enhancements of the electron plasma density along the magnetic field line. Then, the wave surface power density  $S$  at any point in the propagation path is given by

$$S = \frac{\omega_{ce}}{\omega_{ce,150\text{ km}}} S_{150\text{ km}} = \frac{B_0}{B_{0,150\text{ km}}} S_{150\text{ km}}, \quad (4.5)$$

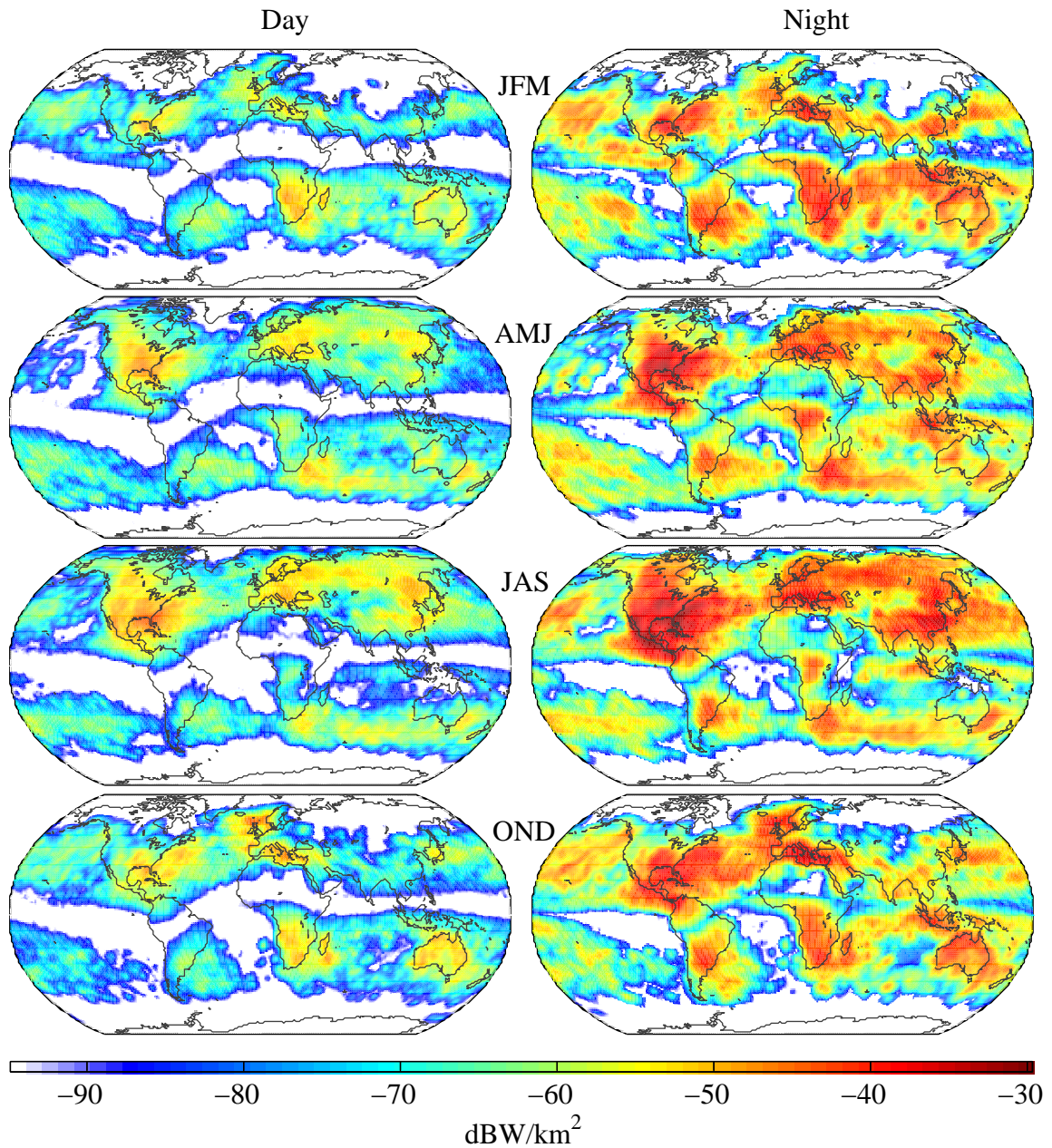


**Figure 4.11:** Total average power flux at 150 km altitude due to lightning for day (left column) and night (right column) split into the four quarters of the year 2014. The first row is January, February, and March (JFM), the second row is April, May, and June (AMJ), the third row is July, August, and September (JAS), and the last row is October, November, and December (OND).

where  $\omega_{ce}$  and  $B_0$  are the electron gyrofrequency and Earth's magnetic field strength at the desired point in the propagation path, respectively,  $\omega_{ce,150\text{ km}}$  and  $B_{0,150\text{ km}}$  are the same at 150 km altitude along the same path, and  $S_{150\text{ km}}$  is the wave surface power density at 150 km. Despite the fact that this is a fairly simplistic representation of the true propagation (as most of the VLF waves are likely non-ducted [*Smith and Angerami, 1968*]), that assumption is computationally much faster and approximates at least some of the conditions under which VLF waves are known to propagate in the plasmasphere. *Abel and Thorne [1998a]* also utilized the same technique to estimate wave amplitudes in the radiation belts due to terrestrial VLF waves. *Starks et al. [2008]* utilized a full three dimensional ray tracer program in an attempt to avoid any ambiguity about whether a given wave is ducted or not, although even that model is highly dependent on the input plasma density in the ionosphere and plasmasphere.

Acknowledging the difficulty in determining wave amplitudes from upgoing power flux densities at the lower ionosphere, we have therefore opted to simply present the upgoing power flux at the ionosphere and as such avoid any issues as to whether our propagation model from the ionosphere to the plasmasphere is representative of the actual conditions. Despite the fact that previous estimates of the lightning energy in the plasmasphere are often given as the wave magnetic field amplitude there rather than the surface power density at the ionosphere, it would still be useful to compare our estimate with previous ones.

In a survey of perturbations of sub-ionospheric VLF transmissions presumably caused by precipitating electrons, *Burgess and Inan [1993]* found a year-round average whistler occurrence rate at Palmer Station, Antarctica ( $L = 2.42$ ) of 6 /minute. An analysis of 59 whistlers that were associated with VLF signal perturbations indicating electron precipitation yielded an average wave magnetic field at the equator of 12 pT, which was reportedly determined by applying the method of *Inan et al. [1984]* to the measured whistler amplitudes at Palmer. To determine the upgoing power density that results in a wave amplitude at the equator of 12 pT, we apply the reverse of the same method with the following assumptions:

1. The electron density at the equator is  $10^3\text{ cm}^{-3}$ .



2. The wave frequency is 5 kHz.
3. The Earth’s magnetic field is a dipole, and the whistler is at  $L = 2.5$ , so that the ratio of the magnetic field intensity at the equator to that at the ionosphere as given in (4.5) is approximately 1.44.

The result of these assumptions is that the whistler surface power density at the ionosphere is about  $-27.9$  dBW/km<sup>2</sup>.

*Abel and Thorne* [1998b] in turn derived their estimate of a 10 pT wave amplitude due to lightning generated whistlers from the whistler rate and amplitude given by *Burgess and Inan* [1993]. By assuming that each whistler component lasts 30 ms, the whistler occurrence rate was assumed to be 3%. Multiplying that percentage by the power density at the ionosphere computed above results in an average power density of  $-43.2$  dBW/km<sup>2</sup>. That power density is marked on Figure 4.8 with a magenta line. Clearly, there are places when that estimate is accurate and other times when it is either an over or under estimate, yet most of the world on average shows an underestimate. Checking the power density of  $-43.2$  dBW/km<sup>2</sup> against Figure 4.9 indeed suggests that on average, *Abel and Thorne* [1998b] likely overestimated the lightning wave amplitude in the plasmasphere, as the overall peak average at  $L = 1.7$  is closer to  $-50$  dBW/km<sup>2</sup> than  $-43.2$  dBW/km<sup>2</sup>. Also, *Abel and Thorne* [1998b] assumed a constant wave amplitude  $1.2 < L < 4$  while Figure 4.9 shows that the power density rises sharply up to its peak before decaying linearly on a dB scale.

A more thorough estimate of the VLF wave energy entering the plasmasphere was conducted by *Colman and Starks* [2013]. They constructed a map of “pseudopower” from lightning flash data that was then translated up to the DEMETER satellite’s altitude (660 km) and then scaled that result by the actual average power that DEMETER measured at each of those points. We compare the result presented by *Colman and Starks* [2013] with our own results in Figure 4.12. It should be noted that *Colman and Starks* [2013] reported wave power in  $\mu\text{V}^2/\text{m}^2/\text{Hz}$  while we calculate the surface power density in  $\text{W}^2/\text{km}^2/\text{Hz}$ . Converting between the two units would require knowledge of the refractive index. Rather than introduce a possible error depending on the refractive index used, we simply make a qualitative comparison.

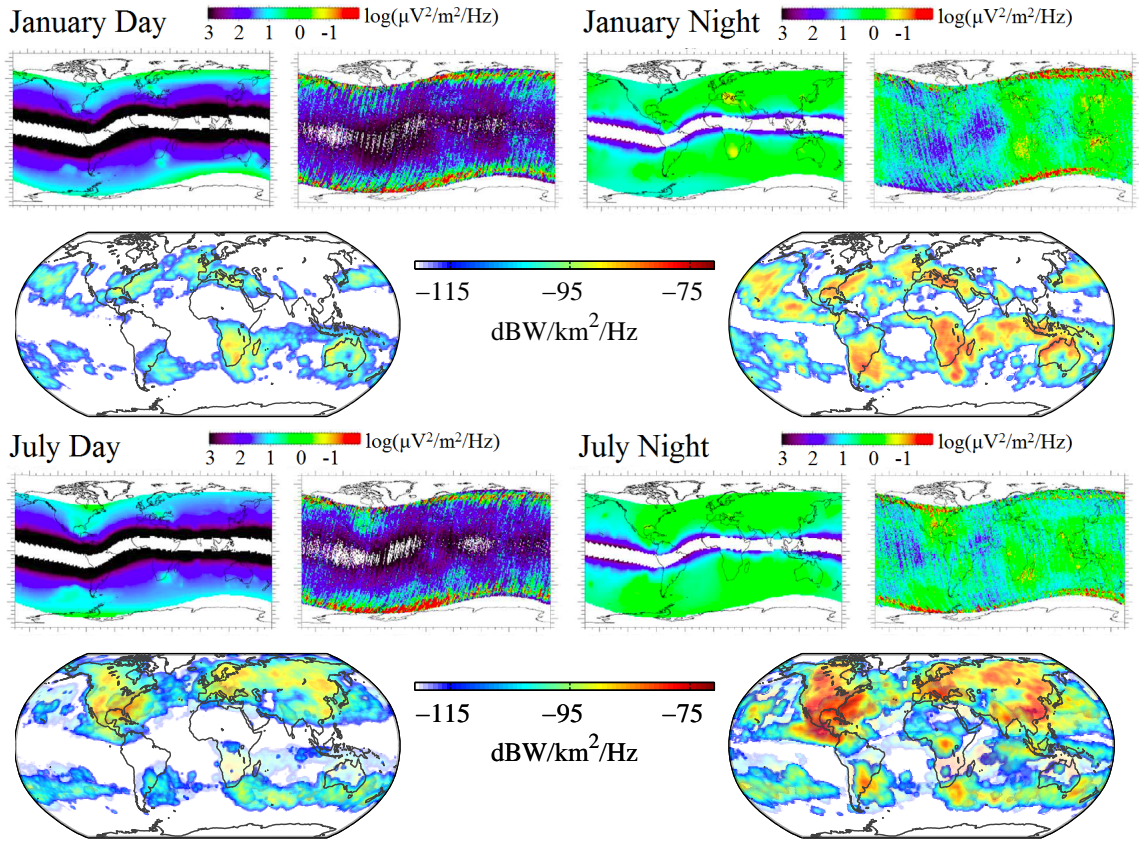


**Figure 4.12:** Global lightning power at 5 kHz as given by the model of *Colman and Starks* [2013], the DEMETER satellite, (rows 1 and 3) and that calculated by the model presented here (rows 2 and 4) for January (rows 1-2) and July (rows 3-4) and day (left) and night (right).

First, the *Colman and Starks* [2013] model, DEMETER data, and our model all show less power during the day than at night. All three also show the same seasonal variation. There is more lightning energy over North America in July than in January, for example. The *Colman and Starks* [2013] model and DEMETER data both include conjugate reflection of the wave energy, which our model does not include, and so our model does not have a large amount of wave power off the southwest coast of South America like the *Colman and Starks* [2013] model and DEMETER data do. Except for that, the graphs all show many of the same features overall. Interestingly, though, the magnetic equator in the model calculation of *Colman and Starks* [2013] significantly

attenuates the total wave power not only during the day and but also at night, while in our case, the magnetic equator does not have nearly as strong an effect on the transmission at night as it does in the day. The DEMETER measurements agree more with our model in not having strong attenuation along the magnetic equator at night.

## 4.4 Conclusions

We have presented the result of translating global lightning occurrence data derived from the GLD360 to an upgoing power flux density at 150 km altitude. In order to avoid introducing any errors in our calculation due to misrepresenting the wave propagation from the ionosphere into the plasmasphere, we have opted to leave our results as such and not calculate a wave amplitude in the plasmasphere itself.

The resulting power estimate compares relatively closely with the wave power due to lightning that *Abel and Thorne* [1998a] used in their analysis of the impact of various waves on the radiation belts, although we show almost  $-6$  dBW/km<sup>2</sup> less power injected at the peak than they assumed. Also, it must be noted that *Abel and Thorne* [1998a] assumed a constant wave amplitude over the entire range  $1.2 < L < 4$ , whereas our results from Figure 4.9 suggest that there may be as much as a 10 dB difference in lightning power across that range of  $L$ -shells. Therefore, it is advisable to conduct a new analysis using the global lightning power estimate we have presented here.

Our power estimate also compares qualitatively with that determined by *Colman and Starks* [2013] and DEMETER satellite measurements. In fact, our conclusion that the magnetic equator does not significantly attenuate whistler power in the ionosphere at night is borne out in DEMETER satellite measurements.

## Chapter 5

# Conclusions and Suggestions for Future Work

Throughout this thesis, we describe our efforts to better understand and quantify the propagation of the electromagnetic waves radiated by lightning through the Earth’s ionosphere and into the plasmasphere and the Van Allen radiation belts. We used measurements of those waves taken on board satellites as well as numerical modeling. In this final chapter, we present some conclusions of our work and offer some suggestions for future work that might extend what we present here.

### 5.1 Conclusions

In Chapter 2, we lay out an algorithm that can be used to automatically detect and identify  $0^+$  whistlers on board a low Earth orbiting satellite, with an application especially geared towards the TARANIS satellite. The algorithm is implementable on an FPGA and is thus well-suited to be part of the satellite payload. The algorithm is applied to data from the DEMETER satellite, which faced similar conditions that TARANIS is expected to see, and successfully identify many of the  $0^+$  whistlers observed there. Data from the instrument, which will be received after TARANIS launches in 2018, will likely find many applications. In particular as it relates to this thesis, the data could lead to an estimate of the amount of lightning energy



propagating up into the plasmasphere on a large scale and also be compared with data from global lightning detection networks.

Next, we show the results of our numerical simulations of lightning generated whistler propagation through the ionosphere as computed by the Full Wave Method (FWM) and compare these results with measurements taken from the DEMETER satellite. This study was motivated in large part due to the discrepancy between numerical models and measurements that *Starks et al.* [2008] uncovered. Our simulations show a slight underestimate of the field strengths than that measured on the satellite, with the magnetic fields having a smaller discrepancy than the electric fields. The variation in the discrepancy of the electric fields over frequency lead us to conclude that at least some of the discrepancy could be due to a miscalibration of the DEMETER data.

Finally, despite the discrepancy between the FWM simulations and DEMETER measurements, we apply the FWM to global lightning across the world in order to estimate globally the amount of lightning propagating out through the ionosphere and into the plasmasphere. We compare our estimate with previous estimates used in models of radiation belt electron lifetimes and find relatively close agreement. However, we make the argument that our estimate invokes fewer assumptions (such as a uniform distribution of lightning energy across the globe) that suggest future models should utilize our results in their calculations.

## 5.2 Suggestions For Future Work

There are a number of avenues to explore which could further expand on the work presented in this thesis. We suggest some of those here.

### 5.2.1 $0^+$ Whistler Detection Algorithm

Recall in Section 2.4 that we suggest a number of improvements to the automatic  $0^+$  whistler detection algorithm. Implementing those suggestions to further refine and improve the performance of the algorithm would clearly be attractive. Note that

less than half of the nighttime  $0^+$  whistlers we labeled by hand are identified by the algorithm using the optimum parameters from Table 2.2, and so there is significant room for improvement. By allowing more parameters to vary in more ways, the algorithm would likely be able to detect even more  $0^+$  whistlers without significantly increasing, or even possibly decreasing, the number of false positives.

Similarly, nothing in principle would prevent the algorithm from being used to detect whistlers more dispersed than  $0^+$  ones, such as  $1^-$ ,  $1^+$ , etc. Doing so would just require a readjustment of the parameters. Analysis along those lines could result in a general whistler detection algorithm rather than one specifically suited to  $0^+$  whistlers that we present.

There are also other means to characterize the algorithm. For example, one could characterize it with a different objective in mind, such as minimizing the number of false positives. Or possibly one may be more interested in very strong  $0^+$  whistlers rather than weak ones. As it is, we do not distinguish between weak and strong signals. Additionally, we characterize the algorithm in a general sense that is supposed to represent a variety of environmental conditions and noise levels. If one instead characterizes different environmental conditions separately, one could ensure the algorithm performance of the algorithm optimally in each of those cases individually.

Finally, the algorithm could easily be applied to the entire 6 year set of burst mode data from DEMETER to provide a more robust estimate of the global distribution of  $0^+$  whistlers. The computation time would be long, but not prohibitively so. Data from that analysis could provide a useful check on the computed estimate of  $0^+$  whistler energy given in Chapter 4. Utilizing the algorithm to definitively identify the contributions in the DEMETER data due to  $0^+$  whistlers would remove the ambiguity present in the survey mode data as to the source of the energy and thus provide a closer estimate to what we presented in this thesis than *Colman and Starks [2013]* computed.

### 5.2.2 Comparison of FWM and DEMETER Measurements

The most pressing issue in the comparison of the FWM with DEMETER measurements is the discrepancy between the two data sets. So first and foremost, future work on that front should be directed towards resolving that discrepancy. We suggest that the discrepancy might be due to a miscalibration of the electric field data on DEMETER. Because the calibration depends on the background electron density, and the data we utilize in our study was collected during solar minimum almost five years after the start of the DEMETER mission, a similar study using data collected earlier in the mission could provide some insight into whether the electric field data during that time are closer to what the FWM predicts. Alternatively, the ionosphere input into the FWM could be varied. Another possibility would be to use data from another satellite entirely, which would remove any question about the calibration of the DEMETER instrument specifically. Of course, the upcoming TARANIS mission presents an excellent opportunity to revisit this issue.

### 5.2.3 Global Estimate of Lightning Energy

First of all, there is probably room to further refine the global estimate of the lightning energy propagating into the plasmasphere that we computed in Chapter 4. In particular, the lateral extent of our simulations out to only 500 km allows us to capture approximately 80% of the total power propagating up. Extending that further would allow for a more accurate power estimate at the expense of longer computation time. Ideally the simulations would also account for the Earth's curvature, as that does start to become significant for larger distances. More ionosphere profiles and magnetic field inclinations could also yield a more refined estimate.

The computation of the global lightning energy propagating into the plasmasphere is made with the idea of its being used in models of radiation belt lifetimes, and so it is only natural to utilize the data presented here in one of those models and observe the effect. In particular, the whistler wave amplitude could be adjusted over different  $L$ -shells as suggested by Figure 4.9.

# Appendix A

## FPGA on TARANIS Satellite

Recall from Chapter 2 that the TARANIS satellite, expected to launch in 2018, will carry an Field Programmable Gate Array (FPGA) to automatically detect  $0^+$  whistlers utilizing the algorithm developed for this thesis. The instrument is known as the  $0^+$  detector (ZPD), and the specifics of how the algorithm was implemented on the Actel AX 2000 FPGA selected for that purpose are presented in this Appendix. We utilize the Verilog hardware description language.

### A.1 System Architecture

A block diagram of the signal path from the antenna through the ZPD is given in Figure A.1. First, the analog wave field data from either the electric or magnetic antenna, depending on the operational mode, are converted to 12-bit digital numbers using a radiation hardened RHF1201 analog to digital converter (ADC) sampled at  $f_s = 2$  MHz and input to the ZPD. Next, the data are downsampled by a factor of 64, and then the spectrograms of the data are computed. Finally, the spectrograms are input into the algorithm, and when the algorithm detects a  $0^+$  whistler, information on the event is output to the SN74V623 external FIFO memory to be read by the MF-A and downloaded to the ground. The input command to the instrument sets various parameters of the algorithm.

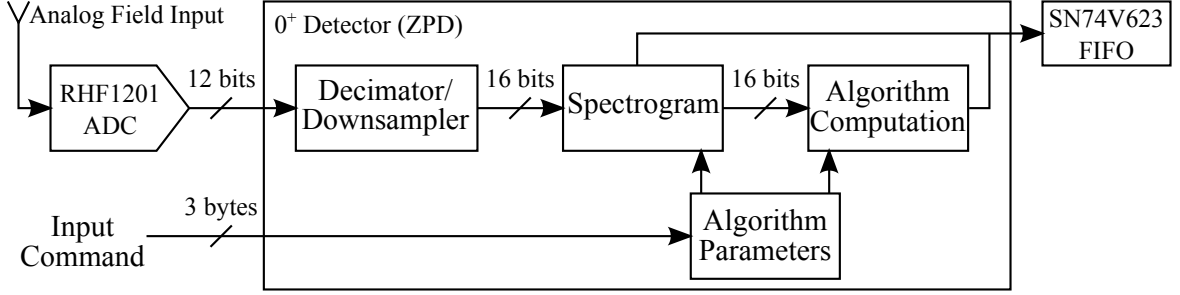


**Figure A.1:** Block diagram of the  $0^+$  detector. The analog field input is converted to digital by the ADC, which is then input into the ZPD. After processing within the ZPD, information on the detected  $0^+$  whistlers is output to the external FIFO.

### A.1.1 Decimator

Because sferic and whistler energy is predominantly concentrated in the VLF range, a sample rate of  $f_s = 2$  MHz is unnecessarily high for detection of  $0^+$  whistlers. Therefore, to increase the signal to quantization noise ratio (SQNR) and reduce the computation load, the input ADC data are immediately downsampled (also known as decimated) by a factor of  $M = 64$ , resulting in a new sampling frequency of  $f_s = 31.25$  kHz.

To avoid aliasing, data must be low pass filtered before the sample rate can be reduced. A general block diagram of a decimator by  $M$  appears in Figure A.2. First, the data are low-pass filtered with a normalized cut-off frequency  $\hat{\omega} = \pi/M$  followed by a downsampling block that removes every  $M - 1$  samples (keeping every  $M$ th sample). The ZPD decimates in two stages: The first stage is a cascaded integrator comb (CIC) filter [Hogenauer, 1981] decimating by  $M_1 = 32$ , which is then followed by a finite impulse response (FIR) compensator filter that decimates by  $M_2 = 2$ .

Decimation can be challenging for large downsampling rates because of the difficulty in making low pass filters with the small cut-off frequencies necessary to avoid aliasing. However, CIC filters have a number of advantages over other decimation techniques that make them well suited for decimating by large rates. First, CIC filters perform no multiplications, just addition/subtraction and delays (registers on an FPGA), and hence tend to be more economical and computationally efficient than comparable FIR filters, which get exponentially bigger with increasing decimation

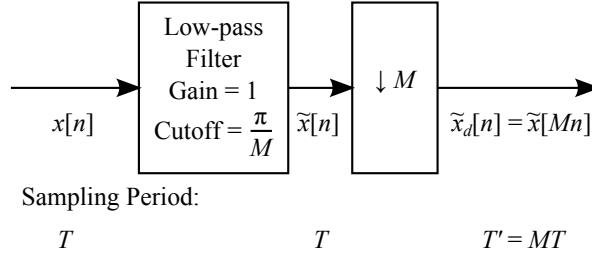


**Figure A.2:** Decimator by  $M$ . The input data are first low pass filtered, and then every  $M - 1$  samples are removed, which ultimately increases the sampling period from  $T$  to  $MT$ .

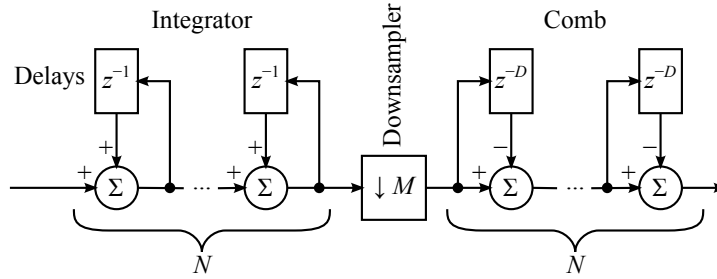


**Figure A.3:** Cascaded integrator comb (CIC) filter. A total of  $N$  integrators precedes a block that removes every  $M - 1$  samples, which is then followed by  $N$  comb blocks.

rates; see Figure A.3 for a block diagram of a general CIC decimator. Second, CIC filters have a linear phase response, unlike infinite impulse response (IIR) filters.

As shown in Figure A.3, an  $N$ -stage CIC filter is composed of  $N$  first order cascaded integrators followed by a downsampler and another  $N$  first order cascaded combs. Parameters of a CIC filter are the number of stages  $N$ , the differential delay  $D$ , and the downsampling rate  $M$ . The system transfer function of a CIC filter is

$$H(z) = \left( \frac{1 - z^{-DM}}{1 - z^{-1}} \right)^N. \quad (\text{A.1})$$

It has zeros at  $z_n = e^{j\frac{2\pi n}{DM}}$ ,  $n = 0, 1, \dots, N - 1$  and a pole at  $p = 1$  (which normally would result in an unstable filter, but this pole cancels with the zero for  $n = 0$ ). The

magnitude of (A.1) can be approximated for large values of  $M$  as

$$|H(z = e^{j2\pi f})| = \left| \frac{\sin(\pi f D)}{\sin\left(\frac{\pi f}{M}\right)} \right|^N \simeq \left| D M \frac{\sin(\pi f D)}{\pi f D} \right|^N, \quad (\text{A.2})$$

which is simply a sinc function. The  $0^+$  whistler detector achieves greater than 80 dB attenuation in the aliasing band of the CIC filter for  $M_1 = 32$  with  $N = 8$  and  $D = 1$ .

One of the disadvantages of using CIC filters is the inability to create arbitrary passband shapes: Only a sinc function magnitude response is possible. In order to get a CIC filter with a large stop-band attenuation, it will necessarily have significant pass-band attenuation that is typically called “pass-band droop” in CIC filters. The CIC filter’s gradual roll-off and pass-band droop can be mitigated by following a CIC with a FIR filter that has the inverse response in the pass band—resulting in a flat pass band in the cascaded system—and a steep roll off in the stop band. The ZPD has a FIR compensator with a cut-off frequency at  $\pi/2$  and 64 symmetric coefficients, and a downsampler by  $M_2 = 2$  follows the compensator, resulting in a total downsampling rate of  $M = M_1 M_2 = 64$  for the entire system.

The magnitude and phase response of the decimator used in the ZPD is shown in Figure A.4. Note that the stop-band attenuation is greater than 90 dB except for the small band with close to 80 dB attenuation, which will alias into the already unusable FIR filter’s transition region. Decimating the 12-bit input data by a factor  $M = 64$  increases the effective number of bits by  $0.5 \log_2(M) = 3$ , resulting in 15-bit effective output data. Data with 15 bits has an SQNR of about 90 dB, so with the aliasing bands also attenuated by more than 90 dB, the output of the decimator can be effectively represented with 15 bits. The ZPD passes 16 bits of the decimator output as an additional margin over the effective number of bits.

### A.1.2 Spectrogram

The next step in the algorithm requires taking the spectrogram of the input signal. Recall from Section 2.2.1 that the spectrogram is the magnitude of the Short Fourier

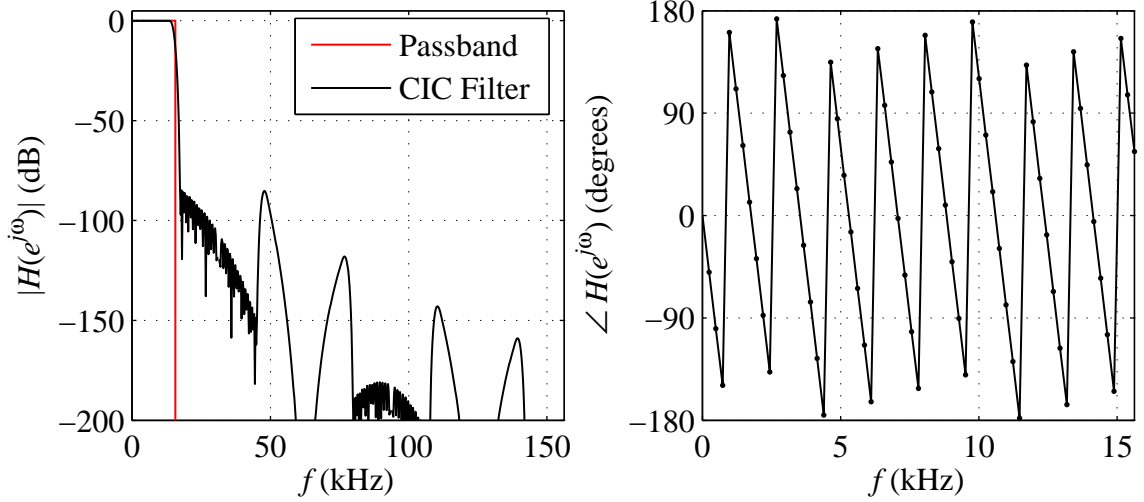


**Figure A.4:** Frequency response of the decimator used in the ZPD. The ideal passband is denoted in red, and the actual filter response is shown in black.

Transform (STFT), repeated here as:

$$\text{STFT}\{x[k]\} = s[m, n] = \sum_{k=0}^{N-1} \left( x[k - (N - O)n]w[k]e^{-j2\pi \frac{km}{N}} \right), \quad (\text{A.3})$$

where the parameters of the STFT are:

- $N$  is the discrete Fourier transform (DFT) length.
- $O$  is the number of points to overlap between successive times.
- $w[k]$  is the windowing function. Also, let  $W$  be the largest  $k$  that satisfies  $w[k - 1] \neq 0$  (i.e., the length of the windowing function).

Computing the spectrogram requires computation of a discrete Fourier transform. When the length of the DFT is a power of 2, a technique known as the fast Fourier transform (FFT) can be used to greatly reduce the computation time of the DFT [Cooley and Tukey, 1965], and so the ZPD uses a power of 2 for the length of the DFT. We wrote a FFT algorithm in Verilog with a user-configurable length, although the ZPD uses  $N = 128$ . Additionally, the overlap is 50% and the windowing function has the same length as the DFT so that  $O = 64$  and  $W = 128$ . Given a sampling



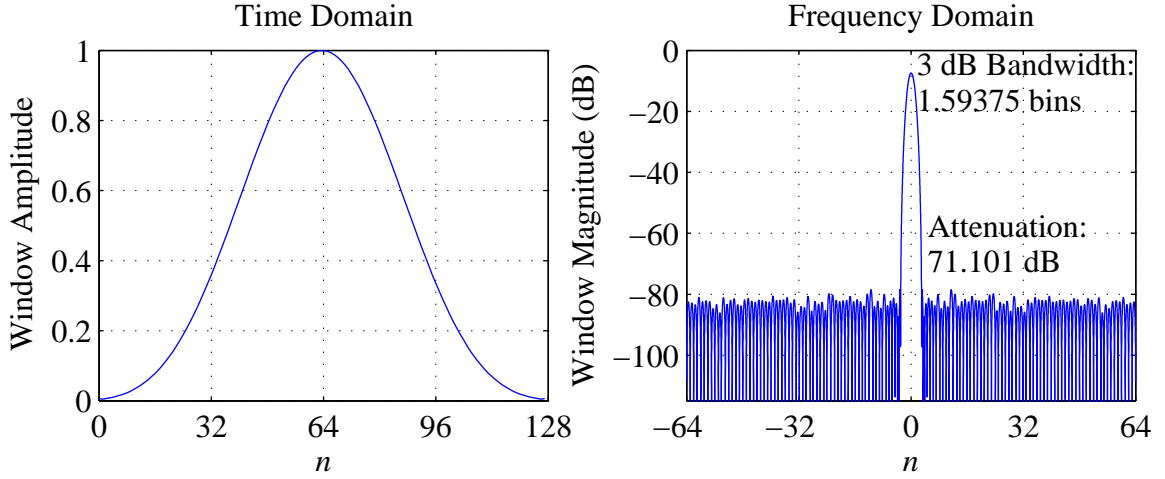


**Figure A.5:** Windowing function used in the STFT. On the left is the time domain representation of the windowing function, and the right shows the Fourier transform of the function.

frequency of  $f_s = 31.25$  kHz, these parameters set the spacing between frequency bins to  $\Delta f \approx 244$  Hz and the spacing between time bins to  $\Delta t = 2.048$  ms. There is also an option between computing the linear magnitude or  $\log_2$  magnitude, with the latter computed as a look up table.

The windowing function used is a Dolph-Chebyshev window. A windowing function designed with Chebyshev polynomials, having first been used in the design of antenna arrays [Dolph, 1946], minimizes the window's main lobe width for a given side-lobe attenuation level [Harris, 1978]. Dolph-Chebyshev windows have the disadvantage that the terms are computationally intensive to calculate, but that is minimized on the FPGA by implementing the windowing function as a look-up table with the terms quantized to 12 bits. Quantization of the terms sets the maximum theoretical attenuation to approximately 72 dB. Plots of the quantized windowing function in the time domain and frequency domain are shown in Figure A.5.

The spectrogram values are stored in a  $64 \times 64$  RAM module inside the FPGA. Therefore,  $A$  and  $C$  must sum to 64, and we set them to 16 and 48, respectively.

### A.1.3 Algorithm Computation

Finally, the FPGA computes the cross-correlation of the spectrogram with the expected whistler shapes. The shapes are given as a simple look-up table, with the specific table given by the particular input command (as described in Section A.2.1). Note that the whistler shape coefficient matrices generally have more negative than positive values; to compensate for that, the coefficient matrix used is selected from one of two different possibilities depending on the selected science mode. The first is exactly the same as described by (2.10), and the other replaces  $-1$  in (2.10) with  $-0.7578125$ , which was chosen to make the sum of all the terms in the matrix be approximately zero for all the different possible dispersion constants the ZPD uses.

The ZPD can optionally be set to require  $\rho_l[n]$  and  $\gamma_l[n]$  of (2.13) from to exceed some thresholds  $R$  and  $Q$ , which the ZPD sets to be 7 and 10 respectively, in addition to the requirement that  $b[n]$  be a local maximum and equals or exceeds some threshold  $T$ . In that case, the specific  $\rho_l[n]$  and  $\gamma_l[n]$  that must exceed  $R$  and  $Q$  are for the particular  $l$  and  $n$  that meet the requirement on  $b[n]$  in (2.12).

## A.2 Input and Output Description

As shown in Figure A.1, the ZPD receives as input a digitized analog field and three command/configuration bytes that set algorithm parameters and outputs data to an external FIFO. This section details the exact format of the input command/configuration bytes and output modes. The ZPD will be given a different set of three command/configuration bytes at the beginning of each TARANIS half orbit immediately after being awakened from reset at the end of the previous half orbit. The instrument will exclusively use the three command/configuration bytes received at the beginning of the half orbit over the entire half orbit; in other words, it is not possible to change any of the input bytes midway through a half orbit. The protocol that the ZPD and the rest of the satellite use to relay the command/configuration bytes is detailed in the internal interface document supplied by LPC2E and summarized here. The output data are written in blocks of TARANIS packets following the protocol specified

**Table A.1:** Science Mode Options

Science Mode	Mode Bits		Spectrogram Magnitude	Neg. Coef. Value	Threshold Rows/Cols
	(Binary)	(Hexadecimal)			
1 (Default)	0000/0001	0x0/0x1	Logarithmic	−1	No
2	0010	0x2	Logarithmic	−1	Yes
3	0011	0x3	Logarithmic	−0.7578125	No
4	0100	0x4	Logarithmic	−0.7578125	Yes
5	0101	0x5	Linear	−1	No
6	0110	0x6	Linear	−1	Yes
7	0111	0x7	Linear	−0.7578125	No
8	1000	0x8	Linear	−0.7578125	Yes

in the data sheet for the SN74V623 FIFO memory.

### A.2.1 Input Command/Configuration Bytes

The first byte of the three command/configuration bytes sets the mode in which the ZPD is run. Specifically, the 4 least significant bits of byte 1, known hereafter as the mode bits, specify which of the either eight science modes or four test modes the ZPD will use for the given half orbit; the most significant bits of byte 1 are ignored. If the ZPD receives mode bits that do not correspond to one of the eight science modes or four test modes, it will run in the default science mode and set the ERROR\_SD signal to the satellite high.

The science modes toggle three different options: whether to compute the linear or logarithmic magnitude for the spectrograms, whether the negative value in the whistler coefficient matrix is  $-1$  or  $-0.7578125$ , and whether or not the calculation of (2.13) must exceed thresholds  $R = 10$  and  $Q = 7$ , respectively, in addition to the usual requirement on (2.12) to be a local maximum and exceed  $T$  for the spectrogram to be considered a  $0^+$  whistler. In all of the science modes, data are only output when a spectrogram meets all the criteria to be considered a  $0^+$  whistler. Table A.1 lists the specific options set by each science mode and what 4-bit sequence in the least significant bits of the first command byte is needed in order to select that particular science mode. The default science mode is Science Mode 1.

**Table A.2:** Test Mode Descriptions

Test Mode	Mode Bits (Binary)	Mode Bits (Hexadecimal)	Algorithm Input	Output Data	Output APIDs
A	1010	0xA	Counter	Algorithm	1244-1247
B	1011	0xB	ADC	Algorithm	1244-1247
C	1100	0xC	ADC	Counter	1244-1247
D	1101	0xD	ADC	Algorithm	1244

The four test modes in which the ZPD can be operated, designated A, B, C, and D, vary the input data stream going into the algorithm and the type of output. In all test modes, the ZPD outputs a TARANIS packet approximately once every three seconds regardless of the algorithm computation and threshold selected. The first three test modes A, B, and C cycle through the four APIDs allotted to the ZPD: APID 1244 is output first, APID 1245 is output three seconds later, and so on until APID 1247 is output after about nine seconds, and finally three seconds after that the cycle repeats when APID 1244 is output again. In test mode D, on the other hand, only APID 1244 is output. For the test modes except test mode C, the data in each packet are formatted the same as in a standard science mode ZPD TARANIS packet with the only difference being the data do not represent a detected  $0^+$  whistler; the data in each packet in test mode C are just a counter. The specific format of the ZPD TARANIS data packets, including those for test mode C, will be explained later. In each test mode, the algorithm computation is made using the same parameters as the default science mode—that is, with logarithmic magnitude spectrograms and a negative coefficient value of  $-1$ . Finally, in test mode A, the input to the algorithm is not the ADC data stream like the other science and test modes but just a counter clocked at 10 kHz. The differences between the four test modes are summarized in Table A.2.

The remaining two bytes in the command/configuration bytes set various algorithm parameters. The most significant bit of byte 2 signals whether the satellite is on the dayside (1) or nightside (0) of its half-orbit. That information is important to know because  $0^+$  whistlers tend to be more dispersed in the more ionized daytime

conditions, and so the ZPD uses different expected whistler shapes at night than during the day. The next bit in byte 2 sets whether the input field is the electric field (0) or magnetic field (1). The magnetic field instrument is less sensitive than the electric field instrument, and the magnetic field data input to the ZPD has a low frequency cut-off of 10 kHz and attenuates most of the useful signal in a  $0^+$  whistler. Therefore, the ZPD will primarily use the electric field unless there is a catastrophic failure in that data stream. The remaining six bits in byte 2 are the algorithm threshold  $T$  (see Table 2.1) divided by 4; for example, if the last six bits are 000101 in binary/5 in decimal, the ZPD will use a threshold of  $T = 20$ .

The four most significant bits in byte 3 set the standard deviation parameter  $N_\sigma$  (again see Table 2.1). In the case that the ZPD is running in logarithmic magnitude mode (set in byte 1), the actual  $N_\sigma$  used is the number represented by the 4 most significant bits of byte 3 divided by 2. For example, if the bits are 0101 in binary/5 in decimal, the ZPD will use  $N_\sigma = 2.5$  in science modes 1-4 and all four test modes and use  $N_\sigma = 5$  in science modes 5-8. Finally, the last 4 bits in byte 3 determine which whistler shapes to use. A total of 8 dispersion constants are utilized by the ZPD simultaneously (i.e., there are 8  $D_l$  for  $l = 1, 2, \dots, 8$ ). The smallest and largest  $D_l$  for each possible choice for the least significant bits (LSBs) of byte 3 are given in Table A.3. The intermediate values are calculated by computing a linearly spaced vector of length 8 between  $\sqrt{D_{\min}}$  and  $\sqrt{D_{\max}}$  and then squaring all the terms, which ensures that the resulting expected shapes evenly cover the area between  $D_{\min}$  and  $D_{\max}$  when viewed in a spectrogram. Note that different coefficients are computed on the dayside than at night as set by the most significant bit of byte 2.

### A.2.2 Output Data Format

Each instrument on board the TARANIS satellite must output data in packets of 2088 bytes consisting of 40 header bytes and 2048 data bytes. The first two bytes in the header are known as the APID and denote the format of the data in the packet. There are four APIDs allotted to the ZPD: 1244, 1245, 1246, and 1247. As long as the spacecraft is not operating in burst mode, the satellite will extract one ZPD

**Table A.3:** Dispersion Constants according to LSBs of Input Byte 3

Byte 3 LSBs		Daytime		Nighttime	
(Binary)	(Hexadecimal)	$D_{\min}$	$D_{\max}$	$D_{\min}$	$D_{\max}$
0000	0x0	1	8	1	5
0001	0x1	0.5	7.5	0.5	4.5
0010	0x2	1.5	8.5	1.5	5.5
0011	0x3	2	9	2	6
0100	0x4	0.5	9	2.5	6.5
0101	0x5	0.5	10	0.5	6
0110	0x6	0.5	5.5	1	6.5
0111	0x7	1	6	0.4	7
1000	0x8	1.5	6.5	0.3	9
1001	0x9	2	7	0.25	3.25
1010	0xA	3	8	0.5	3.5
1011	0xB	4	9	1	4
1100	0xC	5	10	1.5	4.5
1101	0xD	2	5.5	2	5
1110	0xE	3	6.5	2.5	5.5
1111	0xF	4	7.5	3	6

TARANIS packet from the SN74V623 external FIFO every three seconds. Therefore, in order to not overflow the external FIFO and lose data due to lack of storage space, the ZPD attempts to write TARANIS packets at the same rate as they are extracted. As the  $0^+$  whistler rate increases, the ZPD switches to an output format that allots fewer bytes per whistler so that the overall output bit rate remains about the same. A brief summary of the data format for each APID is given below:

- APID 1244: A 64x30 spectrogram is written in one packet.
- APID 1245: For 30 whistlers, the time, algorithm output (i.e., the result of (2.12)), and amplitude of the  $0^+$  whistler's spectrogram at 60 frequencies is written over the available bytes in one packet.
- APID 1246: For 120 whistlers, the same information is written in one packet as in APID 1245 but with fewer frequencies (only 12 this time).
- APID 1247: For 480 whistlers, only the time, algorithm output, and the  $0^+$

whistler's normalized spectrogram (i.e., the result of (2.6)) at four frequencies is written in one packet.

We have supplied to the contractor in charge of processing data from TARANIS software that converts raw binary TARANIS packets from the ZPD to Common Data Format (CDF) files. Those data files will be available on the data server with data from the other instruments on the satellite.

# Bibliography

- Abel, B., and R. M. Thorne (1998a), Electron scattering loss in Earth's inner magnetosphere 1. Dominant physical processes, *J. Geophys. Res.*, *103*(A2), 2385–2396, doi:10.1029/97JA02919.
- Abel, B., and R. M. Thorne (1998b), Electron scattering loss in Earth's inner magnetosphere: 2. Sensitivity to model parameters, *J. Geophys. Res.*, *103*(A2), 2397–2407, doi:10.1029/97JA02920.
- Appleton, E. V., and M. A. F. Barnett (1925), Local Reflection of Wireless Waves from the Upper Atmosphere, *Nature*, *115*, 333–334, doi:10.1038/115333a0.
- Armstrong, W. C. (1983), Recent advances from studies of the Trimpf effect, *Antarct. J.*, *18*, 281–283.
- Baker, D. N. (2002), How to Cope with Space Weather, *Science*, *297*(5586), 1486–1487, doi:10.1126/science.1074956.
- Barkhausen, H. (1919), Zwei mit Hilfe der neuen Verstärker entdeckte Erscheinungen, *Phys. Z.*, *20*, 401–403.
- Barkhausen, H. (1930), Whistling Tones from the Earth, *Proc. IRE*, *18*(7), 1155 – 1159, doi:10.1109/JRPROC.1930.222122.
- Bell, T. F., U. S. Inan, D. Piddychiy, P. Kulkarni, and M. Parrot (2008), Effects of plasma density irregularities on the pitch angle scattering of radiation belt electrons by signals from ground based VLF transmitters, *Geophys. Res. Lett.*, *35*(19), L19,103, doi:10.1029/2008GL034834.



- Berthelier, J. J., M. Godefroy, F. Leblanc, M. Malingre, M. Menvielle, D. Lagoutte, J. Y. Brochot, F. Colin, F. Elie, C. Legendre, P. Zamora, D. Benoist, Y. Chapuis, J. Artru, and R. Pfaff (2006), ICE, the electric field experiment on DEMETER, *Planet. Space Sci.*, *54*(5), 456–471, doi:10.1016/j.pss.2005.10.016.
- Bilitza, D., D. Altadill, Y. Zhang, C. Mertens, V. Truhlik, P. Richards, L.-A. McKinnell, and B. Reinisch (2014), The International Reference Ionosphere 2012 - a model of international collaboration, *J. Space Weather Space Clim.*, *4*, A07, doi:10.1051/swsc/2014004.
- Bortnik, J., U. S. Inan, and T. F. Bell (2003), Energy distribution and lifetime of magnetospherically reflecting whistlers in the plasmasphere, *J. Geophys. Res.*, *108*(A5), 1199, doi:10.1029/2002JA009316.
- Breit, G., and M. A. Tuve (1925), A Radio Method of Estimating the Height of the Conducting Layer, *Nature*, *116*, 357, doi:10.1038/116357a0.
- Bruce, C. E. R., and R. H. Golde (1941), The lightning discharge, *J. Inst. Elec. Eng. - Part II: Power Eng.*, *88*(6), 487–505, doi:10.1049/ji-2.1941.0065.
- Burgess, W. C., and U. S. Inan (1993), The role of ducted whistlers in the precipitation loss and equilibrium flux of radiation belt electrons, *J. Geophys. Res.*, *98*(A9), 15,643–15,665, doi:10.1029/93JA01202.
- Carpenter, D. L. (1963), Whistler evidence of a 'knee' in the magnetospheric ionization density profile, *J. Geophys. Res.*, *68*(6), 1675–1682, doi:10.1029/JZ068i006p01675.
- Christian, H. J., R. J. Blakeslee, D. J. Boccippio, W. L. Boeck, D. E. Buechler, K. T. Driscoll, S. J. Goodman, J. M. Hall, W. J. Koshak, D. M. Mach, and M. F. Stewart (2003), Global frequency and distribution of lightning as observed from space by the Optical Transient Detector, *J. Geophys. Res.*, *108*(D1), 4005, doi:10.1029/2002JD002347.

- Chum, J., F. Jiricek, O. Santolik, M. Parrot, G. Diendorfer, and J. Fiser (2006), Assigning the causative lightning to the whistlers observed on satellites, *Ann. Geophys.*, *24*(11), 2921–2929, doi:10.5194/angeo-24-2921-2006.
- Cohen, M. B., and U. S. Inan (2012), Terrestrial VLF transmitter injection into the magnetosphere, *J. Geophys. Res.*, *117*(A8), A08,310, doi:10.1029/2012JA017992.
- Cohen, M. B., N. G. Lehtinen, and U. S. Inan (2012), Models of Ionospheric VLF Absorption of Powerful Ground Based Transmitters, *Geophys. Res. Lett.*, doi:10.1029/2012GL054437.
- Colman, J. J., and M. J. Starks (2013), VLF wave intensity in the plasmasphere due to tropospheric lightning, *J. Geophys. Res. Space Physics*, *118*(7), 4471–4482, doi:10.1002/jgra.50217.
- Cooley, J. W., and J. W. Tukey (1965), An Algorithm for the Machine Calculation of Complex Fourier Series, *Mathematics of Computation*, *19*(90), 297–301, doi:10.2307/2003354.
- Cornwall, J. M. (1964), Scattering of Energetic Trapped Electrons by Very-Low-Frequency Waves, *J. Geophys. Res.*, *69*(7), 1251–1258, doi:10.1029/JZ069i007p01251.
- Cummins, K. L., and M. J. Murphy (2009), An Overview of Lightning Locating Systems: History, Techniques, and Data Uses, With an In-Depth Look at the U.S. NLDN, *IEEE Trans. Electromagn. Compat.*, *51*(3), 499–518, doi:10.1109/TEM.2009.2023450.
- Davies, K. (1990), *Ionospheric Radio*, *IEE Electromagnetic Waves Series*, vol. 31, Peter Peregrinus Ltd., London.
- Dolph, C. L. (1946), A Current Distribution for Broadside Arrays Which Optimizes the Relationship between Beam Width and Side-Lobe Level, *Proc. IRE*, *34*(6), 335–348, doi:10.1109/JRPROC.1946.225956.

- Dungey, J. W. (1963), Loss of Van Allen electrons due to whistlers, *Planet. Space Sci.*, *11*(6), 591–595, doi:10.1016/0032-0633(63)90166-1.
- Eckersley, T. L. (1935), Musical Atmospherics, *Nature*, *135*(3403), 104–105, doi:10.1038/135104a0.
- Elie, F., M. Hayakawa, M. Parrot, J.-L. Pinçon, and F. Lefeuvre (1999), Neural Network System for the Analysis of Transient Phenomena on Board the DEMETER MicroSatellite, *IEICE Trans. Fundamentals*, (8).
- Finlay, C. C., S. Maus, C. D. Beggan, T. N. Bondar, A. Chambodut, T. A. Chernova, A. Chulliat, V. P. Golovkov, B. Hamilton, M. Hamoudi, R. Holme, G. Hulot, W. Kuang, B. Langlais, V. Lesur, F. J. Lowes, H. Lühr, S. Macmillan, M. Manda, S. McLean, C. Manoj, M. Menvielle, I. Michaelis, N. Olsen, J. Rauberg, M. Rother, T. J. Sabaka, A. Tangborn, L. Tøffner-Clausen, E. Thébaud, A. W. P. Thomson, I. Wardinski, Z. Wei, T. I. Zvereva, and W. G. V.-M. Participating members of the International Association of Geomagnetism and Aeronomy (2010), International Geomagnetic Reference Field: the eleventh generation, *Geophys. J. Int.*, *183*(3), 1216–1230, doi:10.1111/j.1365-246X.2010.04804.x.
- Fiser, J., J. Chum, G. Diendorfer, M. Parrot, and O. Santolik (2010), Whistler intensities above thunderstorms, *Ann. Geophys.*, *28*(1), 37–46, doi:10.5194/angeo-28-37-2010.
- Foust, F. R., U. S. Inan, T. Bell, and N. G. Lehtinen (2010), Quasi-electrostatic whistler mode wave excitation by linear scattering of EM whistler mode waves from magnetic field-aligned density irregularities, *J. Geophys. Res.*, *115*(A11), A11,310, doi:10.1029/2010JA015850.
- Fukunishi, H., Y. Takahashi, M. Kubota, K. Sakanoi, U. S. Inan, and W. A. Lyons (1996), Elves: Lightning-induced transient luminous events in the lower ionosphere, *Geophys. Res. Lett.*, *23*(16), 2157–2160, doi:10.1029/96GL01979.
- Galinsky, V. L., V. I. Shevchenko, E. V. Mishin, and M. J. Starks (2011), Numerical

- modeling of 3d weak turbulence driven by high-power VLF pump waves in the topside ionosphere, *Geophys. Res. Lett.*, *38*(16), L16,105, doi:10.1029/2011GL048441.
- Gemelos, E. S., U. S. Inan, M. Walt, M. Parrot, and J. A. Sauvaud (2009), Seasonal dependence of energetic electron precipitation: Evidence for a global role of lightning, *Geophys. Res. Lett.*, *36*(21), L21,107, doi:10.1029/2009GL040396.
- Graf, K. L., N. G. Lehtinen, M. Spasojevic, M. B. Cohen, R. A. Marshall, and U. S. Inan (2013), Analysis of experimentally validated trans-ionospheric attenuation estimates of VLF signals, *Journal of Geophysical Research: Space Physics*, *118*(5), 2708–2720, doi:10.1002/jgra.50228.
- Harris, F. J. (1978), On the use of windows for harmonic analysis with the discrete Fourier transform, *Proc. IEEE*, *66*(1), 51 – 83, doi:10.1109/PROC.1978.10837.
- Heaviside, O. (1902), *Theory of Electric Telegraphy*.
- Helliwell, R. A. (1965), *Whistlers and related ionospheric phenomena*, Stanford University Press, Stanford, California.
- Hogenauer, E. (1981), An economical class of digital filters for decimation and interpolation, *IEEE Trans. Acoust., Speech, Signal Process.*, *29*(2), 155–162, doi:10.1109/TASSP.1981.1163535.
- Inan, U. S., and M. Golkowski (2010), *Principles of Plasma Physics for Engineers and Scientists*, Cambridge University Press, Cambridge.
- Inan, U. S., H. C. Chang, and R. A. Helliwell (1984), Electron precipitation zones around major ground-based VLF signal sources, *J. Geophys. Res.*, *89*(A5), 2891–2906, doi:10.1029/JA089iA05p02891.
- Inan, U. S., D. C. Shafer, W. Y. Yip, and R. E. Orville (1988), Subionospheric VLF signatures of nighttime D region perturbations in the vicinity of lightning discharges, *J. Geophys. Res.*, *93*(A10), 11,455–11,472, doi:10.1029/JA093iA10p11455.

- Inan, U. S., T. F. Bell, and J. V. Rodriguez (1991), Heating and ionization of the lower ionosphere by lightning, *Geophys. Res. Lett.*, *18*(4), 705–708, doi:10.1029/91GL00364.
- Jacobson, A. R., R. H. Holzworth, R. F. Pfaff, and M. P. McCarthy (2011), Study of oblique whistlers in the low-latitude ionosphere, jointly with the C/NOFS satellite and the World-Wide Lightning Location Network, *Ann. Geophys.*, *29*(5), 851–863, doi:10.5194/angeo-29-851-2011.
- Kennelly, A. E. (1902), On the Elevation of the Electrically Conducting Strata of the Earth's Atmosphere, *Electrical World and Engineer*, *39*, 473.
- Lehtinen, N. G., and U. S. Inan (2008), Radiation of ELF/VLF waves by harmonically varying currents into a stratified ionosphere with application to radiation by a modulated electrojet, *J. Geophys. Res.*, *113*, 7, doi:200810.1029/2007JA012911.
- Lehtinen, N. G., and U. S. Inan (2009), Full-wave modeling of transionospheric propagation of VLF waves, *Geophys. Res. Lett.*, *36*, 5, doi:200910.1029/2008GL036535.
- Lodge, O. (1902), Mr. Marconi's Results in Day and Night Wireless Telegraphy, *Nature*, *66*(1705), 222, doi:10.1038/066222c0.
- Lyons, W. A. (1994), Characteristics of luminous structures in the stratosphere above thunderstorms as imaged by low-light video, *Geophys. Res. Lett.*, *21*(10), 875–878, doi:10.1029/94GL00560.
- Matteo, N. A., and Y. T. Morton (2011), Ionosphere geomagnetic field: Comparison of IGRF model prediction and satellite measurements 1991-2010, *Radio Sci.*, *46*, 10, doi:201110.1029/2010RS004529.
- McIlwain, C. E. (1961), Coordinates for mapping the distribution of magnetically trapped particles, *J. Geophys. Res.*, *66*(11), 3681–3691, doi:10.1029/JZ066i011p03681.

- Meredith, N. P., R. B. Horne, S. A. Glauert, and R. R. Anderson (2007), Slot region electron loss timescales due to plasmaspheric hiss and lightning-generated whistlers, *J. Geophys. Res.*, *112*(A8), A08,214, doi:10.1029/2007JA012413.
- Mishin, E. V., M. J. Starks, G. P. Ginet, and R. A. Quinn (2010), Nonlinear VLF effects in the topside ionosphere, *Geophys. Res. Lett.*, *37*(4), L04,101, doi:10.1029/2009GL042010.
- Parrot, M., D. Benoist, J. Berthelier, J. Błęcki, Y. Chapuis, F. Colin, F. Elie, P. Fergau, D. Lagoutte, F. Lefeuvre, C. Legendre, M. Lévêque, J. Pinçon, B. Poirier, H.-C. Seran, and P. Zamora (2006), The magnetic field experiment IMSC and its data processing onboard DEMETER: Scientific objectives, description and first results, *Planet. Space Sci.*, *54*(5), 441–455, doi:10.1016/j.pss.2005.10.015.
- Parrot, M., U. S. Inan, and N. G. Lehtinen (2008), V-shaped VLF streaks recorded on DEMETER above powerful thunderstorms, *J. Geophys. Res.*, *113*, 6, doi:200810.1029/2008JA013336.
- Said, R. K., U. S. Inan, and K. L. Cummins (2010), Long-range lightning geolocation using a VLF radio atmospheric waveform bank, *J. Geophys. Res.*, *115*(D23), D23,108, doi:10.1029/2010JD013863.
- Said, R. K., M. B. Cohen, and U. S. Inan (2013), Highly intense lightning over the oceans: Estimated peak currents from global GLD360 observations, *J. Geophys. Res. Atmos.*, *118*(13), 6905–6915, doi:10.1002/jgrd.50508.
- Sentman, D. D., E. M. Wescott, D. L. Osborne, D. L. Hampton, and M. J. Heavner (1995), Preliminary results from the Sprites94 Aircraft Campaign: 1. Red sprites, *Geophys. Res. Lett.*, *22*(10), 1205–1208, doi:10.1029/95GL00583.
- Smith, R. L., and J. J. Angerami (1968), Magnetospheric Properties Deduced from OGO 1 Observations of Ducted and Nonducted Whistlers, *J. Geophys. Res.*, *73*(1), 1–20, doi:10.1029/JA073i001p00001.

- Starks, M. J., R. A. Quinn, G. P. Ginet, J. M. Albert, G. S. Sales, B. W. Reinisch, and P. Song (2008), Illumination of the plasmasphere by terrestrial very low frequency transmitters: Model validation, *J. Geophys. Res.*, *113*, 16, doi: 200810.1029/2008JA013112.
- Storey, L. R. O. (1953), An Investigation of Whistling Atmospherics, *Phil. Trans. R. Soc. Lond. A*, *246*(908), 113–141, doi:10.1098/rsta.1953.0011.
- Swamy, A. C. B. (1992), Equatorial electrojet parameters and the relevance of Electromagnetic Drifts (EMD) over Thumba, *Astrophys Space Sci*, *191*(2), 203–211, doi:10.1007/BF00644769.
- Taylor, J. E. (1903), Characteristics of Electric Earth-Current Disturbances, and Their Origin, *Proc. Phys. Soc. (London)*, *71*, 225–227.
- Uman, M. A. (1987), *The Lightning Discharge, International Geophysics*, vol. 39, 1 ed., Academic Press, Orlando, Florida.
- Van Allen, J. A., and L. A. Frank (1959), Radiation Around the Earth to a Radial Distance of 107,400 km, *Nature*, *183*(4659), 430–434, doi:10.1038/183430a0.
- Walt, M. (1994), *Introduction to Geomagnetically Trapped Radiation*, Cambridge University Press, Cambridge.
- Zoghzoghy, F. G., M. B. Cohen, R. K. Said, N. G. Lehtinen, and U. S. Inan (2015), Shipborne LF-VLF oceanic lightning observations and modeling, *J. Geophys. Res. Atmos.*, p. 2015JD023226, doi:10.1002/2015JD023226.